Spectroscopic Study on Metalorganic Chemical Vapor Deposition Mechanisms of Barium Strontium Titanate Films(Dissertation_全文)

AUTHOR(S):

Momose, Shun

Spectroscopic Study on Metalorganic Chemical Vapor Deposition Mechanisms of Barium Strontium Titanate Films

Shun Momose

2002

Spectroscopic Study on Metalorganic Chemical Vapor Deposition Mechanisms of Barium Strontium Titanate Films

Shun Momose

2002

Abstract

In this thesis, the chemical reactions during the deposition of barium strontium titanate (Ba,Sr)TiO_3 [BST] films were investigated. BST is a high dielectric substance which has been attracting a great deal of attention as the most promising capacitor dielectrics of dynamic random access memories (DRAMs), because it has high dielectric constant and paraelectric properties around room temperature. As a method to prepare BST films, metalorganic chemical vapor deposition (MOCVD) technique was adopted because this technique has especially excellent step coverage. As CVD source materials, dipivaloymethanato (DPM) chelate compounds such as $Ba(DPM)_2$, $Sr(DPM)_2$ and $Ti(t\text{-}BuO)_2(DPM)_2$ were used. Although many groups around the world were intensively employed in the research of BST films, BST-DRAM has not been manufactured for practical use yet because the reproducibility and improvement of electrical properties required for actual memory devices remain to be solved. In order to solve these problems, it is absolutely necessary to understand the deposition mechanism of BST films. Therefore, we elucidated the chemistries in MOCVD of BST films by using spectroscopic techniques such as Fourier transform infrared (FT-IR) spectroscopy and optical emission spectroscopy (OES).

We studied the thermal decompositions of $Ba(DPM)_2$, $Sr(DPM)_2$ and $Ti(t\text{-}BuO)_2(DPM)_2$ under actual CVD conditions by *in situ* FT-IR spectroscopy. From the temperature dependence of the IR absorbance, the thermal stability of the chemical bonds in the source molecules was investigated. We discussed the effects of these thermal decompositions on the deposition mechanism of BST films. Although $Sr(DPM)_2$ and $Ba(DPM)_2$ molecules decompose completely in the gas phase before Sr and Ba atoms are incorporated in the film, the deposition of Ti atoms does not require the complete

decomposition of Ti(t-BuO)$_2$(DPM)$_2$ molecules in the gas phase. In order to understand the gas-phase reactions in more detail, we developed a novel diagnostic tool for MOCVD processings, which was named microdischarge optical emission spectroscopy (μD-OES), and applied it to the diagnosis in MOCVD of BST films. From the emission spectra of the small plasma excited at the μD-OES sensor head, it is possible to estimate the degree of thermal decomposition of the CVD source molecules. The experimental findings obtained by μD-OES measurements were discussed with referring to *in situ* FT-IR measurements. In order to study the contribution of gas-phase reactions to the film deposition, the temperature dependence of the observed emission intensity was investigated in connection with the film deposition rate and quality. For this procedure, it is important to know the correlation between the gas temperature and the substrate temperature. The gas temperature can be estimated from the rotational temperature of molecular nitrogen, the carrier gas of the CVD sources. By using μD-OES, the interaction between other source molecules was also studied.

The addition of an oxidation gas such as O_2 or N_2O is empirically known to improve the crystallinity of the BST films. Thus, we also conducted the spectroscopic measurements to investigate the oxidation reactions of the source molecules. We compared oxidation mechanisms between O_2 and N_2O. IR absorption spectroscopy showed that O_2 is more reactive than N_2O in the gas phase, and selectively attacks low-electron-density sites in the source molecules. We deposited strontium oxide and BST films in O_2 and N_2O ambients, and investigated the relationship between the qualities of deposited films and the gas-phase reaction mechanism. From the viewpoint of the suppression of carbon contamination and the controllability of the atomic composition ratio of deposited films, it was concluded that O_2 is more suitable than N_2O for the deposition of BST films.

These spectroscopic studies clarified the formation mechanism of film precursors in the gas phase. In addition to the spectroscopic studies, a series of deposition experiments, which includes isotopic labeling study using $^{18}O_2$, was conducted in order to investigate the surface reactions during the BST film growth. The findings on the surface reactions were in good accordance with the precursor formation mechanism suggested from the spectroscopic

diagnoses of the gas-phase reactions. In conclusion, a deep understanding of the deposition chemistry is a key step for the development of electronic devices manufactured by CVD method. In this work, we developed a set of *in situ* spectroscopic diagnostics applicable to the reaction analysis of the MOCVD process of various films.

Acknowledgments

I would like to express my deep gratitude to Prof. Kunihide Tachibana for continuous guidance, encouragement, and critical supervision throughout this work. I am grateful to Prof. Minoru Suzuki and Prof. Masahiro Kawasaki for critical reading of the manuscript and valuable comments. I must express sincerely my gratitude to Dr. Toshihiro Nakamura from my heart. He gave me many elementary lessons for research activities, very valuable advice and encouragement at any time. I thank Associate Prof. Yasuyoshi Yasaka, Associate Prof. Tatsuru Shirafuji and Mr. Makoto Kubo for their support on this study. I am grateful to Dr. Kouichi Ono (Presently at Kyoto University), Mr. Tatsuo Oomori, Mr. Hiroshi Takada, Mr. Tsuyoshi Horikawa, Dr. Takaaki Kawahara, Dr. Masayoshi Tarutani and Mr. Mikio Yamamuka of Mitsubishi Electric Corporation for their kind advice on the CVD experiments. I could use experimental facilities in Kyoto University Venture Business Laboratory (KU-VBL). I thank Mr. Toshihisa Horiuchi, Mr. Hiroshi Tsuji and Dr. Jun Suda for their assistance in the use of the XRD, XPS and SEM apparatus in the KU-VBL. At conferences, I could get advice from many researchers. Especially, I thank Associate Prof. Masaru Shimizu of Himeji Institute of Technology and Associate Prof. Hiroshi Funakubo of Tokyo Institute of Technology for valuable comments on the diagnosis of MOCVD processing.

I had a very nice time in Tachibana Laboratory of Kyoto University, where I have met a lot of nice people. This study is owed to them very much. I would like to thank Dr. Kazuo Takahashi, Mr. Hideki Motomura, Mr. Tetsuo Kikuchi, Mr. Ryusuke Sahara and other members of Tachibana Lab. for experimental supports, helpful discussions and spending a precious time together. At last, I would like to express my gratitude to my family,

who have encouraged me to continue this study.

Contents

Chapter 1

Introduction

Metalorganic chemical vapor deposition (MOCVD) is a very important method to prepare various films of valuable industrial use. In this work, we establish diagnostic techniques for the MOCVD process, and apply them to the diagnosis in MOCVD of barium strontium titanate (Ba,Sr)TiO_3 [BST] films, which have attracted increasing interest as the most promising capacitor dielectrics for Gbit-scale dynamic random access memory (DRAM) because of their high dielectric constant. In order to investigate the deposition mechanism of BST films, we apply spectroscopic techniques, since those are non-destructive and can be carried out under actual CVD conditions. In this chapter, I will present briefly the overview of the structure and operation scheme of a DRAM cell, high-k materials for a capacitor of the memory cell, preparation methods of thin films and diagnostic techniques for MOCVD of BST films. Finally I will describe the constitution of this thesis.

1.1 Background

At the present time, electronic appliances such as personal computer, mobile phone and personal digital assistance (PDA) are coming into wide use. The

downsizing and high performance of these electronic products are achieved by the progress of integration of embedded large-scale integrated (LSI) circuits. Since the invention of integrated circuits about forty years ago, design rules of micro-electronic circuits and manufacturing technologies have evolved toward higher integration [1, 2]. Especially, dynamic random access memory (DRAM) occupies a large amount in the market of semiconductor products, and has been a good tractive force for the development of the art of silicon device technology up to the present day. The integration of DRAM has progressed by a factor of 4 every three years during the past 25 years, and this trend may continue in future. This remarkable increase in the memory density has been brought about by advances in various technology areas, including lithography, dry etching and thin-film deposition.

1.1.1 Dynamic random access memory

Figure 1.1 shows a schematic diagram of the electric circuit of a DRAM memory cell. One memory cell consists of a storage capacitor and a transistor with the drain connected to one node of the capacitor, the source connected to a bit line and the gate connected to a word line, which runs orthogonal by the bit line. The requirement to have a large capacitor in a small space with low leakage is the main issue of DRAM technology. A memory cell operates as follows. To write, the bit line is driven to a high or low logic level with the cell transistor turned on, and then the cell transistor is shut off, leaving the capacitor charged high or low. Since capacitor charge leaks off gradually, its refresh is needed. To read, or refresh the data in the cell, the bit line is left floating when the cell transistor is turned on, and the small change in bit-line potential is sensed and amplified to a full logic level. The ratio of cell capacitance to bit-line capacitance determines the magnitude of the change in bit-line potential. So, the former should be larger than the latter to deliver an adequate signal to the sense amplifier.

The DRAM cell structure has been developed over the years from the simple planar-capacitor type to the trench-capacitor or stacked-capacitor type, which is most commonly used at present. Figure 1.2 shows schematic diagrams of the stacked and trench cell structures. In the stacked cell, the

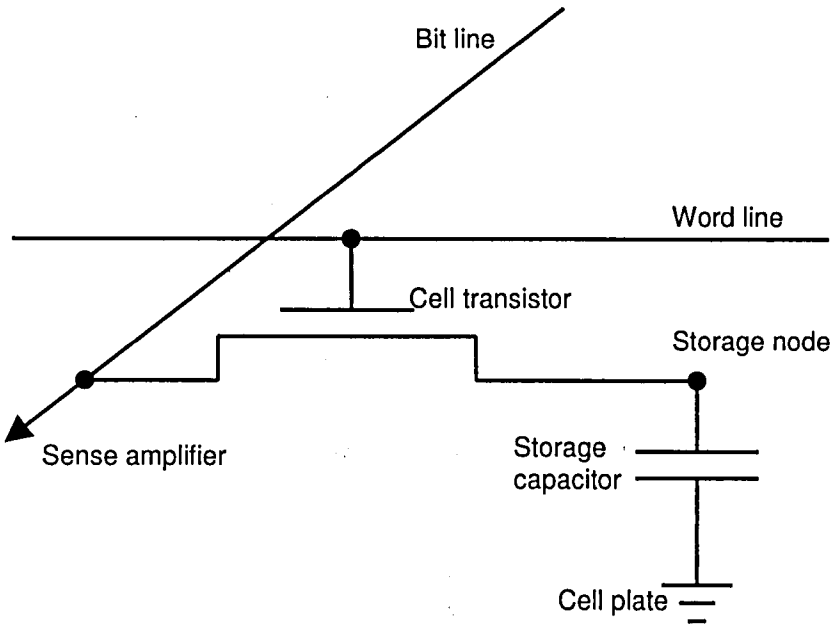

Figure 1.1: Schematic diagram of one-transistor memory cell of DRAMs.

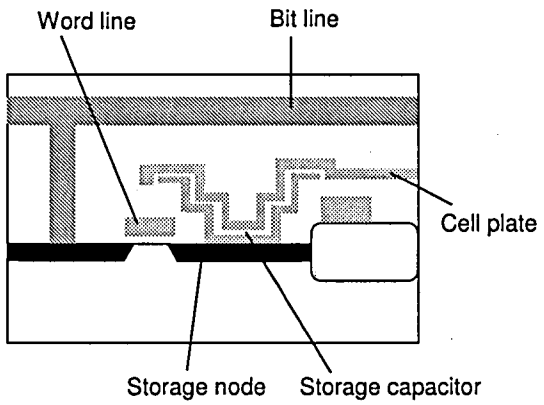

Stacked cell

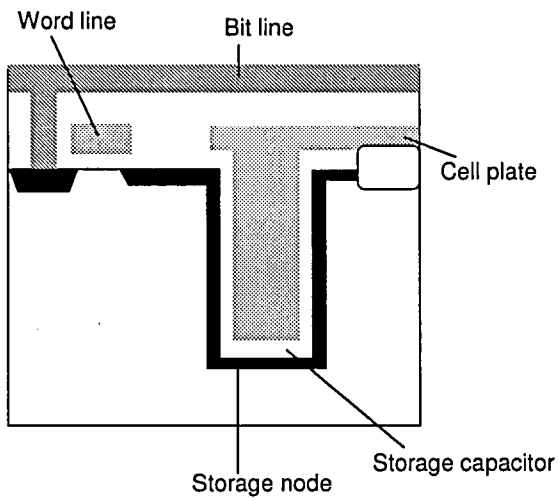

Trench cell

Figure 1.2: Schematic diagrams of DRAM cell structure: stacked cell and trench cell.

storage node lies above the horizontal plane of the DRAM cell access transistor. In the other trench cell, the storage node is in a trench etched in the substrate. Its most important advantage comes from the possibility to use conventional contacts, interconnections and active device processing, because the storage capacitor is formed prior to these elements. But, it has drawbacks, as well: difficulties in the etching of deep trenches into Si with high aspect ratio and the formation of an uniform and reliable dielectric film inside of the trench.

1.1.2 High-k dielectrics for memory devices

As the integration of memory cell advances greater, the cell size is becoming smaller and the capacitance of the cell is decreasing. In order to obtain reliable operation of a DRAM, a certain amount of charge must be stored in the capacitor of a memory cell. This minimum charge has been decreased by a factor of 3 per generation up to now. Similar decreases in operating voltage are expected for future DRAM generations, so that the required DRAM capacitance will remain nearly constant at 25~30 fF/cell. Relationship of these physical values is expressed by the following equation;

$$Q = C \times V, \tag{1.1}$$

where:

Q: charge stored on a capacitor,
C: electrostatic capacitance,
V: operating voltage.

Electrostatic capacitance of one memory cell is given by;

$$C[\mathrm{F/cell}] = \epsilon_0[\mathrm{F/m}] \times \epsilon_r \frac{A[\mathrm{m^2}]}{t[\mathrm{m}]}, \tag{1.2}$$

where:

ϵ_0: dielectric constant of free space(=8.855 $\times 10^{-14}$ [F/cm]),
ϵ_r: relative dielectric constant,
A: area of the electrodes,
t: film thickness.

So, it is inevitable to increase the electrostatic capacitance when the memory

cell is shrinking. Higher capacitance density can be achieved by the use of 1) complex electrode structures providing a large surface area within a small lateral area, 2) thinner capacitor dielectrics and 3) higher-permittivity dielectric materials. In early days when kbit-scale DRAMs were prevalent, the decrease in the thickness of capacitor dielectrics was kept pursued. But the leakage current increases if the thickness becomes too small, so the decrease of dielectric film thickness has reached its limit. In the Mbit generations, the effective capacitor area was increased by employing three-dimensionally shaped storage node electrodes. But complex electrode structure needs additional manufacture processes, and increases the cost of manufacturing of DRAMs. Thus, as the last parameter, the dielectric constant should be improved inevitably for the development of Gbit-scale memories and beyond.

Today, SiO_2, Si_3N_4 and Ta_2O_5 films are used as capacitor dielectrics for DRAMs, and a lot of researchers have been interested in materials with higher dielectric constant in order to substitute for these conventional capacitor dielectrics. As high dielectric materials, strontium titanate $SrTiO_3$ [STO], barium strontium titanate $(Ba,Sr)TiO_3$ [BST] and lead zirconate titanate $Pb(Zr,Ti)O_3$ [PZT] are nominated. Dielectric constant of each material becomes greater in the above order; i.e. STO < BST < PZT. Although the dielectric constant of PZT is higher than that of BST, PZT is ferroelectric substance at room temperature and the electrical fatigue induced by the repetition of the reverse of electronic polarization is a very serious problem. Moreover, PZT has a severe problem of Pb diffusion in semiconductor process. On the other hand, BST has paraelectric property around room temperature. From above reasons, BST thin film attracts increasing attention as the most promising capacitor dielectrics for Gbit-scale DRAMs. Figure 1.3 shows the crystal structure of BST, which has a perovskite structure.

1.2 Film preparation

Although the use of high dielectric constant materials allows simple storage node geometries, even those high-k materials such as BST do not have adequate capacitance per unit area to allow planar storage capacitors for 1 Gbit densities. Since three-dimensional geometries will be required, a conformal

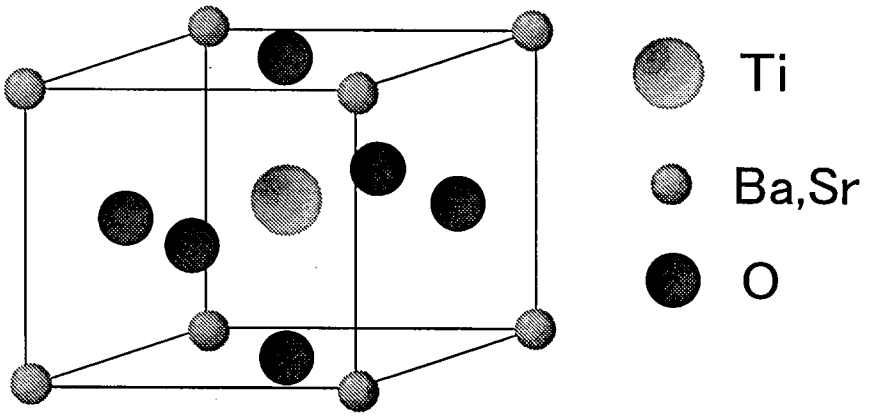

Figure 1.3: Perovskite crystal structure of (Ba,Sr)TiO_3.

deposition process is desired. Among the various techniques used to prepare BST thin films, the metalorganic chemical vapor deposition (MOCVD) technique is recognized as the leading candidate for practical manufacturing because of its good step coverage performance.

1.2.1 Metalorganic chemical vapor deposition

As the method of film preparation, various techniques such as sputtering, laser ablation, sol-gel, metalorganic decomposition (MOD) and chemical vapor deposition (CVD) are given. Conditions required for the preparation of dielectric thin films are:

1. Controllability of atomic composition.
2. Good electrical properties such as large dielectric constant and small leakage current.
3. High deposition rate.
4. Low deposition temperature.

5. Conformal step coverage.

6. Excellent conformity with the LSI process of Si/SiO_2.

7. Uniformity in the large area deposition.

When these conditions are taken into consideration, laser ablation is insufficient in regard to the points of 5, 6 and 7. Although sol-gel and MOD are comparatively handy methods with good controllability, there is a problem as regards the fatal step coverage. Sputtering is a high potential method for preparation of BST films, and it is reported that BST films fabricated by sputtering have very good electrical properties [3, 4, 5]. But poor step coverage of films deposited by sputtering is a large obstacle for the development of Gbit-generation DRAMs. Since the CVD technique satisfies most of these requirements among all methods listed above, it is considered as the most promising technique for preparation of high dielectric films. In the preparation of BST films, organometallic compounds are used as source materials for the CVD, so this technique is especially called as metalorganic chemical vapor deposition (MOCVD). In recent years, many research groups are very eager to develop BST-DRAMs prepared by MOCVD. Studies of BST films prepared by MOCVD are carried out actively in Japanese and Korean electronic companies such as *Mitsubishi Electric Corporation* [6, 7, 8, 9, 10, 11, 12, 13, 14, 15, 16], *Toshiba Corporation* [17], *Murata Manufacturing Corporation* [18, 19] and *SAMSUNG Electronics Corporation* [20], and other groups are also studying about MOCVD of BST films [21, 22, 23, 24, 25, 26].

As MOCVD techniques, conventional thermal MOCVD and plasma MOCVD are given. As an example of plasma MOCVD, BST film is reported to be deposited by using ECR (Electron Cyclotron Resonance) plasma [27, 28, 29]. This plasma MOCVD technique is expected to deposit excellent crystalline BST films at comparatively low substrate temperature by promoting the decomposition of source molecules with oxygen plasma. Furthermore, as compared with thermal MOCVD, it was found that in plasma MOCVD there is less carbon contamination which causes the deterioration of electrical properties of deposited films. But, plasma MOCVD

has several crucial problems. At first, its deposition rate is smaller than that of thermal MOCVD by an order of magnitude. Moreover, it has problems such as poor step coverage and small deposition area. For above reasons, we employ the thermal MOCVD technique as a method for preparation of BST films in this work.

1.2.2 CVD source materials

Desirable conditions for MOCVD precursors are listed up as follows:

1. High volatility.
2. Source materials are in a liquid form at room temperature.
3. Large gap between evaporation temperature and thermal decomposition temperature.
4. Thermal stability until they are supplied into a reactor.
5. Safety toward the environment and the human body.
6. All source materials have evaporation temperatures similar to one another.

The condition 1 is very important to achieve a large deposition rate. The condition 2 is necessary to keep evaporation speed constant, because evaporation speed of solid source materials changes due to the change of surface area of powders when sublimation of solid materials is proceeding. In this study, we dissolve solid source materials into liquid solvent, and used them in a liquid form. The condition 3 is inevitably necessary for practical manufacturing. If the temperature gap between evaporation and thermal decomposition is small, CVD source molecules tend to decompose on the way of transport to a CVD reactor. As a result, the utilization efficiency of source materials gets deteriorated. Moreover, when the thermal decomposition of source molecules occurs on the way to a reactor, there is the possibility that decomposition products may be incorporated into deposited films, which deteriorates electrical properties of deposited films. The condition 4 is very important for the preservation of source materials and the reproducibility

of film deposition. The condition 5 is necessary from the viewpoint of practical industrial use. The condition 6 is required for manufacturing compound materials. In the case of oxide compound films such as BST, film properties are likely to change by the variation of atomic composition ratio of the deposited films. If those sources' evaporation temperatures differ largely from one another, it is difficult to control an atomic composition ratio of the deposited films precisely. Therefore, it is necessary to use source materials which have similar evaporation characteristics. Moreover, since these source materials are used for semiconductor process, they must be highly purified. After taking account of these requirements, we use metal β-diketonate complexes such as bis(dipivaloylmethanato)barium [$Ba(DPM)_2$], bis(dipivaloylmethanato)strontium [$Sr(DPM)_2$], and bis(tertiarybutoxy)bis(dipivaloylmethanato)titanium [$Ti(t\text{-}BuO)_2(DPM)_2$] as the source materials, whose molecular structures are shown in Fig. 1.4. Each metal complex has coordinate bonds with a metal atom. The coordinate bond is a special case of covalent bonds. Electrons contributing to this bond are supplied from an incovalent electron pair on one side of the atom. To form the coordinate bond, an atom having the incovalent electron pair (electron donor) and an atom having an empty orbital (electron acceptor) are necessary. The former is a DPM ligand and the latter is a metal ion in metal complexes.

1.2.3 Liquid-source technique

One of the most challenging aspects of BST-MOCVD process is delivery of the source materials in a way that enables reproducible stoichiometry of films. For multicomponent materials such as BST, the transport of source molecules is better to be accomplished without gas-phase association, ligand exchange and premature reaction or decomposition; all of which can cause uncontrolled fluctuations in the delivery rate of each element. As a source supply system, we adopt the liquid-source technique, in which CVD source materials are dissolved in the organic solvent. This method has an advantage of stable and efficient supply of source materials [30, 31, 32]. We use tetrahydrofuran (THF) as the organic solvent for liquid-source MOCVD.

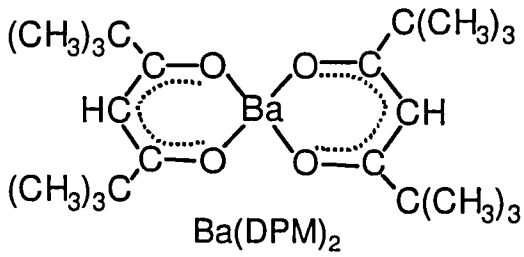

Ba(DPM)$_2$

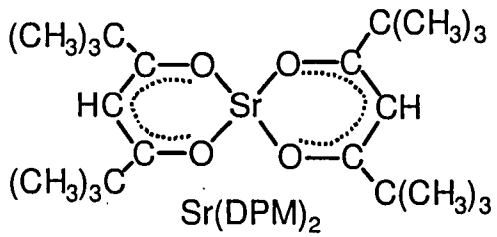

Sr(DPM)$_2$

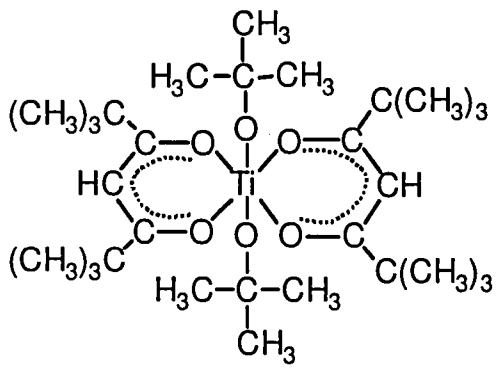

Ti(t-BuO)$_2$(DPM)$_2$

Figure 1.4: Molecular structure of the CVD source materials: Ba(DPM)$_2$, Sr(DPM)$_2$ and Ti(t-BuO)$_2$(DPM)$_2$.

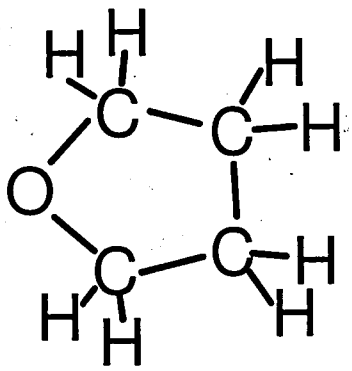

Figure 1.5: Organic solvent: tetrahydrofuran (THF).

The molecular structure of THF is shown in Fig. 1.5. Matsuno *et al.* proposed that the effect of the THF addition is caused by the formation of an additional coordinate bond between $Ba(DPM)_2$ and THF, and realized stable vaporization and smooth transportation of $Ba(DPM)_2$ by the addition of THF vapor [31, 32]. According to the thermal gravimetric analysis by Paw *et al.*, the THF ligands dissociate from $Ba(DPM)_2$ and $Sr(DPM)_2$ at the typical temperature for the deposition of BST [33]. Therefore, THF molecules are not incorporated into the deposited BST films.

1.3 Spectroscopic diagnoses

The requirements for the development of the BST capacitor for memories are: improving the dielectric constant, step coverage, leakage current, uniformity of the large area deposition, and reproducibility of the film quality. These film characteristics were reported to be greatly affected by the deposition conditions, which include the deposition temperature, the pressure in the reactor, the flow rate of the source materials and oxidizer, and the kind of oxidation gas [7, 11, 17]. Since the chemistries in MOCVD processing for the deposition of BST films are not well investigated, the required film qualities

and reproducibility are not yet obtained. In order to solve these problems, it is inevitably necessary to understand the chemistries in the MOCVD of BST films. For the elucidation of the deposition mechanism of BST films, we carry out *in situ* measurements of MOCVD processing for BST films. As a diagnostic method, we employ spectroscopic techniques such as infrared absorption spectroscopy and microdischarge optical emission spectroscopy (μD-OES). This μD-OES is a novel technique for the diagnosis of MOCVD processes that we develop in this work.

1.3.1 *In situ* infrared absorption spectroscopy

We employ *in situ* Fourier transform infrared (FT-IR) spectroscopy for the diagnosis in MOCVD of BST films under actual CVD conditions. Infrared absorption frequencies depend on the masses of atoms involved in the various vibrational motions, and on the force constant and geometry of the bonds connecting them; band shapes are determined by the rotational structure and hence by the molecular symmetry and moments of inertia. Thus, the rovibrational spectrum of a gas provides direct molecular structural information, resulting in very high specificity. The vibrational spectrum of any molecule is unique, except for those of optical isomers. Every molecule, except homonuclear diatomics such as O_2, N_2, and the halogens, has at least one vibrational absorption in the infrared region (from 200 cm^{-1} to 4000 cm^{-1}). In this manner, FT-IR spectroscopy is broadly applicable to analyses of molecular species and their quantification. Moreover, FT-IR spectroscopy is non-destructive, so this technique is very powerful for *in situ* diagnosis of chemical reactions in various CVD processes. Many examples of this diagnosis of MOCVD processes were reported for ZrO_2 films [34], SnO_2 films [35], GaAs films [36], Al films [37], Al_2O_3 films [38], Cu films [39, 40, 41, 42], and high-T_c superconducting $YBa_2Cu_3O_{7-x}$ films [43, 44, 45, 46].

1.3.2 Microdischarge optical emission spectroscopy

In this study, we employ another spectroscopic technique for the elucidation of deposition mechanism of BST films in addition to FT-IR spectroscopy. As another spectroscopic technique, we develop a novel diagnostic tool, microdis-

charge optical emission spectroscopy (μD-OES) sensor system and apply it to the diagnosis of MOCVD of BST films. There are some attempts to obtain information about film-deposition mechanism from the emission spectra of plasmas excited in the processes [47, 48, 49, 50, 51], but those are far from the purpose of elucidating chemistries in those processes. We show that it is possible to estimate the degree of thermal decomposition of the CVD source molecules from the emission spectra of the small plasma excited in the μD-OES sensor head. We also investigate oxidation reactions of the source molecules and reactions among source molecules with different metal atoms. Moreover by using this technique, we can estimate the gas temperature and the spatial distribution of the source molecules. The gas temperature is estimated form the rotational temperature of molecular nitrogen, the carrier gas of the CVD sources. The gas temperature is very important parameter to understand the gas-phase chemistry, and the information concerning the spatial distribution of the source molecules is necessary to realize uniformity of the large area deposition.

1.4 Scope and constitution of this thesis

In recent years, many research groups are making aggressive efforts to develop BST-DRAMs, but they have not succeeded in putting BST-DRAMs into practical market as manufacturing products yet. It is partly because they cannot realize the reproducibility of film qualities required for practical products. Moreover, the room of improvement is still left in regard to step coverage and electrical properties such as dielectric constant. We think it is because the chemical reactions in the deposition process of BST films were not understood enough.

In this work, we elucidate chemical reactions in MOCVD of BST films by using spectroscopic techniques. *In situ* FT-IR spectroscopy is employed for the diagnosis of MOCVD of BST films under actual CVD conditions. We can obtain much valuable knowledge about the deposition mechanisms of BST films using this infrared absorption spectroscopy. But, it is impossible to obtain all information of chemistries for the development of BST-DRAMs by only one technique. Therefore, in addition to FT-IR spectroscopy, we apply

another new spectroscopic technique, which is named μD-OES, to the elucidation of deposition mechanism of BST films. These techniques employed in this study can be applied to the diagnosis in the MOCVD process of other oxide films such as lead zirconate titanate $Pb(Zr,Ti)O_3$ [PZT], strontium bismuth tantalate $SrBi_2Ta_2O_9$ [SBT] and bismuth titanate $Bi_4Ti_3O_{12}$ [BIT], which are ferroelectric substances for non-volatile Ferroelectric Random Access Memory (FeRAM) that have attracted a great deal of attention because of those promising applications such as an electronic money card.

Contents of this thesis are shown as following short descriptions:

Chapter 2 The thermal decompositions of the source molecules for MOCVD of BST films are investigated under actual CVD conditions by using *in situ* Fourier transform infrared (FT-IR) spectroscopy. From the temperature dependence of the IR absorbance, we investigate the thermal stability of the chemical bonds in the source molecules. The obtained FT-IR data are correlated with the characteristics of the deposited BST films, which reveals that the deposition of Ti atoms does not require the complete decomposition of $Ti(t\text{-}BuO)_2(DPM)_2$ molecules in the gas phase although $Sr(DPM)_2$ and $Ba(DPM)_2$ molecules decompose completely in the gas phase before Sr and Ba atoms are incorporated in the films. In this chapter, the effects of these thermal decompositions on the deposition mechanism of BST films are discussed.

Chapter 3 Microdischarge optical emission spectroscopy (μD-OES) is developed as a novel diagnostic tool for analyzing chemical reactions in MOCVD of BST films. The thermal decompositions of the CVD source molecules are investigated from the observed emission spectra of the small plasma exited at the μD-OES sensor head. The results obtained by μD-OES measurements are discussed with referring to *in situ* FT-IR spectroscopic measurements. The oxidation of the source molecules in the gas phase is investigated by observing the change in the emission spectra due to the addition of oxygen gas. We also study interaction between source molecules with the different metal atoms. Additionally, the gas temperature and the spatial distribution of the source molecules

are measured using the μD-OES.

Chapter 4 The oxidation reactions of source Ti(t-BuO)$_2$(DPM)$_2$ and Sr(DPM)$_2$ molecules during MOCVD process are studied by *in situ* FT-IR spectroscopy. We use O_2 and N_2O gases as oxidizing agents and investigate the difference in oxidation effect between the two gases. From measurements of IR absorption spectra, it is shown that O_2 is more reactive than N_2O in the gas phase, and selectively attacks low-electron-density sites in the source molecules. We deposit strontium oxide (Sr_xO_y) and BST films in O_2 and N_2O ambients, and investigate the relationship between the qualities of deposited films and the gas-phase reactions measured by FT-IR spectroscopy. In terms of the suppression of carbon contamination and the controllability of the atomic composition ratio of deposited films, we determine which oxidation gas is more suitable for the preparation of BST films.

Chapter 5 The results of these spectroscopic measurements reveal that the addition of oxidation gas has more effects on the creation of Sr precursors than that of Ti precursors. On the basis of these experimental findings, we propose how the precursors for each metal element are formed from the source molecules in the gas phase. In this chapter, we deposit strontium oxide, titanium oxide and strontium titanate films under various deposition conditions, and study the effect of oxidation gas on the deposition chemistry in order to verify above proposition on the mechanism of the precursor formation. Moreover, isotopic ^{18}O-labeled experiments are performed to understand the deposition mechanism of BST films in more detail.

Chapter 6 Conclusions of this work and prospects for future works are summarized.

References

[1] T. Takemitsu and S. Ohya: OYO BUTURI **65** (1996) 1106.

[2] Y. Kato and N. Kasai: OYO BUTURI **67** (1998) 1239.

[3] T. Horikawa, N. Mikami, T. Makita, J. Tanimura, M. Kataoka, K. Sato and M. Nunoshita: Jpn. J. Appl. Phys. **32** (1993) 4126.

[4] M. Izuha, K. Abe and N. Fukushima: Jpn. J. Appl. Phys. **36** (1997) 5866.

[5] S. Ohfuji, M. Itsumi and H. Akiya: Jpn. J. Appl. Phys. **36** (1997) 5854.

[6] T. Kawahara, M. Yamamuka, T. Makita, J. Naka, A. Yuuki, N. Mikami and K. Ono: Jpn. J. Appl. Phys. **33** (1994) 5129.

[7] T. Kawahara, M. Yamamuka, T. Makita, K. Tsutahara, A. Yuuki, K. Ono and Y. Matsui: Jpn. J. Appl. Phys. **33** (1994) 5897.

[8] T. Kawahara, M. Yamamuka, T. Makita, A. Yuuki, N. Mikami and K. Ono: Mat. Res. Soc. Symp. Proc. **361** (1995) 361.

[9] T. Kawahara, M. Yamamuka, A. Yuuki, N. Mikami and K. Ono: Jpn. J. Appl. Phys. **34** (1995) 5077.

[10] M. Yamamuka, T. Kawahara, T. Makita, A. Yuuki and K. Ono: Jpn. J. Appl. Phys. **35** (1996) 729.

[11] M. Yamamuka, T. Kawahara, A. Yuuki and K. Ono: Jpn. J. Appl. Phys. **35** (1996) 2530.

[12] T. Kawahara, M. Yamamuka, A. Yuuki and K. Ono: Jpn. J. Appl. Phys. **35** (1996) 4880.

[13] M. Yamamuka, T. Kawahara, T. Horikawa and K. Ono: Jpn. J. Appl. Phys. **36** (1997) 2555.

[14] M. Tarutani, M. Suita, T. Horikawa, J. Tanimura, T. Kawahara, M. Yamamuka, H. Sumitani and K. Ono: Jpn. J. Appl. Phys. **37** (1998) 1328.

[15] M. Yamamuka, T. Kawahara, M. Tarutani, T. Horikawa, T. Oomori and K. Ono: J. Appl. Phys. **86** (1999) 1082.

[16] T. Kawahara, S. Matsuno, M. Yamamuka, M. Tarutani, T. Sato, T. Horikawa, F. Uchikawa and K. Ono: Jpn. J. Appl. Phys. **38** (1999) 2205.

[17] M. Kiyotoshi, K. Eguchi, K. Imai and T. Arikado: Jpn. J. Appl. Phys. **37** (1998) 4487.

[18] Y. Takeshima, K. Shiratsuyu, H. Takagi and Y. Sakabe: Jpn. J. Appl. Phys. **36** (1997) 5870.

[19] Y. Takeshima, K. Tanaka and Y. Sakabe: Jpn. J. Appl. Phys. **39** (2000) 5389.

[20] C. S. Kang, H.-J. Cho, C. S. Hwang, B. T. Lee, K.-H. Lee, H. Horii, W. D. Kim, S. I. Lee and M. Y. Lee: Jpn. J. Appl. Phys. **36** (1997) 6946.

[21] H. Funakubo, D. Nagano, A. Saiki, Y. Inagaki, K. Shinozaki and N. Mizutani: Jpn. J. Appl. Phys. **36** (1997) 5879.

[22] Y.-C. Choi, J. Lee and B.-S Lee: Jpn. J. Appl. Phys. **36** (1997) 6824.

[23] Y. Tasaki, S. Yoshizawa and M. Satoh: Jpn. J. Appl. Phys. **37** (1998) 649.

[24] J.-C. Lee and S.-G Yoon: J. Vac. Sci. Technol. B **17** (1999) 2182.

[25] J.-H. Ahn, P. C. Mclntyre, L. W. Mirkarimi, S. R. Gilbert, J. Amano and M. Schulberg: Appl. Phys. Lett. **77** (2000) 1378.

[26] P. C. Mclntyre, J.-H. Ahn, R. J. Becker, R.-V. Wang, S. R. Gilbert, L. W. Mirkarimi, M. T. Schulberg: J. Appl. Phys. **89** (2001) 6378.

[27] M. Yoshida, H. Yamaguchi, T. Sakuma and Y. Miyasaka: J. Electrochem. Soc. **142** (1995) 244.

[28] S. Sone, H. Yabuta, Y. Kato, T. Iizuka, S. Yamamichi, H. Yamaguchi, P.-Y. Lesaicherre, S. Nishimoto and M. Yoshida: Jpn. J. Appl. Phys. **35** (1996) 5089.

[29] S. Sone, R. Akahane, K. Arita, H. Yabuta, S. Yamamichi, M. Yoshida and Y. Kato: Jpn. J. Appl. Phys. **38** (1999) 2200.

[30] P. H. Dickinson, T. H. Geballe, A. Sanjurjo, D. Hildenbrand, G. Craig, M. Zisk, J. Collman, S. A. Banning and R. E. Sievers: J. Appl. Phys. **66** (1989) 444.

[31] S. Matsuno, F. Uchikawa and K. Yoshizaki: Jpn. J. Appl. Phys. **29** (1990) L947.

[32] S. Matsuno, F. Uchikawa and K. Yoshizaki: *Proceedings of the 2nd International Symposium on Superconductivity* (Tsukuba, Japan, 1990) p. 877.

[33] W. Paw, T. H. Baum, K.-C. Lam and A. L. Rheingold: Inorg. Chem. **39** (2000) 2011.

[34] M. A. Cameron and S. M. George: Thin Solid Films. **348** (1999) 90.

[35] V. Hopfe, W. Grahlert and O. Throl: J. Phys. IV **9** (1999) 995.

[36] Q. Fu, L. Li, M. J. Begarney, B.-K. Han, D. C. Law and R. F. Hicks: J. Phys. IV **9** (1999) 3.

[37] J.-H. Lee, M.-Y. Park, J.-H. Yun and S.-W. Rhee: Thin Solid Films **348** (1999) 130.

[38] G. A. Battiston, G. Carta, R. Gerbasi, M. Porchia, L. Rizzo and G. Rossetto: J. Phys. IV **9** (1999) 675.

[39] B. Zheng, G. Braeckelmann, K. Kujawski, I. Lou, S. Lane and A. E. Kaloyeros: J. Electrochem. Soc. **142** (1995) 3896.

[40] K. Hanaoka, H. Ohnishi and K. Tachibana: Jpn. J. Appl. Phys. **32** (1993) 4774.

[41] K. Hanaoka, H. Ohnishi and K. Tachibana: Thin Solid Films **262** (1995) 209.

[42] K. Hanaoka, H. Ohnishi and K. Tachibana: Jpn. J. Appl. Phys. **34** (1995) 2430.

[43] M. L. Hitchman, S. H. Shamlian, G. G. Condorelli and F. Chabert-Rocabois: J. Alloys Compd. **251** (1997) 297.

[44] H. Harima, H. Ohnishi, K. Hanaoka, K. Tachibana, M. Kobayashi and S. Hoshinouchi: Jpn. J. Appl. Phys. **29** (1990) 1932.

[45] H. Harima, H. Ohnishi, K. Hanaoka, K. Tachibana and Y Goto: Jpn. J. Appl. Phys. **30** (1991) 1946.

[46] K. Hanaoka, H. Ohnishi and K. Tachibana: Physica C **190** (1991) 145.

[47] D. E. Donohue, J. A. Schiavone and R. S. Freund: J. Chem. Phys. **67** (1977) 769.

[48] J. Sakai, K. Kato, K. Hirama, S. Murakami and T. Ishida: J. Cryst. Growth **95** (1989) 621.

[49] H. Harima, H. Ohnishi, K. Hanaoka, K. Tachibana, M. Kobayashi and S. Hoshinouchi: Jpn. J. Appl. Phys. **29** (1990) 1932.

[50] K. Ebihara, S. Kanazawa and T. Ikegami: J. Appl. Phys. **68** (1990) 1151.

[51] G. J. Orloff: J. Vac. Sci. & Technol. A **10** (1992) 3065.

Chapter 2

Infrared spectroscopic study of thermal decompositions of CVD sources

2.1 Introduction

In recent years, scientists have participated in the development of new capacitor dielectrics for Gbit-scale dynamic random access memory (DRAM). Barium strontium titanate (Ba,Sr)TiO_3 [BST] film is regarded as one of the most promising capacitor dielectrics because of its high dielectric constant and paraelectric properties around room temperature. As a technique for preparation of BST films, metalorganic chemical vapor deposition (MOCVD) are employed, because it has many advantages such as excellent step coverage [1, 2, 3, 4]. BST-DRAM has not been manufactured for practical use yet, because the reproducibility of the good quality required for the fabrication of actual memory cell remains to be achieved. In order to solve these problems, it is necessary to investigate reaction mechanisms in the MOCVD of BST films. In this study, *in situ* Fourier transform infrared (FT-IR) spectroscopy

is applied to the diagnosis in MOCVD of BST films under actual CVD conditions. Although H.-K. Ryu *et al* applied an FT-IR spectroscopy to the diagnosis of source molecules for BST films such as Ti(*i*-PrO)$_2$(DPM)$_2$ and Sr(DPM)$_2$ [5, 6], their study was not carried out under actual CVD conditions. They analyzed solid source materials by the KBr disk method. This study is the first application of *in situ* FT-IR spectroscopy to the diagnosis in the MOCVD process for BST films. We observe the temperature dependence of the IR absorbance, and investigate the thermal decomposition schemes of the source materials. The correlation between the thermal decomposition in the gas phase and the incorporation rate in the deposited BST films is investigated, and the deposition mechanism of BST films is discussed.

2.2 Experimental

Figure 2.1 shows a schematic diagram of the liquid-source MOCVD apparatus and setup of *in situ* FT-IR spectrometer. As the CVD source materials, bis(dipivaloylmethanato)barium [Ba(DPM)$_2$], bis(dipivaloylmethanato)strontium [Sr(DPM)$_2$], and bis(*tertiary*-butoxy)bis(dipivaloylmethanato)titanium [Ti(*t*-BuO)$_2$(DPM)$_2$] were used. Molecular structures are shown in Fig. 1.4 (see Chap. 1). These source materials were dissolved in the organic solvent tetrahydrofuran (THF). The concentration of each source solution was 0.1 mol/*l*. The dissolved sources were introduced into a vaporizer by N_2 carrier gas at 200 sccm. The temperature of the vaporizer was maintained at 245°C. The vaporized sources were transported into a hot-wall CVD reactor and subsequently mixed with O_2 oxidant gas. The temperature of the transport line from the vaporizer to the CVD reactor was maintained at 250°C to prevent source materials from condensing. The mixture gas was sprayed over a substrate through a screening plate and showerhead nozzles.

A schematic diagram of the setup of *in situ* FT-IR spectrometer is also shown in Fig. 2.1. A Mercury Cadmium Tellurium (MCT) detector was used and the resolution was set to 2 cm^{-1}. We observed the IR absorption spectra at the wavenumber between 400 cm^{-1} and 4000 cm^{-1} under actual CVD conditions. The IR beam covers almost the entire region between the

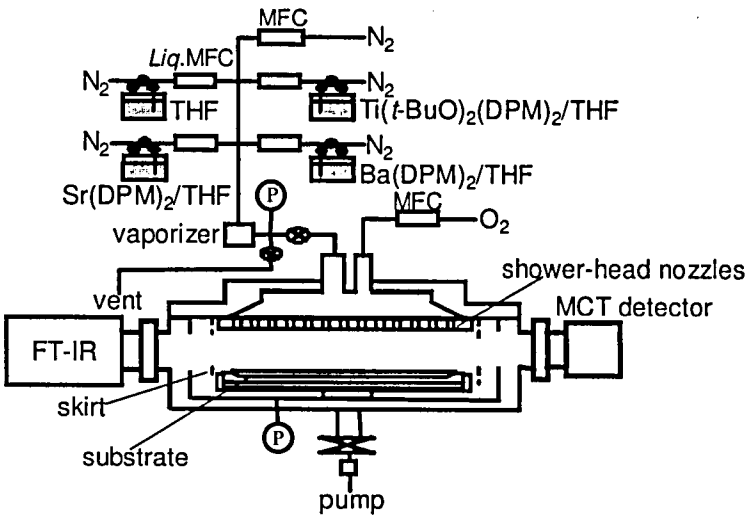

Figure 2.1: Schematic diagram of the liquid-source MOCVD apparatus with an FT-IR spectrometer.

shower-head plate and the substrate. Since there was no IR absorption when only the substrate with a deposited film was placed without supplying source gases, we safely confirmed that the detected IR absorption did not involve the reflection absorption due to the deposited film. The pressure in the reactor was maintained at 10 Torr, which is in the pressure range for the deposition of BST films. The gas temperature at the middle point between the shower-head plate and the substrate can be measured from the simulation of the unresolved rotational structure of the emission spectrum of the carrier N_2 gas by microdischarge optical emission spectroscopy (μD-OES). An approximately linear relationship between the gas temperature and the substrate temperature was obtained in the substrate temperature range between 250°C and 550°C (see Fig. 3.3 in Chap. 3). For example, when the substrate temperature was 560°C, which is the typical temperature for the deposition of BST films, the gas temperature was about 350°C.

The BST thin films were deposited on a 6-inch-diameter Si(200) substrate. The thickness of the deposited films was measured by cross-sectional scanning electron microscopy (SEM) and spectroscopic ellipsometry. The atomic composition was evaluated by X-ray photoelectron spectroscopy (XPS) after etching of the films' surfaces.

2.3 Results and Discussion

2.3.1 *In situ* measurement of IR absorption spectra

We carried out *in situ* measurements of the IR absorption spectra of Ti(*t*-BuO)$_2$(DPM)$_2$, Sr(DPM)$_2$ and Ba(DPM)$_2$. The observed IR spectra in the absorbance mode at the substrate temperature of 240°C, which was the same as the temperature of the vaporizer, are shown in Fig. 2.2. These spectra were obtained by subtracting the THF absorption from the observed spectra. These spectra obtained by *in situ* FT-IR spectroscopy were the same as those measured by the KBr disk method at room temperature. It was confirmed that source molecules are transported into the reactor without thermal decomposition. The peaks between 630 cm^{-1} and 700 cm^{-1} and the peak at 720 cm^{-1} are due to CO_2 and H_2O molecules, respectively.

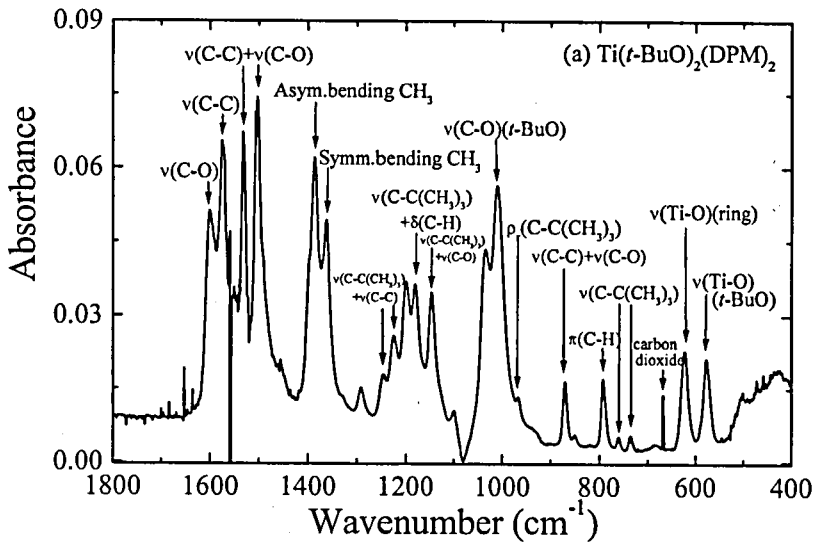

Figure 2.2: IR spectra of Ti(t-BuO)$_2$(DPM)$_2$, Sr(DPM)$_2$ and Br(DPM)$_2$ observed under actual CVD conditions at the substrate temperature of 242°C: (a) Ti(t-BuO)$_2$(DPM)$_2$, (b) Sr(DPM)$_2$ and (c) Br(DPM)$_2$. The assignment of each peak is also shown. The vibration mode is as follows: ν: stretching mode, δ: in-plane bending mode, ρ_r: rocking mode and π: out-of-plane bending mode.

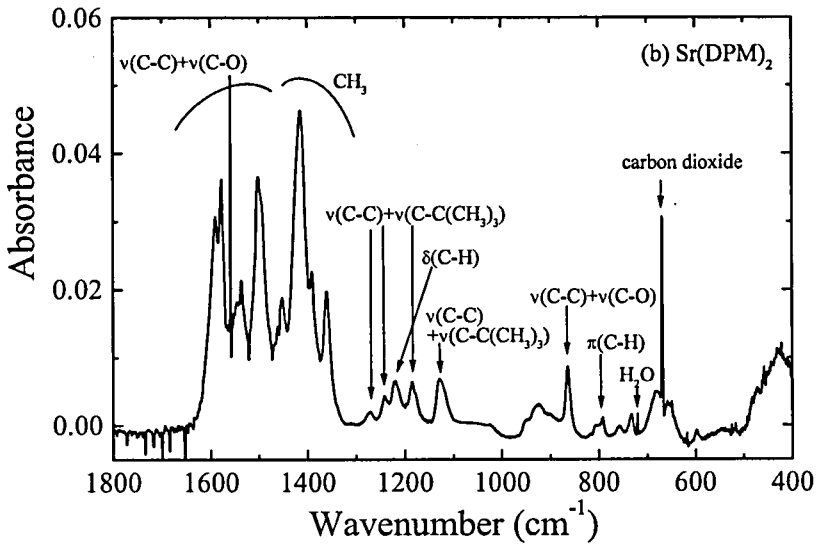

Figure 2.2: IR spectra of Ti(t-BuO)$_2$(DPM)$_2$, Sr(DPM)$_2$ and Br(DPM)$_2$ observed under actual CVD conditions at the substrate temperature of 242°C: (a) Ti(t-BuO)$_2$(DPM)$_2$, (b) Sr(DPM)$_2$ and (c) Br(DPM)$_2$. The assignment of each peak is also shown. The vibration mode is as follows: ν: stretching mode, δ: in-plane bending mode, ρ_r: rocking mode and π: out-of-plane bending mode.

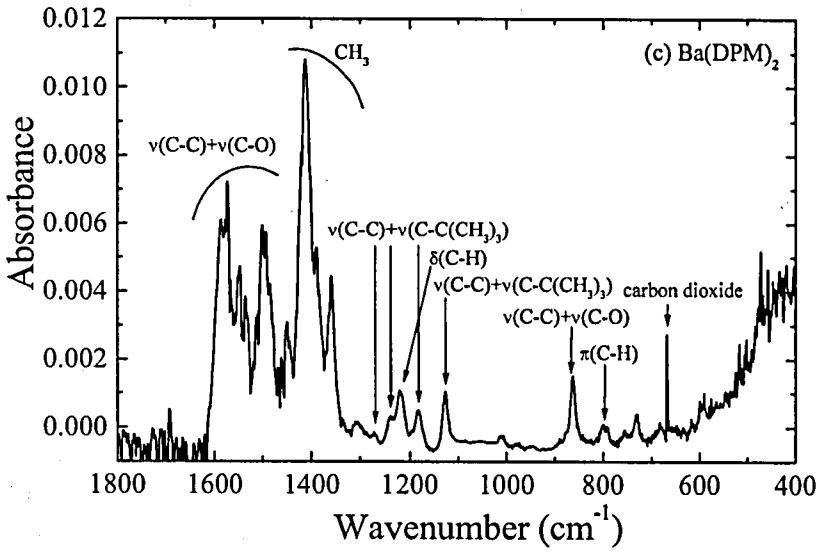

Figure 2.2: IR spectra of Ti(t-BuO)$_2$(DPM)$_2$, Sr(DPM)$_2$ and Br(DPM)$_2$ observed under actual CVD conditions at the substrate temperature of 242°C: (a) Ti(t-BuO)$_2$(DPM)$_2$, (b) Sr(DPM)$_2$ and (c) Br(DPM)$_2$. The assignment of each peak is also shown. The vibration mode is as follows: ν: stretching mode, δ: in-plane bending mode, ρ_r: rocking mode and π: out-of-plane bending mode.

The assignment of each peak is also shown in Fig. 2.2. The assignment of the peaks of Ti(t-BuO)$_2$(DPM)$_2$ was carried out by consulting many papers [5, 7, 8, 9, 10, 11, 12]. Moreover, the assignment of the IR peaks at 577 cm^{-1}, 623 cm^{-1} and 1010 cm^{-1} were revised on the basis of the density functional theory (DFT) calculations [13]. This new assignment shows that these 577 cm^{-1}, 623 cm^{-1} and 1010 cm^{-1} lines are mainly due to the stretching mode of the Ti-O bond in the t-butoxy group, the Ti-O bond in the DPM chelate ring and the C-O bond in the t-butoxy group, respectively.

As a result of the DFT calculations, new assignments for the IR peaks at 577 cm^{-1} and 623 cm^{-1} were found. While both peaks were conventionally assigned to the coupling modes between the chelate ring deformation and Ti-O stretching mode [5], these new assignments made it possible to elucidate the difference in the reactivity between the β-diketone chelate rings and the alkoxy groups of the Ti source molecules such as Ti(t-BuO)$_2$(DPM)$_2$. The assignment of these peaks is one of the most important and interesting issues in discussing the thermal decomposition scheme of Ti(t-BuO)$_2$(DPM)$_2$. In order to confirm the above assignment, we compared IR spectra between Ti(i-BuO)$_2$(DPM)$_2$ and Ti(t-PrO)$_2$(DPM)$_2$. Figure 2.3 shows IR spectra of Ti(i-BuO)$_2$(DPM)$_2$ and Ti(t-PrO)$_2$(DPM)$_2$ measured by the KBr disk method. The IR spectrum of Ti(i-PrO)$_2$(DPM)$_2$ has corresponding peaks at 628 cm^{-1} and 585 cm^{-1}, respectively. The positions of the lower wavenumber peaks show a larger discrepancy as compared with that at the higher wavenumber. The substitution of the alkoxy groups from heavier t-butoxy groups to lighter i-propoxy groups has little influence on the position of the peak due to the Ti-O vibrations in the β-diketone chelate rings, while this substitution significantly shifts the peak due to Ti-O vibrations in the alkoxy groups to the higher wavenumber position. This dependence of the peak position on the type of alkoxy group corresponds to the above assignment determined by the DFT calculations.

The absorption peaks of Sr(DPM)$_2$ and Ba(DPM)$_2$ were also assigned by consulting previous papers [14, 6]. Although a strong absorption peak at 1010 cm^{-1} was observed in the spectrum of Ti(t-BuO)$_2$(DPM)$_2$, the corresponding absorption was not found in the spectra of Sr(DPM)$_2$ and Ba(DPM)$_2$. This difference suggests that the absorption peak at 1010 cm^{-1}

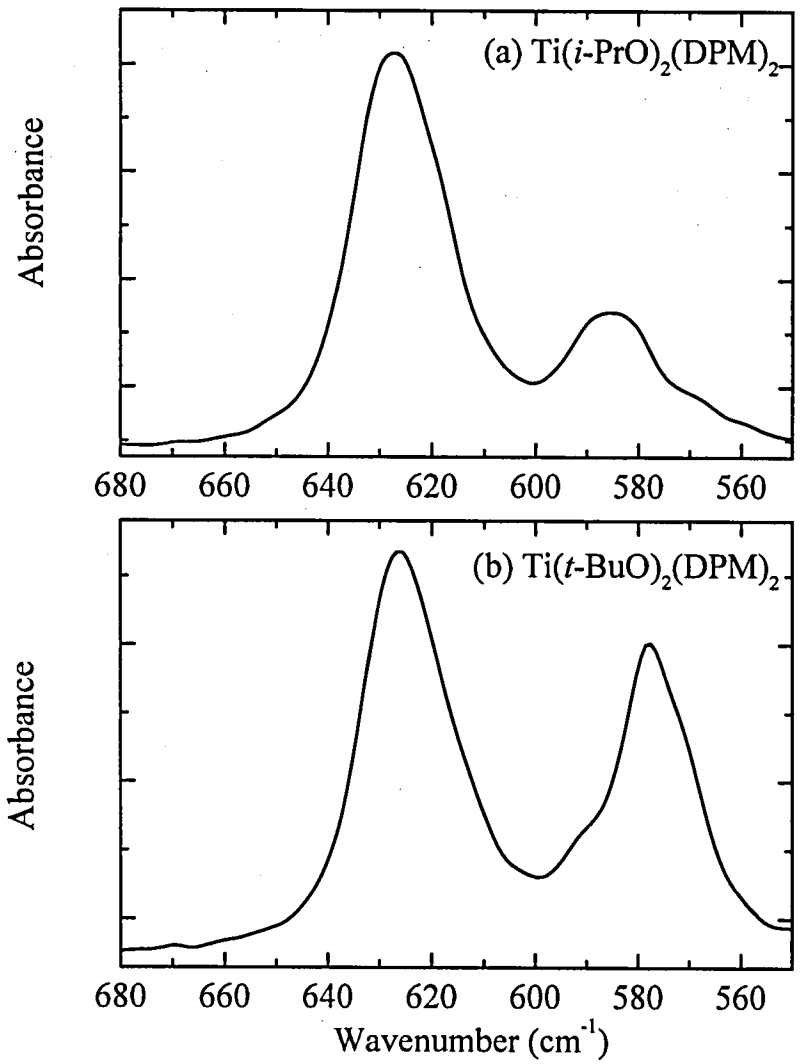

Figure 2.3: Comparison of IR spectra measured by KBr disk method: (a) $Ti(i\text{-}BuO)_2(DPM)_2$ and (b) $Ti(t\text{-}PrO)_2(DPM)_2$.

is derived from the *t*-butoxy group of Ti(*t*-BuO)$_2$(DPM)$_2$.

2.3.2 Thermal decomposition of Ti(*t*-BuO)$_2$(DPM)$_2$ molecules

From the temperature dependence of the FT-IR spectrum, the decomposition scheme of Ti(*t*-BuO)$_2$(DPM)$_2$ molecules were investigated. Figure 2.4 shows the temperature dependence of the absorbance at the substrate temperature between 240°C and 637°C. As the substrate temperature increased, the absorbance derived from Ti(*t*-BuO)$_2$(DPM)$_2$ molecules decreased. This decrease is due to the thermal decomposition of Ti(*t*-BuO)$_2$(DPM)$_2$ molecules. When the substrate temperature was above 480°C, the absorption peak at 889 cm^{-1} and the broad peak at the vicinity of 1710 cm^{-1} appeared. The 889 cm^{-1} peak is assigned to the C-C-H out-of-plane bending mode of *i*-butene [15] and the 1710 cm^{-1} peak is assigned to the stretching mode of the C=O double bond of the products generated by the gas-phase reactions. The appearance of the 889 cm^{-1} peak corresponds to the dissociation of the *t*-butoxy group from the chelate ring.

Figure 2.5 shows the temperature dependence of the normalized absorbance of the IR peaks with high intensity. On the basis of the temperature dependence of their peak intensities, these absorption peaks are classified into three groups. The first is the group of peaks which started to decrease at the highest temperature of 400°C. This group includes the 577 cm^{-1} peak which is assigned to the Ti-O stretching mode of the *t*-butoxy group and the 623 cm^{-1} peak which is assigned to the Ti-O stretching mode of the DPM chelate ring. This result indicates that Ti-O bonds in the chelate ring and *t*-butoxy group are the most stable against the thermal decomposition. The second is the group of peaks which decreased the most drastically. This group includes the 759 cm^{-1} peak, which is assigned to the stretching mode of the C-C(CH$_3$)$_3$ bond, and the 792 cm^{-1} peak, which is assigned to the out-of-plane bending mode of the C-H bond. This result indicates that the C-C(CH$_3$)$_3$ bond is easier to cleave than any other bonds of Ti(*t*-BuO)$_2$(DPM)$_2$ molecules. The weakness of the C-H bond connecting to the chelate ring or the change in the C-H vibration mode derived from cleaving the C-C(CH$_3$)$_3$

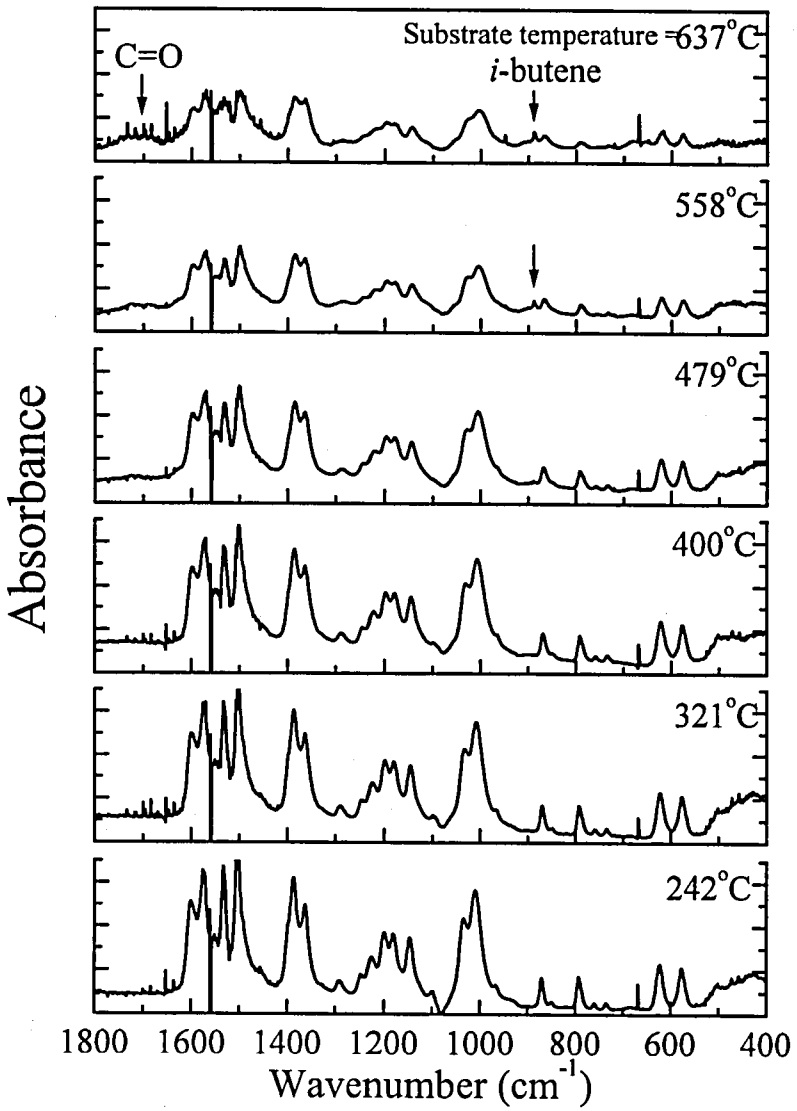

Figure 2.4: Changes in the absorbance of $Ti(t\text{-}BuO)_2(DPM)_2$ when the substrate temperature was varied from 240°C to 637°C.

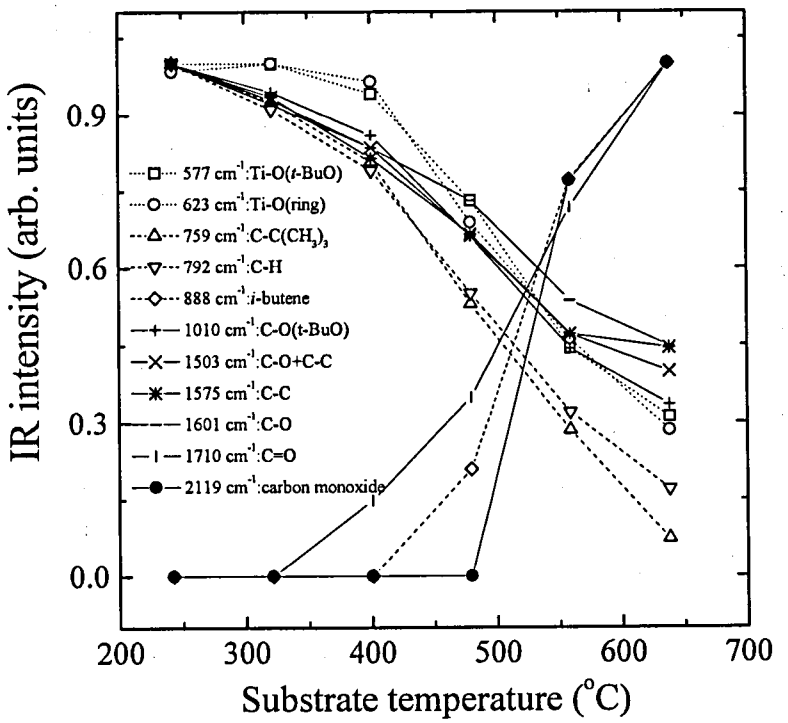

Figure 2.5: Temperature dependence of the normalized IR absorption peak intensities of Ti(t-BuO)$_2$(DPM)$_2$.

bond may be responsible for the decrease of the absorbance at 792 cm^{-1}. The third is the group of all other peaks which showed almost the same moderate temperature dependence. This group includes the 1010 cm^{-1} peak which is assigned to the stretching mode of the C-O bond of the *t*-butoxy group and the 1503 cm^{-1} peak which is assigned to the coupling of the stretching modes of the C-C bond and the C-O bond in the chelate ring. This indicates that the bonds assigned to these peaks are more difficult to cleave than the C-C$(CH_3)_3$ bond and the C-H bond connecting to the chelate ring and easier to cleave than the Ti-O bonds.

On the basis of the observed difference in the temperature dependence of the IR absorbance, we proposed the thermal decomposition scheme of the Ti(*t*-BuO)$_2$(DPM)$_2$ molecule shown in Fig. 2.6. In the first step of the thermal decomposition, the *t*-butyl group is dissociated from the DPM chelate ring (step 1). As the temperature increases, the C-C and the C-O bonds in the chelate ring and the C-O bond in the *t*-butoxy group cleave at almost the same temperature (step 2). The Ti-O bonds in the chelate rings and those in connection with the *t*-butoxy groups are found to be the most difficult to cleave among all the bonds of Ti(*t*-BuO)$_2$(DPM)$_2$ molecule.

2.3.3 Thermal decomposition of Sr(DPM)$_2$ and Ba(DPM)$_2$

We also observed the temperature dependence of the absorption spectrum of Sr(DPM)$_2$, which is shown in Fig. 2.7. Figure 2.8 shows the temperature dependence of the IR absorbance. As the temperature increases, the IR absorbance of Sr(DPM)$_2$ decreases more drastically than that of Ti(*t*-BuO)$_2$(DPM)$_2$ and was completely quenched above 450°C. This indicates that Sr(DPM)$_2$ is much easier to decompose thermally than Ti(*t*-BuO)$_2$(DPM)$_2$ in the gas phase and that the DPM chelate ring of Sr(DPM)$_2$ decomposes completely above 450°C. The obvious difference in the temperature dependence of the IR absorbance at various wavenumbers could not be found. At the substrate temperature of 640°C, the absorption peak at 889 cm^{-1} and the broad peak at the vicinity of 1710 cm^{-1} appeared, which were much smaller than those of Ti(*t*-BuO)$_2$(DPM)$_2$. We also observed the

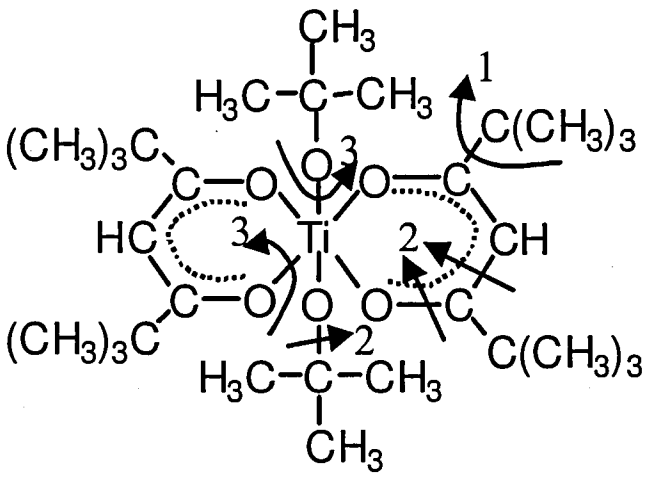

Figure 2.6: Schematic diagram of the thermal decomposition scheme of Ti(t-BuO)$_2$(DPM)$_2$ molecule. Marker 1 denotes the bond which cleaves at the first step of the thermal decomposition (step 1). Marker 2 denotes the bonds which cleave at the second step (step 2). Marker 3 denotes the bonds which are the most difficult to cleave among all the bonds of the Ti(t-BuO)$_2$(DPM)$_2$ molecule.

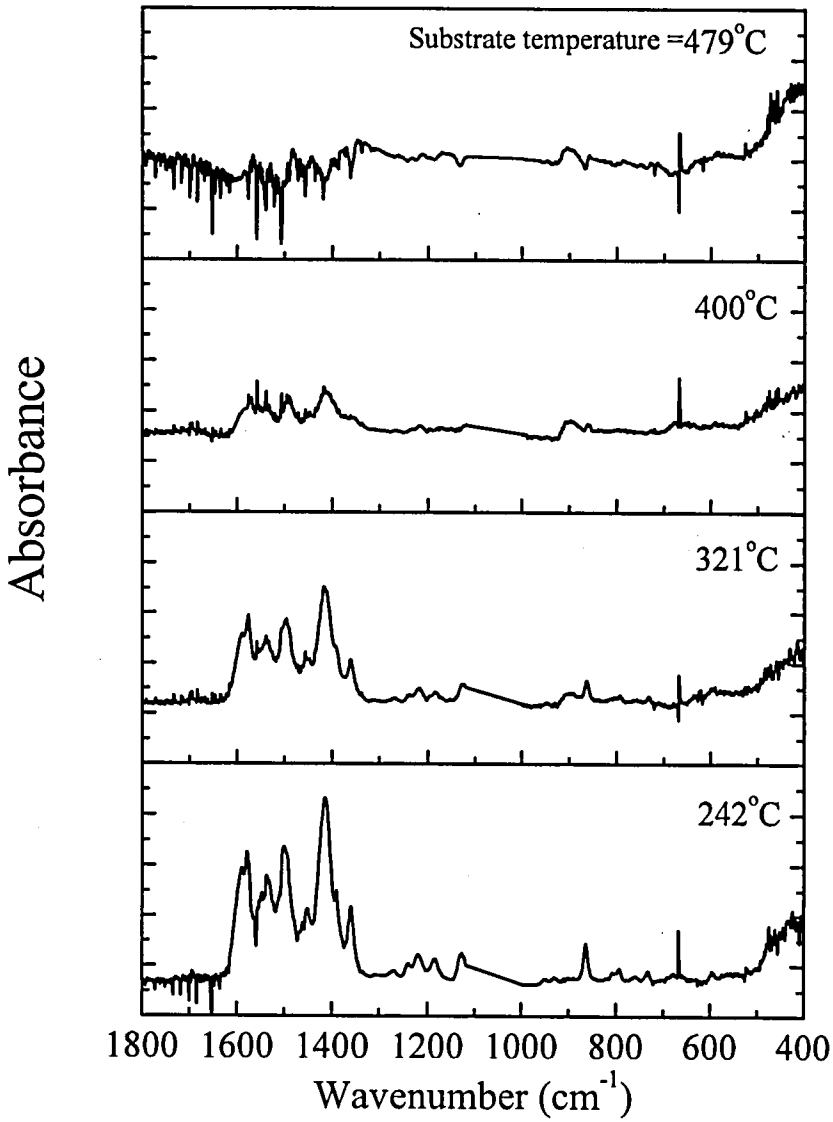

Figure 2.7: Changes in the absorbance of $Sr(DPM)_2$ when the substrate temperature was varied from 240°C to 637°C.

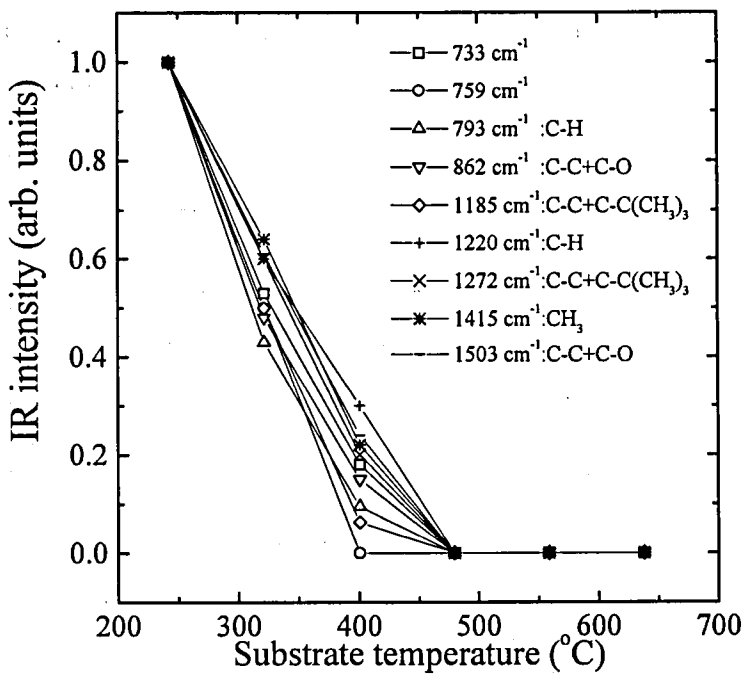

Figure 2.8: Temperature dependence of the normalized IR absorption peak intensities of $Sr(DPM)_2$.

thermal decomposition of $Ba(DPM)_2$ molecules by FT-IR absorption spectroscopy. Although the temperature dependence of the IR absorbance of $Ba(DPM)_2$ showed almost the same behavior as that of $Sr(DPM)_2$, the IR absorbance of $Ba(DPM)_2$ decreased at a slightly lower temperature than that of $Sr(DPM)_2$ (see Fig. 2.9).

This experimental finding indicates that $Ba(DPM)_2$ molecules are easier to decompose thermally than $Sr(DPM)_2$ molecules.

In alkaline-earth metal chelates such as $Sr(DPM)_2$ and $Ba(DPM)_2$, the metal-oxygen coordinate bond (M-O bond) has an ionic character rather than a covalent one. The strength of the M-O bond is in proportion to a reciprocal of the square of the distance of the M-O bond. Since the distance of the Ba-O bond is larger than that of the Sr-O bond, the Sr-O bond is stronger than the Ba-O bond. This simple argument shows good agreement with the experimental results. Since the strength of the M-O bond explains the thermal stability of $Sr(DPM)_2$ and $Ba(DPM)_2$ molecules, the cleavage of the M-O bonds is a key step in the thermal decomposition of these two alkaline-earth metal chelates. In contrast to $Sr(DPM)_2$ and $Ba(DPM)_2$, the M-O bond of $Ti(t\text{-}BuO)_2(DPM)_2$ is difficult to cleave. Because of this thermal instability of the M-O bond, $Sr(DPM)_2$ and $Ba(DPM)_2$ decompose at a much lower temperature than $Ti(t\text{-}BuO)_2(DPM)_2$.

2.3.4 Correlation between the thermal decomposition in the gas phase and the deposition of BST films

The correlation between the thermal decomposition in the gas phase and the characteristics of the deposited BST films was investigated. Figure 2.10 shows the temperature dependence of the incorporation rates of Ti, Sr and Ba atoms in the deposited BST films. For comparison, the temperature dependence of the IR absorbance of $Ti(t\text{-}BuO)_2(DPM)_2$, $Sr(DPM)_2$ and $Ba(DPM)_2$ at 1503 cm^{-1} is also indicated in Fig. 2.10. Sr and Ba atoms were incorporated in the BST films above the substrate temperature of 450°C. In this temperature region, the IR absorbance of $Sr(DPM)_2$ and $Ba(DPM)_2$ was completely quenched. This indicates that $Sr(DPM)_2$ and $Ba(DPM)_2$ molecules decompose completely in the gas phase before Sr and Ba atoms

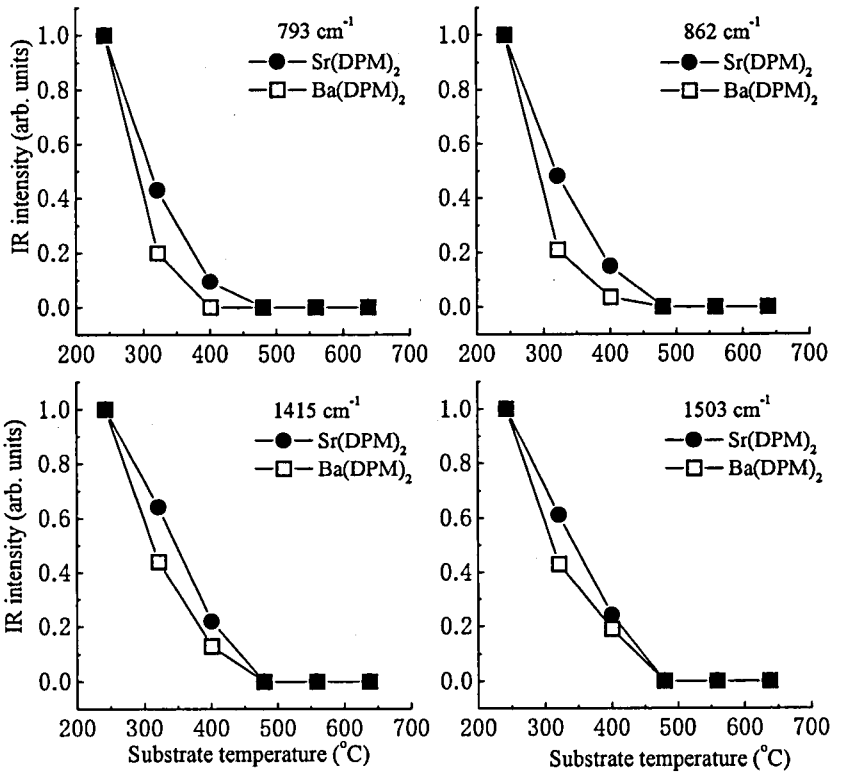

Figure 2.9: Comparison of temperature dependence of the IR absorption peak intensities between $Sr(DPM)_2$ and $Ba(DPM)_2$.

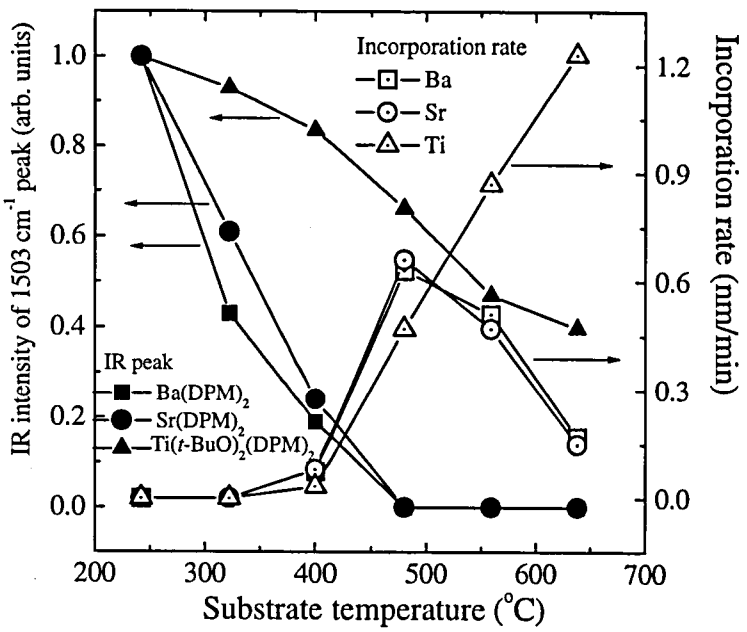

Figure 2.10: Temperature dependence of incorporation rates of Ti, Sr and Ba atoms in the deposited BST films. The temperature dependence of the IR absorbance of Ti(t-BuO)$_2$(DPM)$_2$, Sr(DPM)$_2$ and Ba(DPM)$_2$ at 1503 cm^{-1} is also indicated.

are incorporated in the film, suggesting that the precursors for the deposition of BST film may be thermally decomposed products. In contrast to Sr and Ba atoms, Ti atoms were deposited at low temperature before the IR absorbance of Ti(t-BuO)$_2$(DPM)$_2$ was completely quenched. Although Ti atoms were incorporated in the deposited BST films at the substrate temperature of 480°C, about 70% of the IR absorbance at 250°C remained. This result suggests that about 70% of Ti(t-BuO)$_2$(DPM)$_2$ molecules exist without thermal decomposition in the gas phase and that the surface reactions rather than the gas-phase reactions make a dominant contribution to the deposition of Ti atoms. These results indicate that the thermal decomposition in the gas phase has more effects on the deposition of Sr and Ba atoms than on that of Ti atoms.

While the incorporation rate of Ti atoms increased above the substrate temperature of 500°C, the incorporation rate of Sr and Ba atoms decreased. This suggests that Ti atoms are incorporated prior to Sr and Ba atoms in this temperature region and that the incorporation of Ti atoms prevents the incorporation of Sr and Ba atoms. Similar to this suggestion, Yamamuka *et al.* assumed that the decomposition products from the Ti source molecule adsorbed on the film surface prevent other precursors for Ba and Sr atoms from adhering to the surface in their surface reflection model [16]. This model was reported to be suitable to explain the CVD reaction mechanism for the BST film deposition.

2.4 Conclusions

We carried out *in situ* measurements of the IR absorption spectra of Ti(t-BuO)$_2$(DPM)$_2$ and revised the conventional assignment of the IR peaks at 577 cm^{-1}, 623 cm^{-1} and 1010 cm^{-1}. On the basis of the difference of the temperature dependence of the absorption peaks, the thermal decomposition scheme of a Ti(t-BuO)$_2$(DPM)$_2$ molecule was determined. Ti(t-BuO)$_2$(DPM)$_2$ decomposes sequentially as follows: First, the t-butyl group is dissociated from the DPM chelate ring. As the temperature increases, the C-C and C-O bonds in the chelate ring and the C-O bond in the t-butoxy group cleave at almost the same temperature. The Ti-O bonds in the chelate

ring and those in the *t*-butoxy group are the most difficult to cleave among all the bonds of the Ti(*t*-BuO)$_2$(DPM)$_2$ molecule. Additional *in situ* measurements of the IR absorption spectra of Sr(DPM)$_2$ and Ba(DPM)$_2$ revealed that Sr(DPM)$_2$ and Ba(DPM)$_2$ are much easier to decompose thermally than Ti(*t*-BuO)$_2$(DPM)$_2$. Since the thermal stability of Sr(DPM)$_2$ and Ba(DPM)$_2$ was explained by the strength of the M-O bond, the cleavage of the M-O bonds is considered to be a key step in the thermal decomposition of these two alkaline-earth metal chelates.

The correlation between the observed IR absorption spectra and the characteristics of the deposited BST films was also investigated. While Sr(DPM)$_2$ and Ba(DPM)$_2$ molecules decompose completely in the gas phase before Sr and Ba atoms are incorporated in the film, Ti atoms were deposited at the temperature where 70% of the IR absorbance at 250°C remained. These results indicate that the thermal decomposition in the gas phase has more significant effects on the deposition of Sr and Ba atoms than on that of Ti atoms and that the surface reactions of Ti(*t*-BuO)$_2$(DPM)$_2$ molecules are also important for the deposition of Ti atoms.

References

[1] T. Kawahara, S. Matsuno, M. Yamamuka, M. Tarutani, T. Sato, T. Horikawa, F. Uchikawa and K. Ono: Jpn. J. Appl. Phys. **38** (1999) 2205 and references therein.

[2] S. Sone, R. Akahane, K. Arita, H. Yabuta, S. Yamamichi, M. Yoshida and Y. Kato: Jpn. J. Appl. Phys. **38** (1999) 2200 and references therein.

[3] J. S. Lee, H. W. Song, B.-H. Jun, D. H. Kwack, B. G. Yu, Z.-T. Jiang and K. No: Thin Solid Films **301** (1997) 154.

[4] C. S. Kang, H.-J. Cho, C. S. Hwang, B. T. Lee, K.-H. Lee, H. Horii, W. D. Kim, S. I. Lee and M. Y. Lee: Jpn. J. Appl. Phys. **36** (1997) 6946.

[5] H.-K. Ryu, J. S. Heo, S.-I. Cho and S. H. Moon: J. Electrochem. Soc. **146** (1999) 1117.

[6] H.-K. Ryu, J. S. Heo, S.-I. Cho, C. Chung and S. H. Moon: J. Electrochem. Soc. **147** (2000) 1130.

[7] A. Yamamoto and S. Kambara: J. Am. Chem. Soc. **79** (1957) 4344.

[8] K. Nakamoto and A. E. Martell: J. Chem. Phys. **32** (1960) 588.

[9] K. Nakamoto, P. J. Mccarthy, A. Ruby and A. E. Martell: J. Am. Chem. Soc. **83** (1961) 1066.

[10] K. Nakamoto, P. J. Mccarthy and A. E. Martell: J. Am. Chem. Soc. **83** (1961) 1272.

[11] S. Pinchas, B. L. Silver and I. Laulicht: J. Chem. Phys. **46** (1967) 1506.

[12] D. C. Bradley and C. E. Holloway: J. Chem. Soc. A (1969) 282.

[13] T. Nakamura and K. Tachibana: Jpn. J. Appl. Phys. **40** (2001) 338.

[14] H. Harima, H. Ohnishi, K. Hanaoka, K. Tachibana and Y Goto: Jpn. J. Appl. Phys. **30** (1991) 1946.

[15] K. Hanaoka, H. Ohnishi and K. Tachibana: Jpn. J. Appl. Phys. **32** (1993) 4774.

[16] M. Yamamuka, T. Kawahara, M. Tarutani, T. Horikawa, T. Oomori and K Ono: J. Appl. Phys. **86** (1999) 1082.

Chapter 3

Development of microdischarge optical emission spectroscopy as a novel diagnostic tool for MOCVD

3.1 Introduction

As described in Chap. 2, we carried out the diagnosis in the metalorganic chemical vapor deposition (MOCVD) process of barium strontium titanate (Ba,Sr)TiO_3 [BST] films by using *in situ* infrared absorption spectroscopy [1]. Although *in situ* FT-IR measurements can provide much useful information on the reaction mechanisms in the MOCVD of BST films, it is insufficient to achieve the excellent step coverage and reproducibility of the film quality for the realization of the future generation of BST-DRAM. In order to understand the behavior of the CVD source molecules in more detail, diagnostic study of the MOCVD process of BST films must be carried out from another angle. There is no diagnostic technique applicable to

MOCVD processes with a few exceptions such as infrared absorption spectroscopy [1, 2, 3, 4, 5, 6, 7, 8, 9, 10, 11] and mass spectrometry [12, 13, 14, 15]. Therefore, we develop a novel diagnostic tool for MOCVD process, which is named microdischarge optical emission spectroscopy (μD-OES). Optical emission spectroscopy (OES) has been widely used to gain insight into plasma processings such as etching and film deposition. In this study, OES is applied to the diagnosis of liquid-source MOCVD of BST films. From the emission spectra of the small plasma excited at the μD-OES sensor head, it is possible to estimate the degree of thermal decomposition of the CVD source molecules. The results obtained by μD-OES measurements are discussed with referring to *in situ* FT-IR measurements. In order to study the effects of gas-phase reactions on the film deposition, the temperature dependence of the observed emission intensity is investigated relative to the film deposition rate and quality. For this procedure, it is important to know the correlation between the gas temperature and the substrate temperature. The gas temperature can be estimated from the rotational temperature of molecular nitrogen, the carrier gas of the CVD sources, using the OES sensor. The addition of an oxidizing gas such as O_2 or N_2O is empirically known to improve the crystallinity of the BST films [16, 17]. Thus, the oxidation of CVD source molecules in the gas phase is also investigated by observing the change in the emission spectra due to the addition of oxygen gas. The interaction between source molecules with different metal atoms is also studied by μD-OES. The spatial distribution of the source molecules, measured by moving the OES sensor head, is compared with the uniformity of the film thickness.

3.2 Experimental

Figure 3.1 shows a schematic diagram of the liquid-source CVD apparatus with the μD-OES system. The source supply system, CVD reactor, and source molecules are the same as described in Chap. 2. The μD-OES system is composed of an OES sensor head, a guiding optical fiber bundle and a spectrometer. The magnification of the OES sensor head is shown in the circle in Fig. 3.1. A half-inch-diameter stainless-steel tube and a stainless-steel needle were used as the cathode and anode, respectively. The hollow

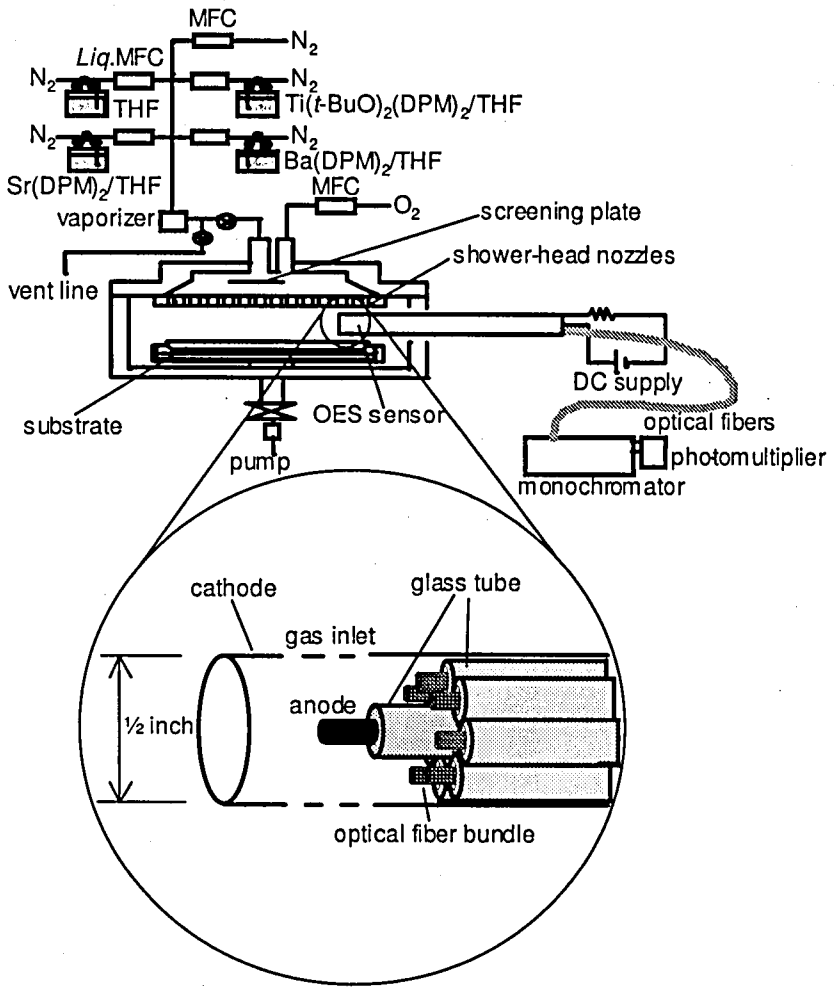

Figure 3.1: Schematic diagram of the liquid-source CVD apparatus with the microdischarge optical emission spectrometer. The magnification of the OES sensor head is shown in the circle.

cathode, having about 300 holes of 2.4 mm diameter for the source gases to pass through, was unified with an optical fiber bundle and kept at ground potential. The needle-type anode, which had a length of 10 mm and a diameter of 1 mm, was located at the center of the tubular cathode. Glass tubes were used as insulators which prevented the anode needle from contacting the tubular cathode. The microdischarge in the hollow cathode was excited by a DC power supply. In order to prevent decomposition reactions due to the discharge, we controlled the discharge voltage and current to be minimal. As a result, the discharge voltage and current were kept almost constant at 350 V and 4 mA, respectively. A series resistance of 30 kΩ was used to stabilize the discharge. The device was arranged in the form of a linearly movable probe which collected photoemission from a small plasma volume in the sensor head. The collected light rays were transported via an optical fiber bundle to a monochromator with a photomultiplier tube. The OES sensor probe was inserted horizontally between the showerhead plate and the substrate. The distance from the substrate to the anode needle was set to be 13.5 mm. The sensor head was moved along the diameter of the substrate wafer for measuring the uniformity of supplied sources.

3.3 Results and Discussion

3.3.1 Determination of gas temperature

The gas temperature is one of the crucial factors for determining the thermal decomposition of the CVD source molecules and generation of film precursors in the gas phase. We assumed the gas temperature T_g to be in equilibrium with the rotational temperature T_{rot} of molecular nitrogen, the carrier gas of the CVD sources, and determined its value from the unresolved rotational structure in the second positive system of the emission spectrum [18]. The wavelength of the rovibronic transition $Cv'J' - Bv''J''$ was calculated from

$$\lambda^{Cv'J'}_{Bv''J''} = \left\{ n_a \sum_{p=0}^{5} \sum_{q=0}^{2} Y^C_{pq} \left(v' + \frac{1}{2} \right)^2 [J'(J'+1)]^q - Y^B_{pq} \left(v'' + \frac{1}{2} \right)^p [J''(J''+1)]^q \right\}^{-1}, \quad (3.1)$$

where n_a is the refractive index of air and Y_{pq} is the expansion coefficient in the Dunham series. The intensity of the rovibronic transition $Cv'J' - Bv''J''$ is given by

$$F_{Bv''J''}^{Cv'J'} = D\frac{S_J}{T_{rot}} \exp[-hcB_v J'(J'+1)/kT_{rot}], \tag{3.2}$$

where D is a constant, S_J is the line strength for Hund's case (a) as given by Budó [19], and T_{rot} is the rotational temperature. Since the width of a rotational line is mainly determined by the slit width of the monochromator, a finite line shape

$$g(\Delta\lambda) = \frac{a - (2\Delta\lambda/W)^2}{a + (a-2)(2\Delta\lambda/W)^2}, \tag{3.3}$$

was assumed. The above function has the wings extended to $\pm(1/2)Wa^{1/2}$, where a is a parameter associated with the intrinsic linewidth of a rotational transition. W is given as the resolution of the monochromator.

The observed emission spectra of $1' - 3''$ transition in the second positive system of N_2 were analyzed by curve fitting with the calculated line shapes. Figure 3.2 shows the simulated spectrum along with the observed one when the substrate temperature T_{sub} and the pressure in the CVD reactor were set to be 400°C and 1 Torr, respectively. The best-fit parameters were found to be $W = 7.3$ Å, $a = 4$, and $T_{rot} = 255$°C. The agreement between the observed and calculated spectra is satisfactory. In Fig. 3.3, the relationship between T_g ($= T_{rot}$), which was measured at a height of 13.5 mm above the substrate, and T_{sub} is shown. An approximately linear relationship was obtained in this temperature range.

3.3.2 Measurement of the spatial distribution of CVD source materials

Since the OES sensor head is movable along the radial direction of the substrate wafer, it is possible to obtain the spatial distribution of the emission spectrum by μD-OES. Figure 3.4 shows the radial dependence of the 315.9 nm emission intensity of the carrier gas N_2 when a TiO_2 film was deposited by supplying only the Ti source. The flow rates of N_2, O_2 and liquid Ti(*t*-

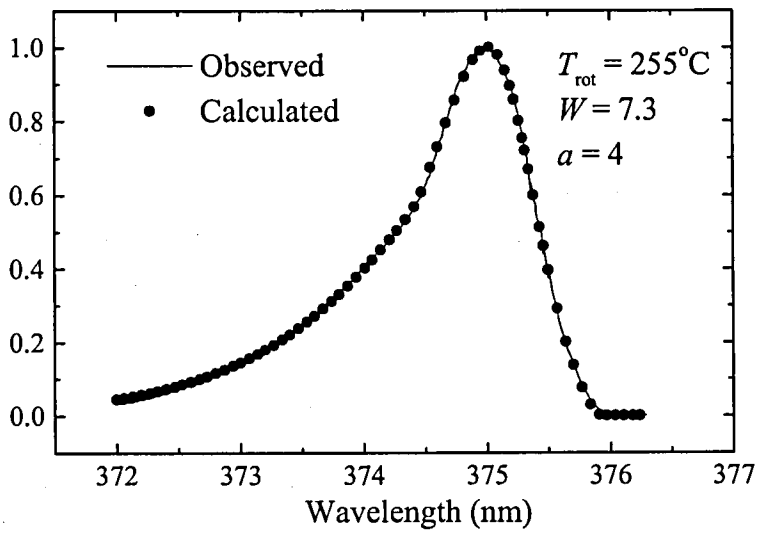

Figure 3.2: Observed and simulated emission spectra of the $1' - 3''$ transition in the second positive N_2 system ($C^3\Pi_u - B^3\Pi_g$). The solid line indicates the observed spectrum and the dotted line indicates the calculated one. When the substrate temperature T_{sub} was set to be 400°C, the gas rotational temperature T_{rot} was evaluated to be 255°C at 1 Torr.

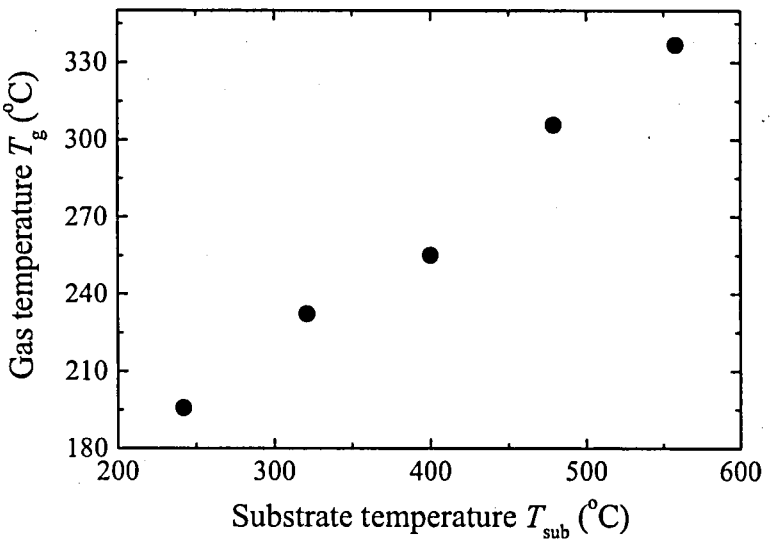

Figure 3.3: Gas temperature T_g (= T_{rot}) as a function of substrate temperature T_{sub}.

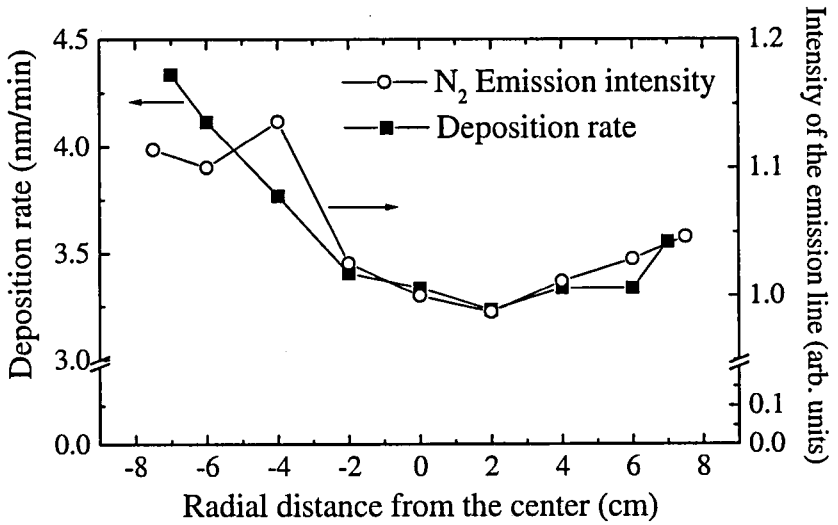

Figure 3.4: Spatial distribution of the N_2 emission intensity at 315.9 nm and the uniformity of the deposition rate.

$BuO)_2(DPM)_2$/THF were 200 sccm, 1000 sccm and 0.5 sccm, respectively. The observed emission was the $(1-0)$ band of the second positive N_2 system ($C^3\Pi_u - B^3\Pi_g$). The measured distribution of the N_2 emission intensity was compared with the deposition rate of the TiO_2 film (see Fig. 3.4). The deposition rate of the TiO_2 film was evaluated from the film thickness determined by spectroscopic ellipsometry. Since the uniformity of the substrate temperature was established in this CVD system, the deposition rate was dependent mainly on the incident flux of the film precursor derived from the CVD source molecule. The radial distribution of N_2 emission intensity has a good correlation with the deposition rate. This result indicates that the spatial distribution of the CVD source materials can be easily obtained from that of the carrier gas N_2. Thus, the thickness uniformity of the deposited films can be estimated by monitoring the spatial distribution of the emission intensity of the carrier gas. Better uniformity of the film thickness can be obtained by modifying the screening plate, based on the μD-OES data.

3.3.3 Thermal decomposition of the CVD source molecules

The optical emission spectra were observed under actual CVD experimental conditions using the μD-OES system. The pressure in the reactor was maintained at 1 Torr. Figure 3.5 shows the typical spectra at 320-460 nm observed with supplying $Sr(DPM)_2$ and $Ba(DPM)_2$ molecules. Several emission lines derived from CVD sources were observed with many transitions due to the N_2 carrier gas. We observed the emissions of SrII 407.7 nm ($5p^2P_{3/2} \longrightarrow 5s^2S_{1/2}$) line and BaII 455.4 nm ($6p^2P_{3/2} \longrightarrow 6s^2S_{1/2}$) line. When Ti($t$-$BuO)_2(DPM)_2$ molecules were supplied into the reactor, the emission of TiII 338.4 nm ($a^4F_{3/2} \longrightarrow z^4G^o_{5/2}$) was observed (see Fig. 3.6). Figure 3.7 shows the temperature dependence of the emission intensities of SrII 407.7 nm and TiII 338.4 nm. The temperature indicated on the horizontal axis is the gas temperature T_g determined by the method described in the preceding section. The temperature dependence of the IR absorbance of both the Sr and Ti source molecules at 1503 cm^{-1}, which is assigned to the stretching mode of the C-O and C-C bonds in the DPM chelate ring [1], is also shown in

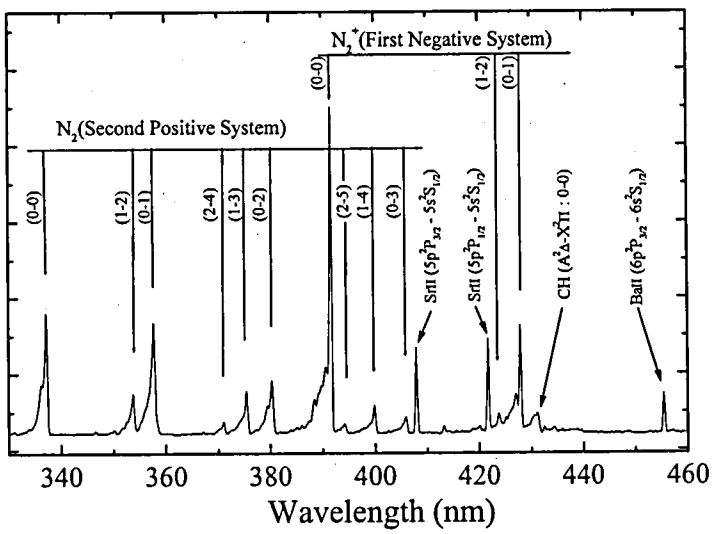

Figure 3.5: Typical emission spectra at 320-460 nm observed by the microdischarge optical emission spectrometer.

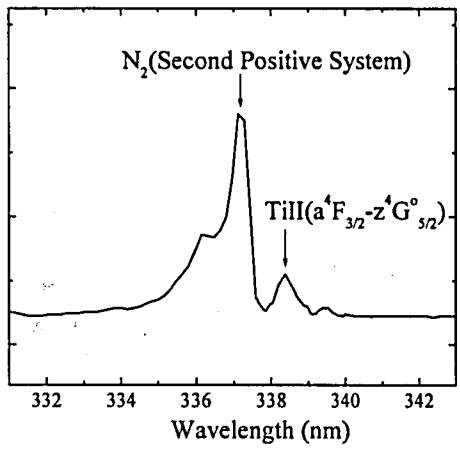

Figure 3.6: Emission spectra of Ti ion (338.4 nm: $a^4F_{3/2} \longrightarrow z^4G^o_{5/2}$).

Fig. 3.7. This measurement of IR absorbance was also carried out at the reactor pressure of 1 Torr. The IR absorbance at 1503 cm^{-1} indicates the degree of thermal decomposition of the chelate ring in the source molecules. The temperature dependence of the emission intensity of the Ti ion was well correlated with the IR absorbance of the Ti source molecules, and the SrII emission appeared when the thermal decomposition of $Sr(DPM)_2$ was sufficient. This result means that the μD-OES can provide information about the degree of thermal decomposition of the source molecules. When the gas temperature was below 265°C, no emission of Sr ions was detected while emission of Ti ions was observed, although both the parent molecules, $Sr(DPM)_2$ and $Ti(t\text{-}BuO)_2(DPM)_2$, remained undecomposed according to the IR spectra. It has been reported that $Sr(DPM)_2$ molecules exist as polymerized forms [15], and that the O atom of THF forms an additional coordinate bond with the central metal atom of DPM compounds [20, 21]. Thus, the Sr atoms of the molecules are not easily exposed to electron impacts due to the microdischarge. On the other hand, similar phenomena have not been reported for Ti complexes such as $Ti(t\text{-}BuO)_2(DPM)_2$. The different behavior of the emissions between SrII and TiII can be considered to be caused by the difference

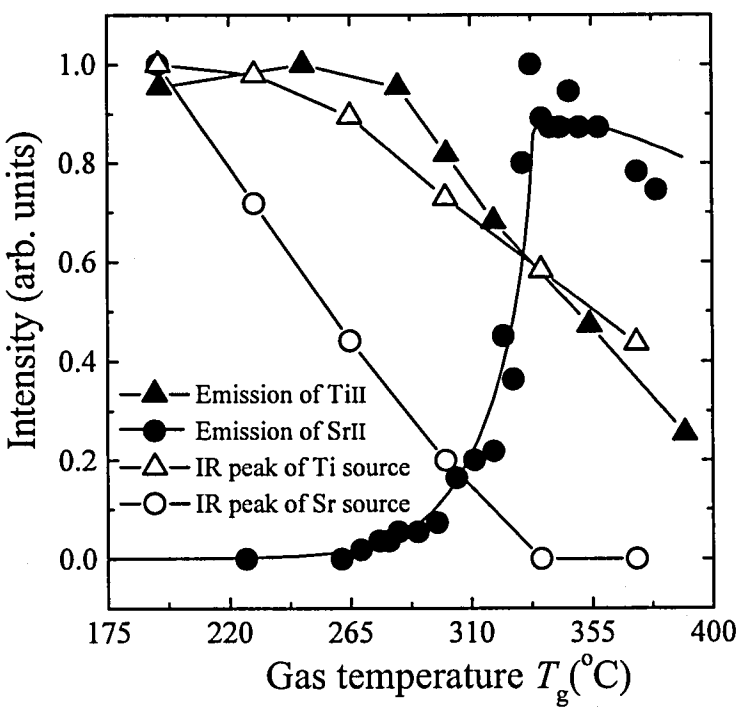

Figure 3.7: Temperature dependence of the emission intensities of SrII and TiII. The IR peak intensity at 1503 cm^{-1} is also shown. Closed triangles and circles denote the emission intensities of TiII and SrII, while open triangles and circles represent the IR peak intensities of Ti and Sr sources, respectively.

in the environment around the metal atoms at low gas temperatures of below 265°C.

As the gas temperature was increased, the emission of the Sr ion increased through the thermal decomposition of $Sr(DPM)_2$ molecules. In contrast to $Sr(DPM)_2$, the emission of Ti ions decreased when $Ti(t\text{-}BuO)_2(DPM)_2$ molecules decomposed, which indicates that the pyrolysates containing the Ti element do not decompose into a Ti atom. As described in Chap. 2, we measured the temperature dependence of IR peak intensities of Sr and Ti source molecules. We found that the Sr-O bond is easily cleaved compared to the other bonds in the DPM chelate rings, by IR absorption study. Since $Sr(DPM)_2$ molecules decompose thermally with cleavage of the Sr-O bond, Sr atoms of $Sr(DPM)_2$ are easily exposed to electron impacts through thermal decomposition. Thus, after thermal decomposition proceeds, emission of the Sr ion is increased. Its intensity increased as T_g increased from 265°C to 330°C, and finally saturated at $T_g \geq 330$°C. This saturation of emission intensity suggests that almost all the supplied source molecules exist as decomposed species in the gas phase.

On the other hand, the IR absorbance at 623 cm^{-1} of $Ti(t\text{-}BuO)_2(DPM)_2$, which is assigned to the stretching mode of the Ti-O bond, decreased at a higher temperature than the IR absorbance at 1503 cm^{-1}, which is assigned to the C-O and C-C bonds in the chelate ring (see Fig. 2.5 in Chap. 2). This result means that the Ti-O bond is difficult to cleave compared to the C-O and C-C bonds in the DPM chelate rings. In other words, the Ti-O bonds remain stable at the temperature where the C-O and C-C bonds are cleaved through the thermal decomposition of $Ti(t\text{-}BuO)_2(DPM)_2$. Thus, the difference in the temperature dependence of the emissions may be caused by the difference in the thermal decomposition schemes between $Sr(DPM)_2$ and $Ti(t\text{-}BuO)_2(DPM)_2$ molecules.

Although we attempted to investigate reactions of $Sr(DPM)_2$ molecules at the typical deposition temperature by *in situ* IR absorption spectroscopy, we could not observe any IR peak due to $Sr(DPM)_2$ because $Sr(DPM)_2$ molecules were completely decomposed at a comparatively low gas temperature (below 320°C). Moreover, we could not observe any peak due to pyrolysates generated from $Sr(DPM)_2$. On the other hand, the μD-OES allows us to observe

the emission of Sr ions at the typical deposition temperature where the IR absorption spectroscopy was not available for the diagnosis of Sr precursors. The complementary employment of the μD-OES and *in situ* IR absorption spectroscopy can provide valuable information about gas-phase reactions in MOCVD processings. The temperature dependence of the emission intensity of BaII 455.4 nm ($6p^2P_{3/2} \longrightarrow 6s^2S_{1/2}$) line was also measured. The BaII line behaved similarly to the SrII line, which means that the chemical characteristics of $Ba(DPM)_2$ molecules are almost the same as $Sr(DPM)_2$ molecules.

3.3.4 Effects of gas-phase reaction detected by μD-OES on the film deposition

Figure 3.8 shows the correlation between the emission intensity of the SrII line at 407.7 nm and the deposition rate of films deposited when only Sr source molecules were supplied. It should be noted that the temperature denoted on the horizontal axis in Fig. 3.8 is not the gas temperature T_g but the substrate temperature T_{sub}. The deposition rate shows a behavior similar to the emission intensity. However, the film grows rapidly at $T_{sub} \geq 560°C$, while a marked increase of SrII intensity occurs earlier at $T_{sub} \geq 520°C$. As discussed in the above section, the SrII emission appeared due to the thermal decomposition of $Sr(DPM)_2$ and reflects the generation of film precursors in the gas phase. However, the film growth proceeds not only by the generation of film precursors in the gas phase but also by the subsequent incorporation of the film precursors into the film surface. Therefore, the experimental finding shown in Fig. 3.8 indicates that the incorporation reaction of the film precursors, generated rapidly in the gas phase at $T_{sub} \geq 520°C$, is activated on the surface at $T_{sub} \geq 560°C$. In this temperature range ($560°C \geq T_{sub} \geq 520°C$), the rate-determining step of the film deposition is suggested to be the surface reactions for the incorporation of the film precursors into the film.

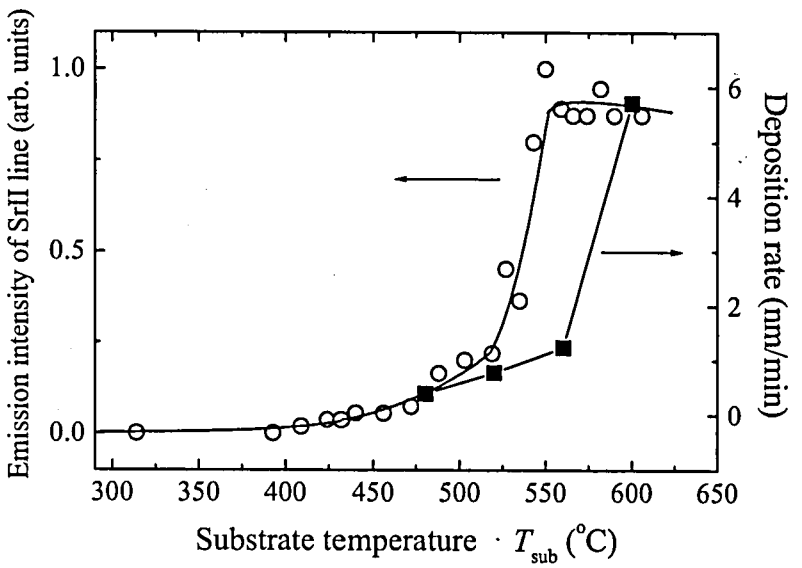

Figure 3.8: Correlation between the emission intensity of SrII 407.7 nm and the deposition rate of films deposited when only Sr source molecules were supplied.

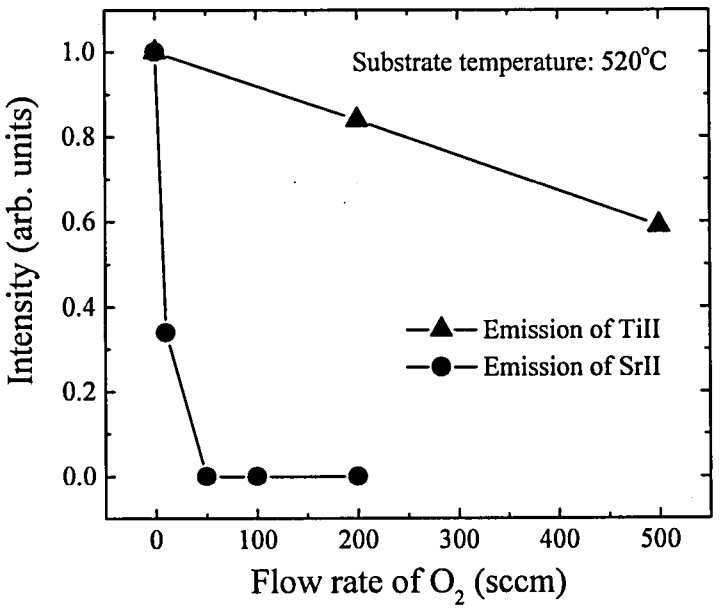

Figure 3.9: Change in the emission intensities of SrII and TiII on adding oxidation gas.

3.3.5 Oxidation of the CVD source molecules

The dielectric constant of the (Ba,Sr)TiO_3 film was reported to increase with an increase in its crystallinity and grain size [22]. In the CVD processings of the (Ba,Sr)TiO_3 films, the addition of an oxidation gas such as O_2 and N_2O promotes the crystallization of the deposited films [16, 17]. We investigated the oxidation process of CVD source molecules using μD-OES at a substrate temperature of 520°C. When the substrate temperature was 520°C, the gas temperature was 320°C. This temperature is in a typical range for the deposition of BST films. In Fig. 3.9, the emission intensities of SrII and TiII are shown as a function of the flow rate of O_2 gas. The SrII emission intensity decreased rapidly due to the addition of O_2. This quenching of the SrII emission indicates that the oxidation of Sr-containing species proceeds

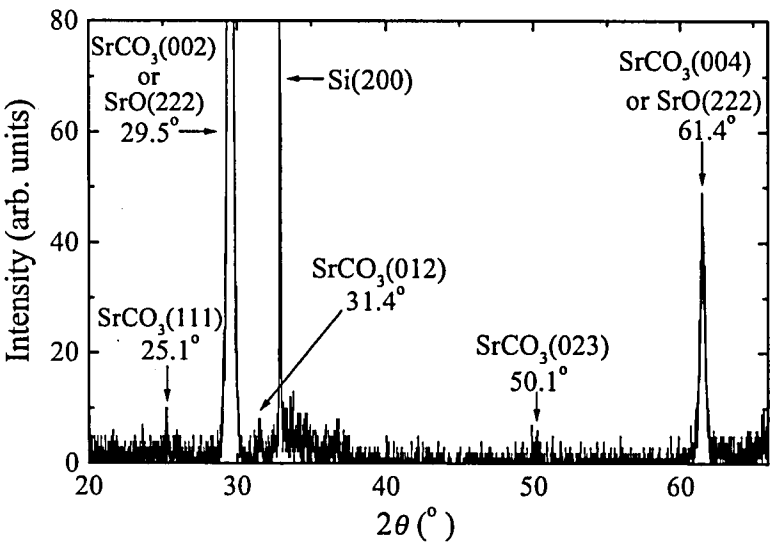

Figure 3.10: XRD pattern of the thin film deposited by supplying $Sr(DPM)_2$/THF with O_2.

in the gas phase. On the other hand, the TiII emission did not decrease rapidly compared to that of SrII. This result means that in a typical temperature range for the deposition of BST films, Sr-containing species are much more reactive to O_2 gas than Ti-containing species. In this temperature range, $Sr(DPM)_2$ molecules are decomposed almost completely, while only one-third of $Ti(t\text{-}BuO)_2(DPM)_2$ molecules are decomposed, according to the *in situ* IR absorption measurements (see Fig. 3.7). This stability of the $Ti(t\text{-}BuO)_2(DPM)_2$ molecule, particularly the Ti-O bonds, against thermal decomposition may be responsible for the lower reactivity of Ti precursors to O_2 gas.

The crystalline characteristics of the deposited films were analyzed by X-ray diffractometry (XRD) to study the correlation between the gas-phase oxidation and the crystalline growth. Figure 3.10 shows the typical XRD pattern of the film deposited by supplying $Sr(DPM)_2$/THF with O_2. The peaks

due to the crystalline SrO and/or $SrCO_3$ were observed. According to an X-ray photoelectron spectroscopy (XPS) measurement, the atomic composition of the film deposited with O_2 was determined to be Sr:O:C = 3:5:1, suggesting that this film was composed of a mixture of SrO and $SrCO_3$ ($SrO:SrCO_3$ = 2:1). However, no XRD signal was observed in the films deposited without supplying O_2. The atomic composition of the films deposited without O_2 was evaluated to be Sr:O:C = 2:1:2, indicating the lack of oxygen required for the growth of SrO crystal and the incorporation of a significant amount of carbon impurity into the film. The oxidation of the film precursor in the gas phase is important for obtaining high crystallinity and low carbon contamination of the deposited films.

3.3.6 Interaction between source molecules with different metal atoms in gas phase

During the deposition of BST films, an interaction between source molecules with the different metal atoms is supposed to occur in the gas phase. For example, a reaction between $Ca(DPM)_2$ and $Sr(DPM)_2$ was reported to form a heteronuclear polymer containing both metal atoms [15]. In this work, we attempted to investigate the gas phase interaction between $Sr(DPM)_2$ and $Ti(t\text{-}BuO)_2(DPM)_2$ by using the μD-OES. Figure 3.11(a) shows the change in the SrII emission intensity with the addition of $Ti(t\text{-}BuO)_2(DPM)_2$ at gas temperature of 333°C and Fig. 3.11(b) shows the change in the TiII emission upon the addition of $Sr(DPM)_2$ at gas temperature of 250°C. When the addition of the other source was increased, the emission intensities of the SrII and TiII were decreased. Since the ratio of the supply rate of $Sr(DPM)_2$ to the sum of all the liquid sources was kept constant in Fig. 3.11(a) and that of $Ti(t\text{-}BuO)_2(DPM)_2$ was also kept constant in Fig. 3.11(b), the observed emission decrease was not caused by the dilution. This result suggests the interaction between $Ti(t\text{-}BuO)_2(DPM)_2$ and $Sr(DPM)_2$ occurs in the gas phase.

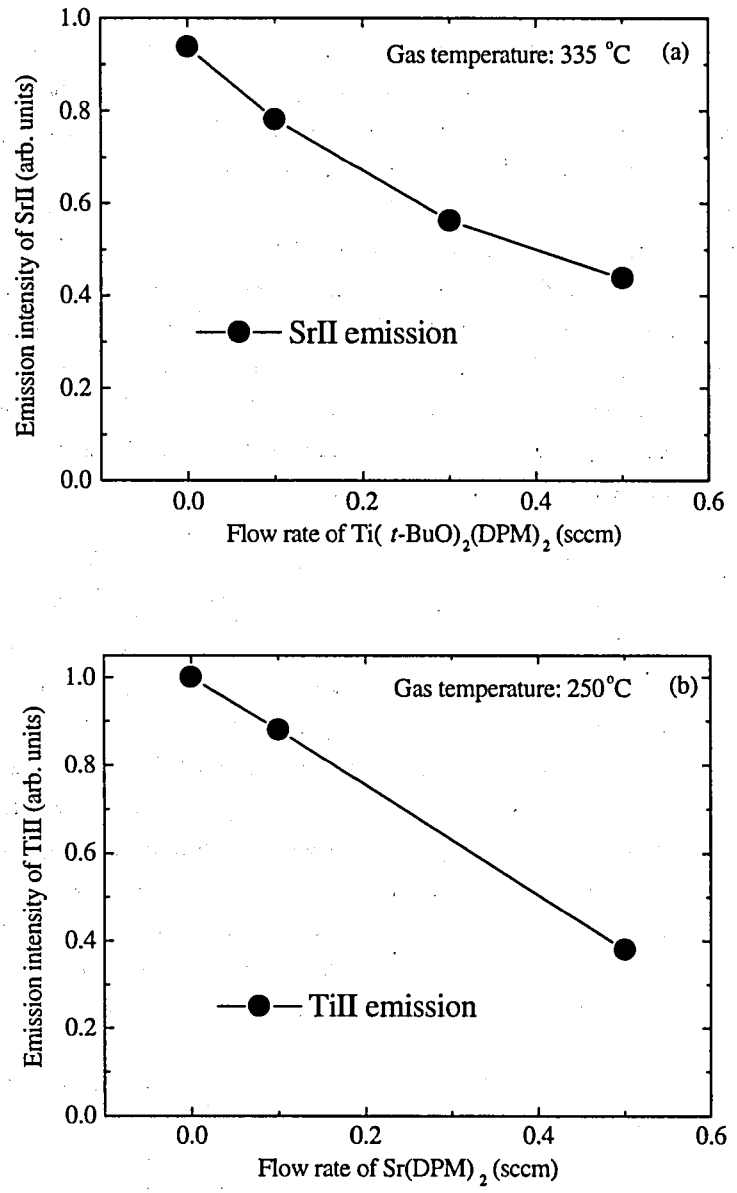

Figure 3.11: Changes in the emission intensities upon the addition of other sources: (a) change in the SrII emission and (b) change in the TiII emission.

3.4 Conclusions

We developed an OES sensor system using a microdischarge plasma for analyzing the chemical reactions in MOCVD processings and demonstrated its usefulness in applications to the liquid-source MOCVD of (Ba,Sr)TiO_3 films. The dissociation of the metal-oxygen coordination bond (M-O bond) is the key step for the generation of the film precursor from the CVD source molecule. The μD-OES technique provides information about the M-O bond, which other spectroscopic methods are difficult to obtain. The thermal decomposition and oxidation of $Sr(DPM)_2$ and Ti(*t*-BuO)$_2$(DPM)$_2$ molecules were studied by μD-OES. In order to understand the gas phase reactions in greater detail, we compared the data obtained by μD-OES with those of *in situ* IR absorption measurements. When the gas temperature was increased, the SrII emission behaved inversely to the temperature dependence of the IR absorbance of $Sr(DPM)_2$. On the other hand, the temperature dependence of the TiII emission intensity showed a direct correlation with that of the IR absorbance of Ti(*t*-BuO)$_2$(DPM)$_2$. This suggests that the Ti source behaves differently from the Sr source at both low and high temperatures. At low gas temperatures (below 320°C) only the IR absorbance of $Sr(DPM)_2$ was observed, while at high gas temperatures (above 320°C) no IR absorbance was observed due to the Sr-containing species, but the emission of Sr ions from the microdischarge could be observed. This result means that by using μD-OES and IR absorption spectroscopy complementarily, we can investigate the gas-phase reactions of the source molecules. That is, at low gas temperatures the IR absorbance of $Sr(DPM)_2$ is a good monitor of the decomposition of Sr source molecules, and at high gas temperatures above 330°C (the typical temperature for BST deposition), the emission of Sr ions detected by μD-OES is a good monitor of the production of Sr precursors. We also observed the changes in the TiII and SrII emissions with the addition of other source materials, which suggests the interaction between $Sr(DPM)_2$ and Ti(*t*-BuO)$_2$(DPM)$_2$ molecules.

At the typical deposition temperature, an oxidation gas such as O_2 has high reactivity to the Sr precursor in the gas phase, although this is not the case with the Ti precursor. This distinction may be caused by the difference

in the strength of M-O bonds; the Sr-O bond is easy to cleave, while the Ti-O bond is difficult to cleave [1]. The oxidation of the film precursors in the gas phase is considered to have considerable influence on the crystallinity and carbon contamination of the deposited films. The crystallinity and carbon impurity concentration are the most important factors for determining the dielectric constant and leakage current of the dielectric capacitor film, respectively. To understand the mechanisms of the MOCVD process and optimize the deposition conditions, the accumulation of experimental data, as determined in this study, is important and useful.

References

[1] S. Momose, T. Nakamura and K. Tachibana: Jpn. J. Appl. Phys. **39** (2000) 5384.

[2] M. L. Hitchman, S. H. Shamlian, G. G. Condorelli and F. Chabert-Rocabois: J. Alloys Compd. **251** (1997) 297.

[3] H. Harima, H. Ohnishi, K. Hanaoka, K. Tachibana, M. Kobayashi and S. Hoshinouchi: Jpn. J. Appl. Phys. **29** (1990) 1932.

[4] H. Harima, H. Ohnishi, K. Hanaoka, K. Tachibana and Y Goto: Jpn. J. Appl. Phys. **30** (1991) 1946.

[5] K. Hanaoka, H. Ohnishi and K. Tachibana: Physica C **190** (1991) 145.

[6] B. Zheng, G. Braeckelmann, K. Kujawski, I. Lou, S. Lane and A. E. Kaloyeros: J. Electrochem. Soc. **142** (1995) 3896.

[7] K. Hanaoka, H. Ohnishi and K. Tachibana: Jpn. J. Appl. Phys. **32** (1993) 4774.

[8] K. Hanaoka, H. Ohnishi and K. Tachibana: Thin Solid Films **262** (1995) 209.

[9] K. Hanaoka, H. Ohnishi and K. Tachibana: Jpn. J. Appl. Phys. **34** (1995) 2430.

[10] H.-K. Ryu, J. S. Heo, S.-I. Cho and S. H. Moon: J. Electrochem. Soc. **146** (1999) 1117.

[11] H.-K. Ryu, J. S. Heo, S.-I. Cho, C. Chung and S. H. Moon: J. Electrochem. Soc. **147** (2000) 1130.

[12] M. Yamamuka, T. Kawahara, T. Horikawa and K. Ono: Jpn. J. Appl. Phys. **36** (1997) 2555.

[13] A. E. Turgambaeva, V. V. Krisyuk, A. F. Bykov and I. K. Igumenov: J. Phys. IV **9** (1999) 65.

[14] J. S. Lee, H. W. Song, K. S. Kim, B. G. Yu, Y. H. Jeong, Z.-T. Jiang and K. No: J. Vac. Sci. & Technol. A **15** (1997) 72.

[15] J. E. Schwarberg, R. E. Sievers and R. W. Moshier: Anal. Chem. **42** (1970) 1828.

[16] M. Yamamuka, T. Kawahara, A. Yuuki and K. Ono: Jpn. J. Appl. Phys. **35** (1996) 2530.

[17] C. S. Hwang, C. S. Kang, H.-J. Cho, S. O. Park, B. T. Lee, J. W. Kim, H. Horii, S. I. Lee and M. Y. Lee: Integrat. Ferroelectr. **12** (1996) 199.

[18] D. M. Phillips: J. Phys. D **8** (1975) 507.

[19] A. Budó: Z. Phys. **105** (1937) 579.

[20] S. Matsuno, F. Uchikawa and K. Yoshizaki: Jpn. J. Appl. Phys. **29** (1990) L947.

[21] W. Paw, T. H. Baum, K.-C. Lam and A. L. Rheingold: Inorg. Chem. **39** (2000) 2011.

[22] T. Horikawa, N. Mikami, T. Makita, J. Tanimura, M. Kataoka, K. Sato and M. Nunoshita: Jpn. J. Appl. Phys. **32** (1993) 4126.

Chapter 4

Diagnosis of oxidation reactions in MOCVD of (Ba,Sr)TiO_3 films

4.1 Introduction

In Chaps. 2 and 3, we have studied the thermal decomposition of source molecules during metalorganic chemical vapor deposition (MOCVD) of barium strontium titanate (Ba,Sr)TiO_3 [BST] films using spectroscopic techniques such as a microdischarge optical emission spectroscopy (μD-OES) and *in situ* Fourier transform infrared (FT-IR) spectroscopy [1, 2, 3]. It has been reported that the properties of BST films are strongly affected by the deposition conditions, such as the deposition temperature, the pressure in the reactor, and the kind of oxidation gas [4, 5, 6]. In particular, it is known that oxidation gas plays an important role in the improvement of the crystallinity and the dielectric characteristics of deposited BST films [4, 7]; nevertheless, the oxidation reactions remain to be clarified. In this study, we conduct *in situ* FT-IR absorption measurements to investigate the oxidation

reactions of the source molecules. As oxidation gas, O_2 and N_2O gases are used. Although several recent studies have reported the characteristics of films deposited in O_2 and N_2O ambients, some of them showed contradicting experimental results: Hwang *et al.* reported that the Ti/Sr atomic ratio in deposited strontium titanate $SrTiO_3$(STO) films was decreased when oxidation gas was changed from O_2 to N_2O [7], while Joo *et al.* reported that the Ti/(Ba+Sr) ratio in BST films was increased under the same conditions [8]. In general, Ti atoms are known to be more difficult to incorporate into BST films at low substrate temperature than Ba and Sr atoms [5]. An appropriate choice of oxidation gas is expected to increase the Ti/(Ba+Sr) atomic ratio in BST films deposited at low temperature. In this chapter, we investigate the oxidation mechanism of the source molecules during MOCVD of BST films, focusing on the difference between O_2 and N_2O gases. We correlate the results of *in situ* FT-IR measurements with the characteristics of the oxide films deposited in O_2 and N_2O ambients, and determine which oxidation gas is more suitable for the fabrication of BST capacitors.

4.2 Experimental

As the preparation method of BST films, the liquid-source MOCVD technique was employed. The liquid-source MOCVD apparatus and the setup of the FT-IR spectrometer were the same as described in Chap. 2 (see Fig. 2.1). CVD source materials were $Ba(DPM)_2$, $Sr(DPM)_2$, and $Ti(t\text{-}BuO)_2(DPM)_2$. The source materials vaporized in the vaporizer were transported into a hot-wall CVD reactor and subsequently mixed with the oxidation gas, O_2 or N_2O. The pressure in the reactor was maintained at 10 Torr, and the substrate temperature was varied from 240°C to 640°C. Strontium oxide and BST thin films were deposited on 6-inch-diameter Si(200) substrates. The atomic composition of the deposited films was evaluated by X-ray photoelectron spectroscopy (XPS) after etching of the films' surfaces.

Gas-phase oxidation reactions of the source molecules in O_2 and N_2O ambients were studied by *in situ* FT-IR spectroscopy. The IR absorption spectra at a wavenumber between 400 cm^{-1} and 4000 cm^{-1} were observed under actual CVD conditions. The IR beam covered almost the entire region

between the shower-head plate and the substrate. Details of the FT-IR measurements are described in Chap. 2.

4.3 Results and Discussion

4.3.1 Diagnosis of gas-phase oxidation reactions of Ti(*t*-BuO)$_2$(DPM)$_2$

We measured *in situ* IR absorption spectra of Ti(*t*-BuO)$_2$(DPM)$_2$ when oxidation gases, O_2 and N_2O, were added. In order to correctly evaluate the effect of the addition of oxidation gases, FT-IR measurement was also carried out when N_2 was added as the diluent gas at the same flow rate as that of the oxidation gas, in order to keep the residence time of the source molecules constant in the CVD reactor. No significant change in the spectral feature was observed with the addition of oxidation gas. A typical IR spectrum of Ti(*t*-BuO)$_2$(DPM)$_2$ in O_2 ambient is shown in Fig. 4.1. This spectrum was measured at the substrate temperature T_s of 240°C, which was the same temperature as the vaporizer. The vibrational spectral peaks were assigned on the basis of *ab initio* quantum chemical calculations [9]. Figure 4.2(a) shows the T_s dependence of the intensities of the IR spectral peaks at 577 and 623 cm^{-1}, which have been assigned to Ti-O stretching modes in *t*-butoxy groups and DPM chelate rings, respectively. The intensities are normalized to the values at 240°C. With the addition of oxidation gases, the intensities of the two IR peaks decreased at lower temperature. This decrease in the IR peak intensity is more drastic in O_2 ambient than in N_2O ambient. In the oxidation gas ambients, the IR absorption peak of the Ti-O bonds in the DPM chelate rings shows a behavior similar to that of the Ti-O bonds in the *t*-butoxy groups. Figure 4.2(b) shows the T_s dependence of the intensities of the IR absorption peaks at 733 and 888 cm^{-1}, which have been assigned to an in-plane ring deformation mode with C-C(CH$_3$)$_3$ stretching and an out-of-plane C-C-H bending mode of *i*-butene, respectively. *i*-Butene is one of the byproducts of the thermal decomposition of the parent molecule, *i.e.*, the dissociation of the *t*-butoxy group from the chelate ring. Similar to the Ti-O stretching modes, the addition of O_2 had a greater influence on the IR

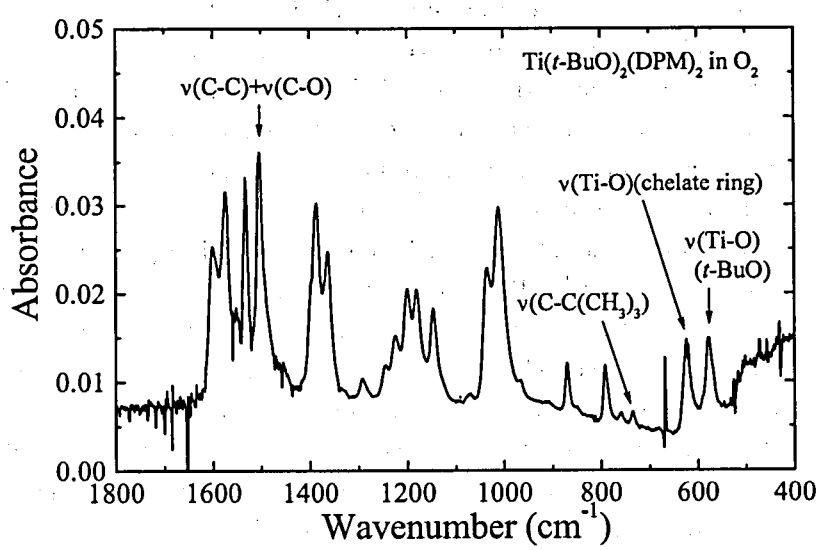

Figure 4.1: IR spectrum of Ti(t-BuO)$_2$(DPM)$_2$ observed in O_2 ambient at a substrate temperature of 240°C. The vibration mode is as follows: ν: stretching mode, π: out-of-plane bending mode.

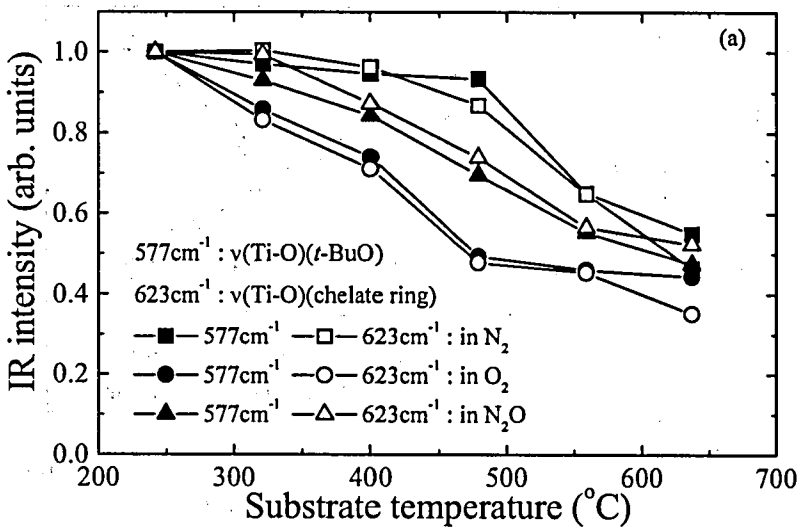

Figure 4.2: Substrate temperature dependence of the normalized IR absorption peak intensities of $Ti(t\text{-}BuO)_2(DPM)_2$ in N_2, O_2 and N_2O ambients: (a) 577 and 623 cm^{-1} peaks, (b) 733 and 888 cm^{-1} peaks and (c) 1503 cm^{-1} peak.

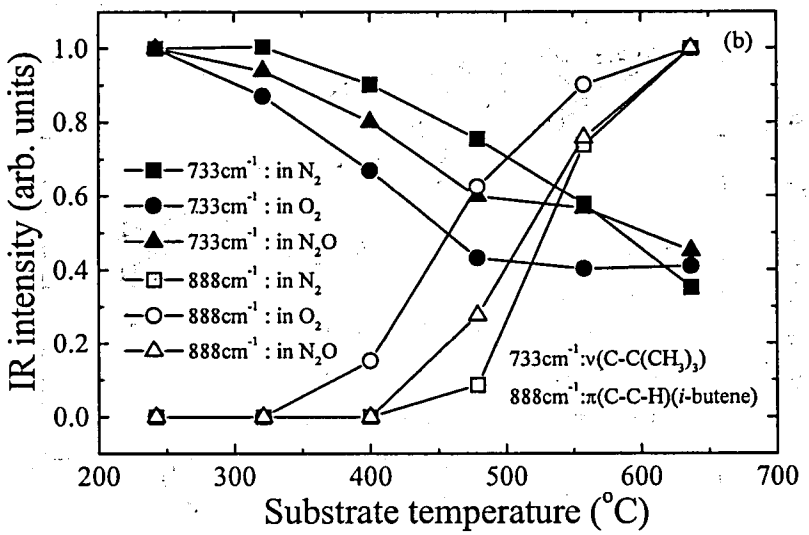

Figure 4.2: Substrate temperature dependence of the normalized IR absorption peak intensities of Ti(*t*-BuO)$_2$(DPM)$_2$ in N_2, O_2 and N_2O ambients: (a) 577 and 623 cm^{-1} peaks, (b) 733 and 888 cm^{-1} peaks and (c) 1503 cm^{-1} peak.

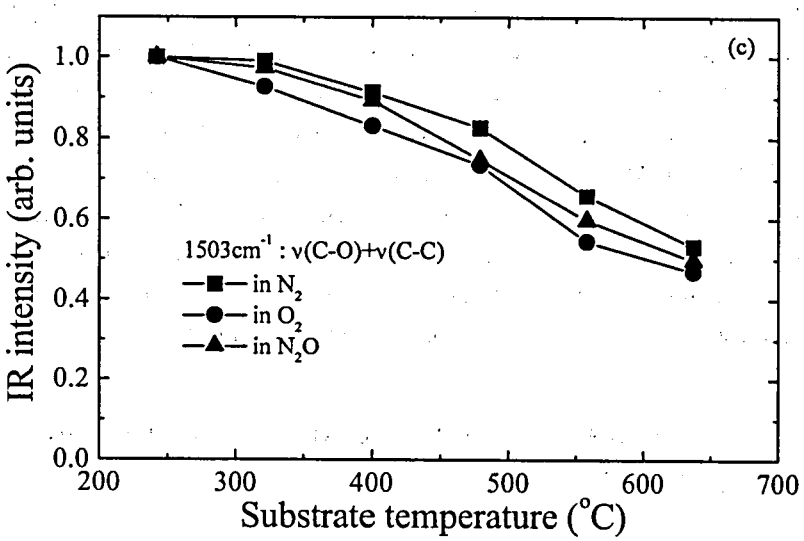

Figure 4.2: Substrate temperature dependence of the normalized IR absorption peak intensities of Ti(*t*-BuO)$_2$(DPM)$_2$ in N_2, O_2 and N_2O ambients: (a) 577 and 623 cm^{-1} peaks, (b) 733 and 888 cm^{-1} peaks and (c) 1503 cm^{-1} peak.

absorption of the C-C$(CH_3)_3$ bonds than that of N_2O. The substrate temperature dependence of the IR absorption peak at 1503 cm^{-1} is shown in Fig. 4.2(c), which is assigned to C-C and C-O stretching modes in the chelate rings. The addition of oxidation gases resulted in only a slight difference in the IR absorption of these bonds in the chelate rings. These findings in Figs. 4.2(a)-4.2(c) indicate that the oxidation gas does not attack evenly all the bonds of a source molecule; it is more reactive with such bonds as Ti-O and C-C$(CH_3)_3$. Figure 4.3 shows the electron density distribution calculated based on the density functional theory (DFT) for Ti$(MeO)_2(ACAC)_2$, which is a prototype of the source molecule, in which all the *t*-butyl groups of Ti(*t*-BuO)$_2$(DPM)$_2$ are replaced by methyl groups [9]. As shown in Fig. 4.3, the electron density is low in the vicinity of Ti-O and C-CH_3 bonds of Ti$(MeO)_2(ACAC)_2$. This theoretical result indicates that the oxidation gases attack selectively the low-electron-density sites in the source molecule. Considering that the oxidation gases behave as nucleophilic reagents, the above experimental results obtained by *in situ* FT-IR measurements can be explained well by *ab initio* quantum chemical calculation.

4.3.2 Diagnosis of gas-phase oxidation reactions of Sr(DPM)$_2$

The *in situ* IR absorption spectra of Sr(DPM)$_2$ were also measured when oxidation gases, O_2 and N_2O, were added. No significant change in spectral feature due to the addition of an oxidation gas was observed, as in the case of Ti(*t*-BuO)$_2$(DPM)$_2$. A typical IR spectrum of Sr(DPM)$_2$ in N_2O ambient is shown in Fig. 4.4, which was measured at T_s = 240 °C. Infrared band identification was carried out on the basis of density functional calculations [9]. Figure 4.5 shows the T_s dependence of the intensities of the IR spectral peaks at (a) 733 cm^{-1}, (b) 865 cm^{-1}, and (c) 1590 cm^{-1}. The assignments of these three spectral peaks are as follows: peak (a) corresponds to the out-of-plane ring deformation that mainly comprises the C-C stretching mode, peak (b) corresponds to the C-C$(CH_3)_3$ stretching mode with in-plane ring deformation, and peak (c) corresponds to the C-C and C-O stretching modes in the chelate rings. No significant change in the T_s dependence of the inten-

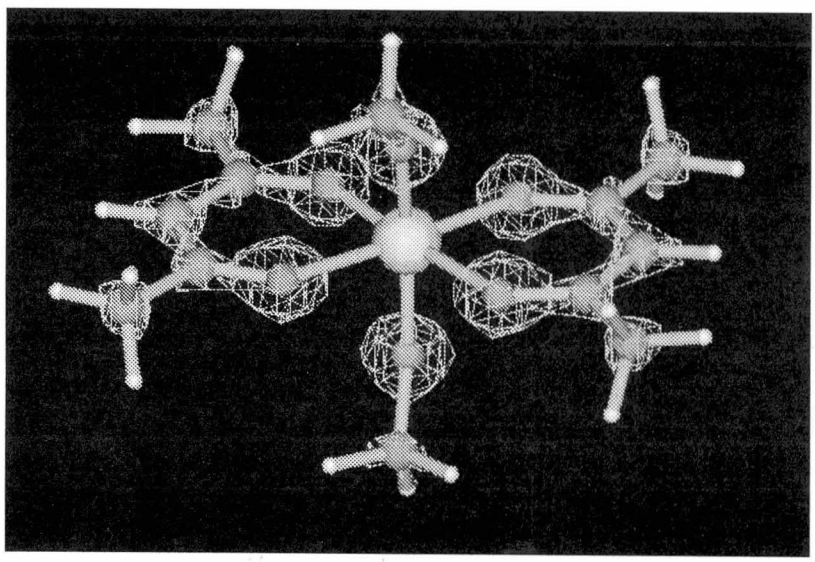

Figure 4.3: Electron density distribution in $Ti(MeO)_2(ACAC)_2$ calculated based on the density functional theory.

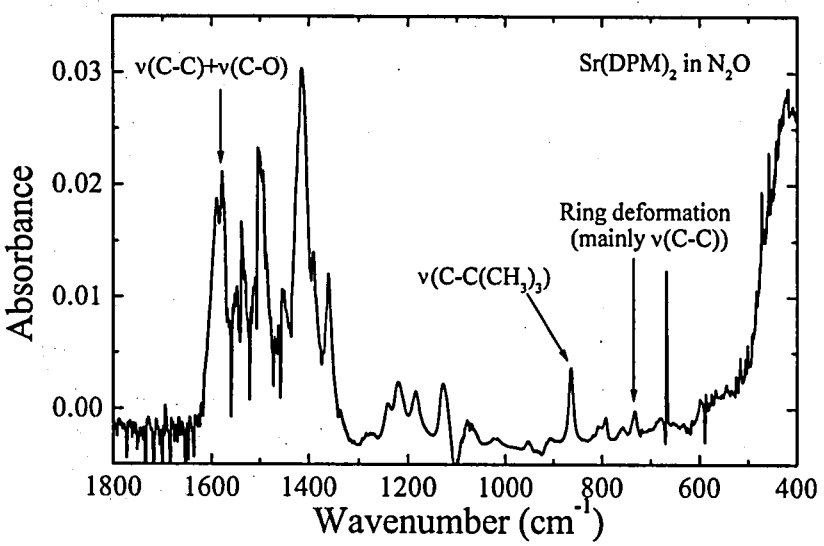

Figure 4.4: IR spectra of $Sr(DPM)_2$ in N_2O ambient at a substrate temperature of 240°C.

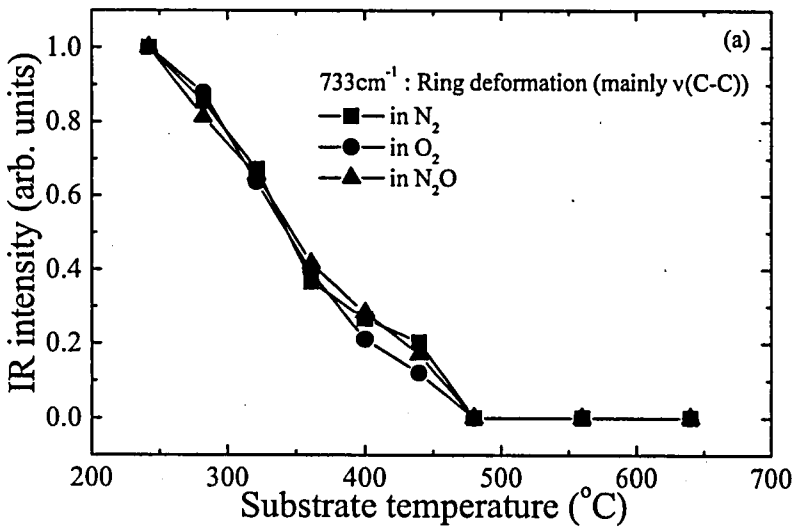

Figure 4.5: Substrate temperature dependence of the normalized IR absorption peak intensities of $Sr(DPM)_2$ in N_2, O_2 and N_2O ambients: (a) 733 cm^{-1} peak, (b) 865 cm^{-1} peak and (c) 1590 cm^{-1} peak.

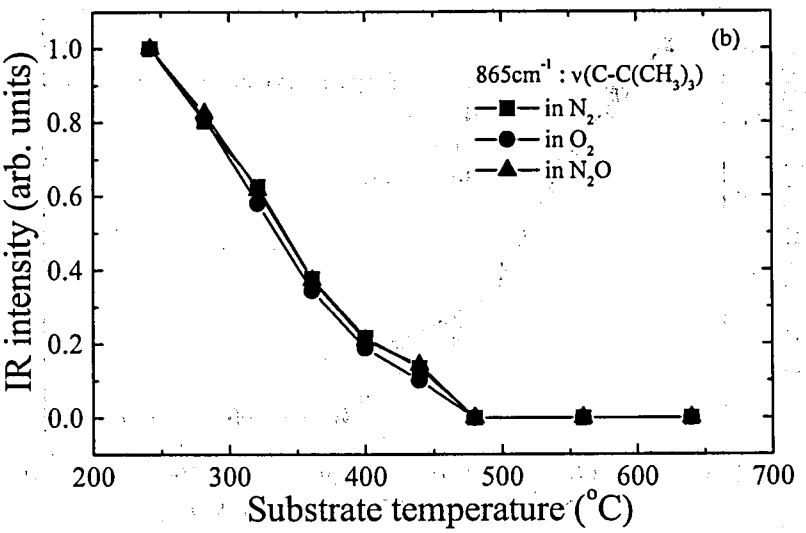

Figure 4.5: Substrate temperature dependence of the normalized IR absorption peak intensities of $Sr(DPM)_2$ in N_2, O_2 and N_2O ambients: (a) 733 cm^{-1} peak, (b) 865 cm^{-1} peak and (c) 1590 cm^{-1} peak.

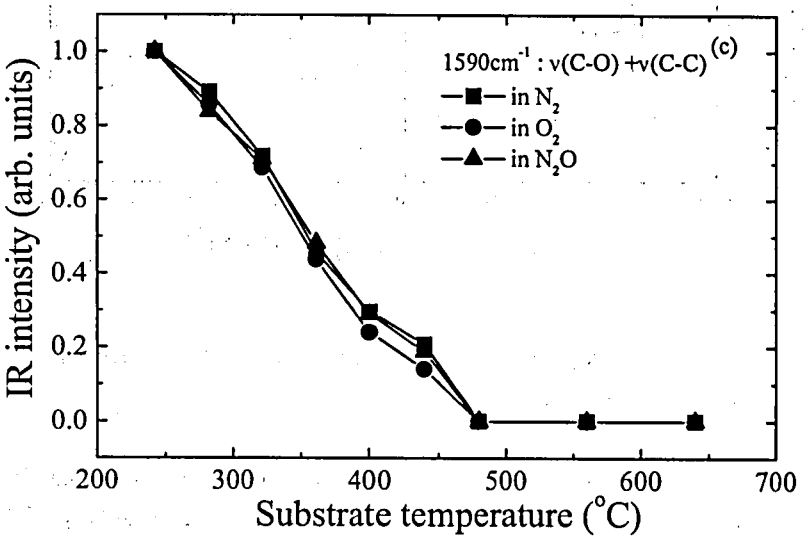

Figure 4.5: Substrate temperature dependence of the normalized IR absorption peak intensities of $Sr(DPM)_2$ in N_2, O_2 and N_2O ambients: (a) 733 cm^{-1} peak, (b) 865 cm^{-1} peak and (c) 1590 cm^{-1} peak.

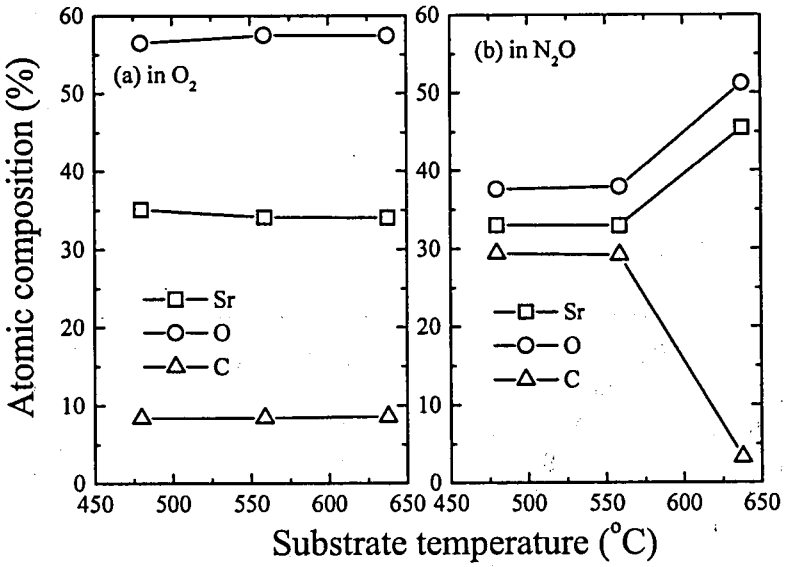

Figure 4.6: Atomic composition of strontium oxide films deposited in O_2 and N_2O ambients: (a) O_2 and (b) N_2O.

sities of the IR absorption peaks upon the addition of oxidation gases was observed in the measured range of T_s. In contrast to Ti(*t*-BuO)$_2$(DPM)$_2$, the thermal decomposition of Sr(DPM)$_2$ proceeded to a greater extent even in the absence of oxidation gases in the range of T_s investigated, so that the effect of the oxidation gases on Sr(DPM)$_2$ could not be detected directly.

4.3.3 Difference in oxidation effect between O_2 and N_2O

In order to understand the role of oxidation gas in film formation, the characteristics of strontium oxide films deposited in O_2 and N_2O ambients were investigated as the first step. The flow rates of the Sr source molecule and oxidation gas were 0.2 and 1000 sccm, respectively. Figure 4.6 shows the atomic composition of the deposited strontium oxide films. When O_2 was used as

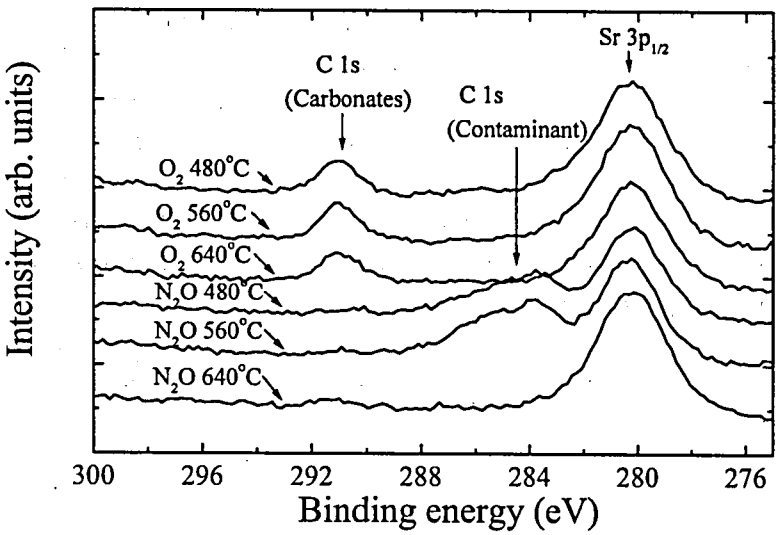

Figure 4.7: C 1s XPS spectra for strontium oxide films deposited in O_2 and N_2O ambients.

the oxidizing agent, the atomic composition of the deposited oxide films was constant. On the other hand, when N_2O was used, the atomic composition varied drastically with the increase in T_s. When the substrate temperature was below 560°C, the oxygen content was low and a large amount of carbon was incorporated. This is similar to the results of the films deposited in the absence of an oxidation gas. This finding indicates that N_2O hardly acts as an oxidizing agent when the substrate temperature is lower than 560°C. However, when the substrate temperature is higher than 640°C, the oxygen content is increased and the incorporation of carbon is suppressed. This is similar to the tendency caused by the addition of O_2, but the atomic composition is different from that of films deposited in the presence of O_2 gas. This indicates that N_2O acts as an oxidizing agent at high temperature (above 640°C), but the oxidation reaction of N_2O is different from that of O_2.

Figure 4.7 shows the C 1s XPS spectra for strontium oxide films. The

peak at 291 eV is due to carbonates and the broad peak at approximately 285 eV is due to carbon contaminants such as hydrocarbon and carbide [10]. When the oxidizing agent was O_2, strontium carbonate ($SrCO_3$) was formed. $SrCO_3$ is assumed to be formed by the adsorption of CO_2 gas [11]. In O_2 ambient, a decrease in the intensity of the broad IR peaks at the vicinity of 2190 and 2110 cm^{-1} occurred, both of which were due to carbon monoxide (CO), as well as the decrease in the intensity of the broad peak at the vicinity of 1710 cm^{-1}, which was due to the C=O bond of the products generated by the thermal decomposition in the gas phase. Figure 4.8 shows the change of the 1710 cm^{-1} peak when O_2 and N_2O gases were added at $T_s = 640°C$. These results suggest that O_2 gas oxidizes carbon monoxide molecules and C=O bonds of the thermally decomposed fragments into carbon dioxide (CO_2).

On the other hand, the XPS peak at 291 eV did not appear in the XPS spectrum for films deposited in N_2O ambient. When the substrate temperature was low (below 560°C), a broad peak appeared at approximately 285 eV, which was quenched at $T_s \geq 640°C$. This broad peak at approximately 285 eV was observed in the XPS spectrum for films that were deposited in the absence of oxidation gas. N_2O became reactive at higher substrate temperature; however, the contribution of N_2O to the oxidation reaction during film deposition differed from that of O_2. In N_2O ambient, the intensity of the IR peak at 1710 cm^{-1} due to the C=O bond of fragments did not decrease even at high substrate temperature (see Fig. 4.8), which suggested that N_2O did not oxidize the thermally decomposed fragments into CO_2 gas in the gas phase. As a result, $SrCO_3$ was not formed. It has been reported that N_2O decomposes easily above 600°C [12]. Since the temperature of the gas phase is much lower than the substrate temperature (see Fig. 3.3 in Chap. 3), N_2O does not decompose in the gas phase even when the substrate temperature is sufficiently high. N_2O decomposes only on the substrate with temperatures above 640°C. This may be responsible for the difference in the oxidation reaction between O_2 and N_2O at high substrate temperature.

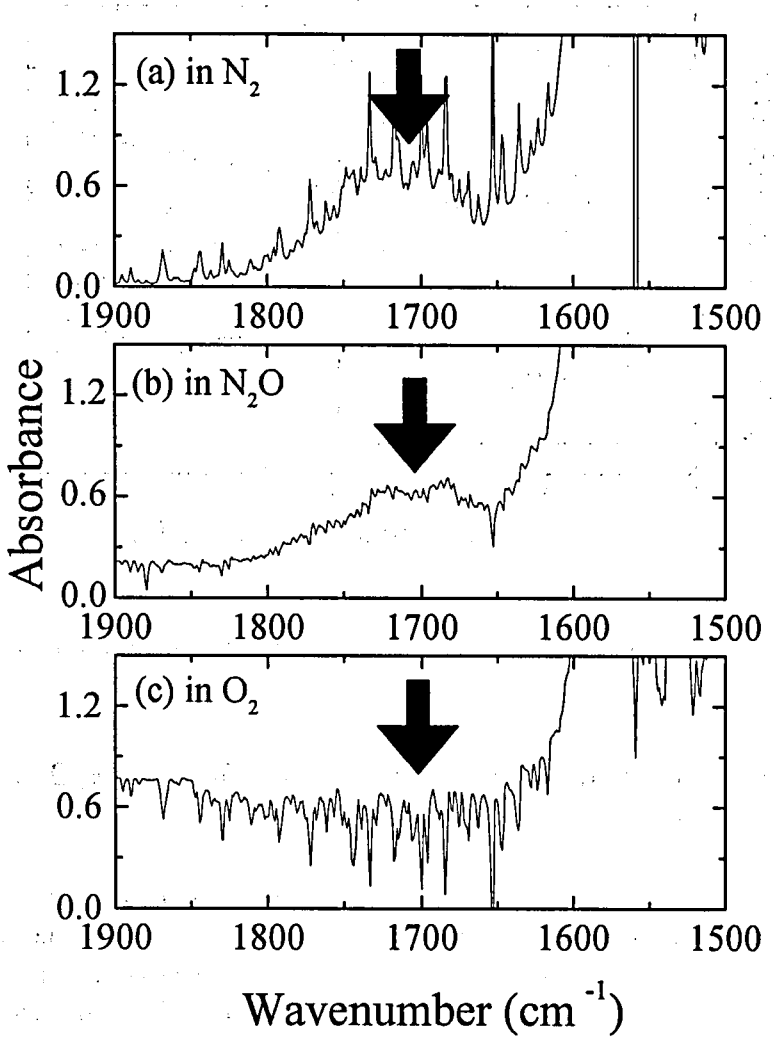

Figure 4.8: IR absorption peak of the C=O double bond of the fragments generated by the thermal decomposition in the gas phase in (a) N_2, (b) N_2O and (c) O_2 ambients.

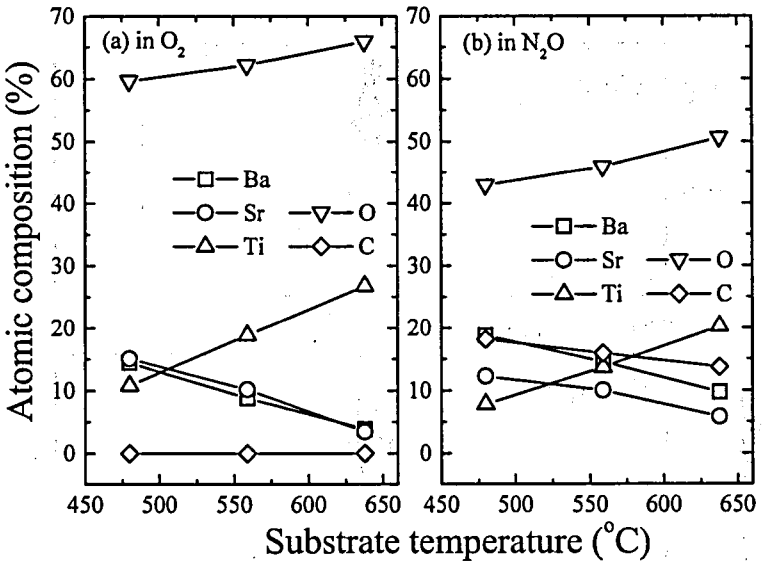

Figure 4.9: Atomic composition in the BST films deposited in O_2 and N_2O ambients: (a) O_2 and (b) N_2O.

4.3.4 BST thin films deposited in O_2 and N_2O ambients

We investigated the difference in the effects of the oxidation reactions between O_2 and N_2O during the deposition of BST films. Figure 4.9 shows the atomic composition of BST films deposited in O_2 and N_2O ambients. The flow rates of $Ba(DPM)_2$, $Sr(DPM)_2$ and $Ti(t\text{-}BuO)_2(DPM)_2$ were 0.3, 0.1 and 0.3 sccm, respectively. The flow rate of O_2 or N_2O gas was 1000 sccm. In both cases of O_2 and N_2O, the atomic composition of Ti was increased and those of Ba and Sr were decreased as the substrate temperature was increased. When the oxidation gas was O_2, however, carbon was hardly incorporated into the deposited films; in contrast, a relatively large amount of carbon was incorporated into the films when N_2O was used. In the BST films deposited in N_2O ambient, the XPS peak of C 1s appeared only at 285 eV, which is due

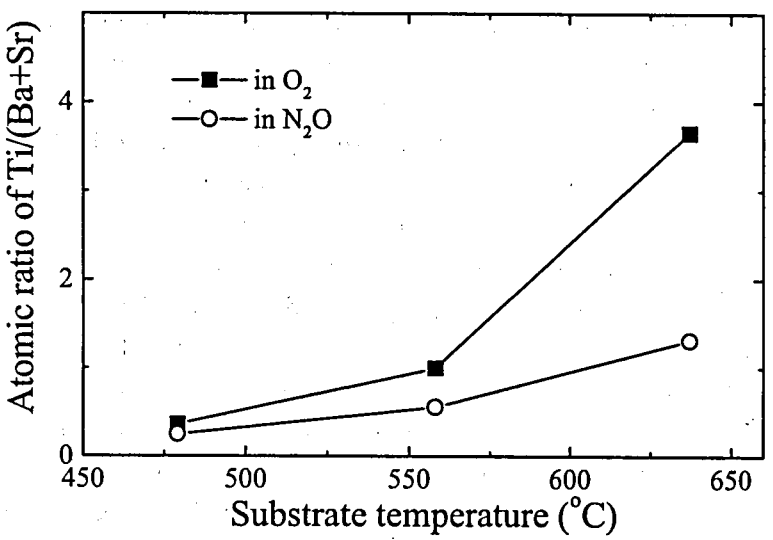

Figure 4.10: Atomic composition ratio of Ti/(Ba+Sr) in BST films deposited in O_2 and N_2O ambients.

to carbon contaminants. This result suggests that the addition of N_2O has little effect on the generation of volatile carbon oxides such as CO and CO_2. As a result, there was much carbon contamination in BST films deposited in N_2O. Figure 4.10 shows the atomic composition ratio of Ti/(Ba+Sr) in the deposited films as a function of T_s with the two kinds of oxidation gases. The ratio in the case of O_2 was larger than that in the case of N_2O. From the viewpoint of the incorporation of Ti atoms, it is found that O_2 gas is more effective for the deposition of BST films than N_2O gas at any substrate temperature.

4.4 Conclusions

We investigated the oxidation reactions of Ti(*t*-BuO)$_2$(DPM)$_2$ and Sr(DPM)$_2$ molecules in the presence of O_2 and N_2O gases by *in situ* measurements of

the IR absorption spectra. From the change of the intensities of the IR absorption peaks of Ti(t-BuO)$_2$(DPM)$_2$ with the addition of O_2 and N_2O, it was found that O_2 oxidizes the source molecules more strongly than N_2O in the gas phase. It was also found that oxidation gases do not act evenly on all the bonds of the source molecule but act on such bonds as Ti-O and C-C(CH$_3$)$_3$. This is in agreement with *ab initio* quantum chemical calculations, which shows that these sites have low electron density.

Aside from the FT-IR measurements, the role of oxidation gas was studied by means of chemical analyses of the deposited strontium oxide and BST films in O_2 and N_2O ambients. $SrCO_3$ was formed in O_2 ambient, while it was not formed in N_2O ambient. Since $SrCO_3$ is assumed to be produced by the adsorption of CO_2 gas, we suggest that O_2 can oxidize carbon-containing bonds into CO_2 while N_2O cannot do so. We found that N_2O does not oxidize source molecules at low T_s (under 560°C) but becomes reactive at high T_s (above 640°C) where N_2O is assumed to decompose thermally only on the substrate. However, the desirable T_s for the fabrication of BST capacitors in DRAMs is below 500°C; therefore, N_2O is not a suitable oxidizing agent for practical use.

Enhancement of the incorporation of Ti is also a key issue. It was found that the Ti/(Ba+Sr) ratio was decreased when the oxidation gas was changed from O_2 to N_2O. Moreover, in N_2O ambient, a relatively large amount of carbon contaminants was incorporated into the deposited BST films, which caused the increase in the leakage current in BST capacitors. This is due to the lower reactivity of N_2O than O_2 to decompose organic materials such as DPM ligands into CO_2 gas in the gas phase. In terms of the increase in the Ti/(Ba+Sr) atomic ratio and the suppression of carbon contamination, it is concluded that O_2 gas is much more suitable for the fabrication of BST capacitors than N_2O gas.

References

[1] S. Momose, T. Nakamura and K. Tachibana: Jpn. J. Appl. Phys. **39** (2000) 555.

[2] S. Momose, T. Nakamura and K. Tachibana: *CVD XV*, eds. M. D. Allendorf and M. L. Hitchman (The Electrochemical Society, Inc., New Jersey, 2000) p. 740.

[3] S. Momose, T. Nakamura and K. Tachibana: Jpn. J. Appl. Phys. **39** (2000) 5384.

[4] M. Kiyotoshi, K. Eguchi, K. Imai and T. Arikado: Jpn. J. Appl. Phys. **37** (1998) 4487.

[5] M. Yamamuka, T, Kawahara, A. Yuuki and K. Ono: Jpn. J. Appl. Phys. **35** (1996) 2530.

[6] T. Kawahara, M. Yamamuka, T. Makita, K. Tsutahara, A. Yuuki, K. Ono and Y. Matsui: Jpn. J. Appl. Phys. **33** (1994) 5897.

[7] C. S. Hwang, C. S. Kang, H.-J. Cho, S. O. Park, B. T. Lee, J. W. Kim, H. Horii, S. I. Lee and M. Y. Lee: Integr. Ferroelectr. **12** (1996) 199.

[8] J.-H. Joo, J.-B. Park, Y. Kim, K.-S. Lee, J.-S. Lee, J.-S. Roh and J.-J. Kim: Jpn. J. Appl. Phys. **38** (1999) L195.

[9] T. Nakamura and K. Tachibana: Jpn. J. Appl. Phys. **40** (2001) 338.

[10] G. Munuera, A. R. G.-Elipe, J. P. Espinos and E. L.-Molina: Surf. & Interf. Anal. **15** (1990) 693.

[11] Z. Liu, K. Xie, N. Wu, D. Shen and Z. Lin: Chinese Phys. Lett. **6** (1989) 261.

[12] W. S. Lau, P. W. Qian, N. P. Sandler, K. A. Mckinley and P. K. Chu: Jpn. J. Appl. Phys. **36** (1997) 661.

Chapter 5

Film precursor formation in MOCVD of $(Ba,Sr)TiO_3$ films

5.1 Introduction

As described in Chaps. 2, 3 and 4, we investigated the gas phase reactions in the metalorganic chemical vapor deposition (MOCVD) processing for barium strontium titanate $(Ba,Sr)TiO_3$ [BST] thin films by using several spectroscopic techniques such as microdischarge optical emission spectroscopy (μD-OES) and *in situ* Fourier transform infrared (FT-IR) spectroscopy [1, 2, 3, 4]. On the basis of these spectroscopic measurements, we found following three points as regards the chemistries of Sr source molecules. First is that most of $Sr(DPM)_2$ molecules decompose thermally in the gas phase at the typical temperature for the deposition of BST films [1, 2]. Second is that the Sr-O bond of $Sr(DPM)_2$ molecule is easiest to cleave through the thermal decomposition [2]. Third point is that species formed through the thermal decomposition of these source molecules are very easy to be oxidized when an oxidation gas is added [3]. Therefore, it is considered that the film precursors containing Sr atoms are formed from the thermal decomposition of

the parent source molecules followed by the oxidation reactions, and that the O atom in Sr precursor is derived mainly from the oxidation gas. On the other hand, we found following three points as regards the chemistries of Ti source molecule. First is that Ti(*t*-BuO)$_2$(DPM)$_2$ molecules are difficult to decompose thermally in the gas phase at the typical temperature range for deposition of BST films [2]. Second is that the Ti-O bond of Ti(*t*-BuO)$_2$(DPM)$_2$ is stable against the thermal decomposition as compared with the C-O and C-C bonds in the DPM chelate rings [2]. Third is that because of the tendency of Ti(*t*-BuO)$_2$(DPM)$_2$ molecule hard to decompose thermally and the stability of the Ti-O bond, precursors for Ti atom have less reactivity to an oxidation gas [3]. Therefore, it is thought that the Ti-O bond in the Ti source molecule is difficult to cleave through gas-phase reactions, and that the O atom in Ti precursor is originated mainly from the Ti source molecule itself. Based on the above argument, we suggest that an oxidation gas has a significant effect on the formation of Sr precursors and little effect on that of Ti precursors. In this chapter, we present the results of experiments carried out in order to verify our suggested precursor formation mechanism. We deposit strontium oxide, titanium oxide and strontium titanate $SrTiO_3$ (STO) films under various deposition conditions, and study the effect of oxidation gas on the deposition chemistries in MOCVD of these films to understand the mechanism of the precursor formation.

As an another approach to analyze deposited films, we employ an isotopic labeling experiment involving time-of-flight secondary ion mass spectroscopy (TOF-SIMS) [5, 6]. Recently, such isotopic studies on BST films were carried out by Gao *et al.* [7, 8]. In the BST film formation, a metal atom of Ba, Sr and Ti can form a metal-oxygen bond network with the oxygen incorporated along with the other kinds of metal atoms. Although they reported that the $Ti^{18}O^+/Ti^{16}O^+$ ratio (0.71) is slightly larger than the $Sr^{18}O^+/Sr^{16}O^+$ (0.62) and $Ba^{18}O^+/Ba^{16}O^+$ (0.63) values in the BST films grown at the substrate temperature of 590°C in $^{18}O_2$ ambient, the average values of all the three ratios appeared to be similar. Therefore, the experimental data does not correctly reflect the difference in the chemistries of the individual source molecules clarified from our spectroscopic measurements. We carry out an isotopic study on strontium and titanium oxide films deposited with $^{18}O_2$ as

the labeling oxidant. The deposited oxide films are analyzed by TOF-SIMS to establish whether the O atoms in the deposited films originate from the individual source molecules or oxidation gas. The aim of this isotopic labeling experiment is to verify our suggested formation mechanism of the precursor for BST films.

5.2 Experimental

The details of the experimental MOCVD apparatus are described in Chap. 2. We used $Sr(DPM)_2$ and $Ti(t\text{-}BuO)_2(DPM)_2$ as the CVD source materials of strontium oxide, titanium oxide films, and STO films. The source materials were dissolved in organic solvent, tetrahydrofuran (THF). After each dissolved source was introduced into a vaporizer by N_2 carrier gas, the vaporized source was transported into the MOCVD reactor and subsequently mixed with the oxidation gas. The substrate temperature was 600°C except for the measurements of temperature dependence. The pressure in the reactor was maintained at 1 Torr. A thin film was deposited on a 6-inch-diameter Si(200) substrate.

The deposited films prepared using $^{18}O_2$ were analyzed by TOF-SIMS. A 15 keV Ga^+ primary ion beam was used for both sputtering and analysis. The dose of primary Ga^+ ions was reduced to be less than 10^{12} ions/cm^2 (static SIMS). In this study, we employed both positive and negative SIMS. The SIMS analysis was conducted on a 25 μm^2 region, while the sputtered area was a 60 μm^2 region.

5.3 Results and Discussion

5.3.1 Effect of oxidation gas on film deposition

The results of our spectroscopic diagnoses suggested that the film precursors containing Sr atoms are formed from the thermal decomposition of the parent source molecule followed by the oxidation reactions. Thus, O atom in Sr precursor is derived mainly from the oxidation gas. On the other hand, we assumed that the Ti-O bond in the Ti source molecule is difficult to

cleave through gas-phase reactions, and that oxygen atom in Ti precursor is originated from the Ti source molecule itself. In other words, the oxidation gas plays an important role in the creation of Sr precursors for achieving good-quality oxide film deposition, while it does not make a large contribution to the formation of Ti precursors. The following experiments were carried out in order to verify the above precursor formation mechanism proposed on the basis of the results of our spectroscopic studies. We deposited strontium oxide films by changing the flow rate of O_2 gas (0 – 200 sccm) to investigate the effect of O_2 addition on the film deposition. The flow rates of $Sr(DPM)_2$ and THF were 0.2 and 0.8 sccm, respectively. In Fig. 5.1, the atomic composition in the deposited strontium oxide films is shown as a function of the flow rate of O_2 gas. When the oxidation gas was not added, a large amount of C atoms were incorporated and only a few O atoms were incorporated into the film. It is thought that the low oxygen content of the film deposited without the addition of O_2 gas was caused by the release of oxygen atoms from $Sr(DPM)_2$ via its thermal decomposition. At the beginning of O_2 addition, the number of O atoms in the strontium oxide films increased abruptly and the incorporation of C atoms was suppressed to less than 10%, which is due to the formation of $SrCO_3$. This result means that an oxidation gas has a significant effect on the formation of Sr precursors, and suggests that the O atoms in the strontium oxide films deposited with O_2 gas are derived mainly from the oxidation gas.

The same deposition experiments were performed with respect to titanium oxide films. The flow rates of $Ti(t\text{-}BuO)_2(DPM)_2$ and THF were 0.2 and 0.8 sccm, respectively. The flow rate of O_2 gas was changed from 0 to 200 sccm. In Fig. 5.2, the atomic composition in the deposited titanium oxide films is shown as a function of the flow rate of O_2 gas. Even when no O_2 gas was added, a large amount of O atoms were incorporated into the films and the incorporation of C atoms was suppressed. In contrast to strontium oxide films, the addition of O_2 gas did not have a significant effect on the atomic composition in the titanium oxide films. These experimental results of film deposition are in good agreement with the spectroscopic data on the mechanism of precursor formation.

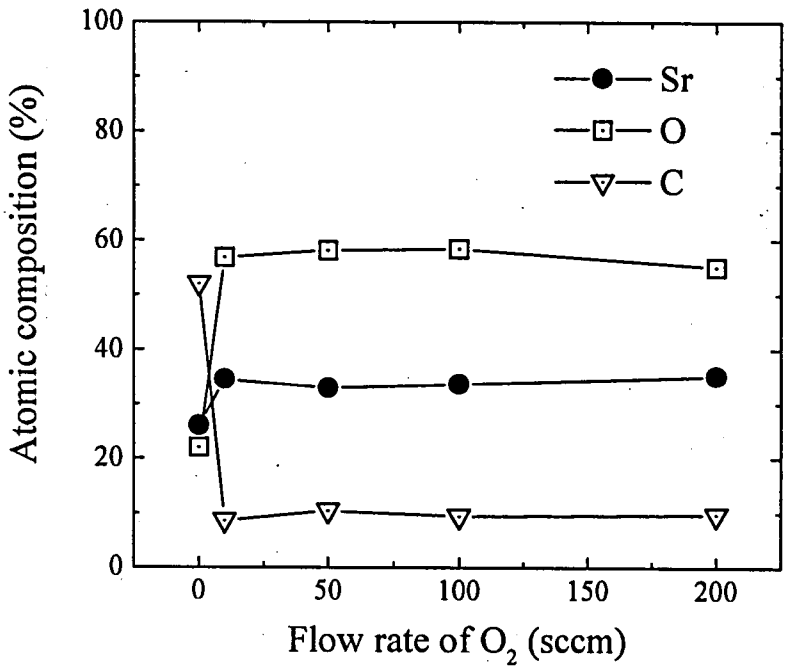

Figure 5.1: Atomic composition in the strontium oxide films as a function of the flow rate of O_2 gas.

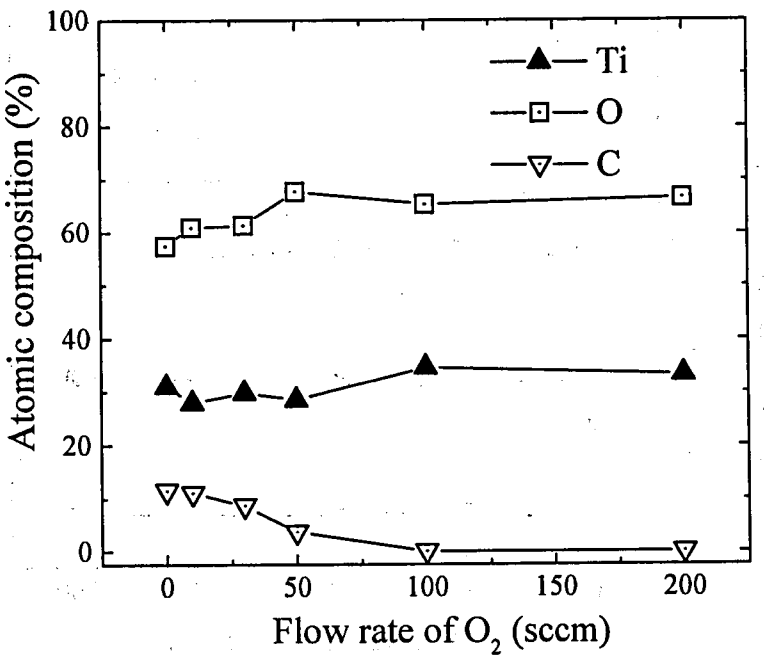

Figure 5.2: Atomic composition in the titanium oxide films as a function of the flow rate of O_2 gas.

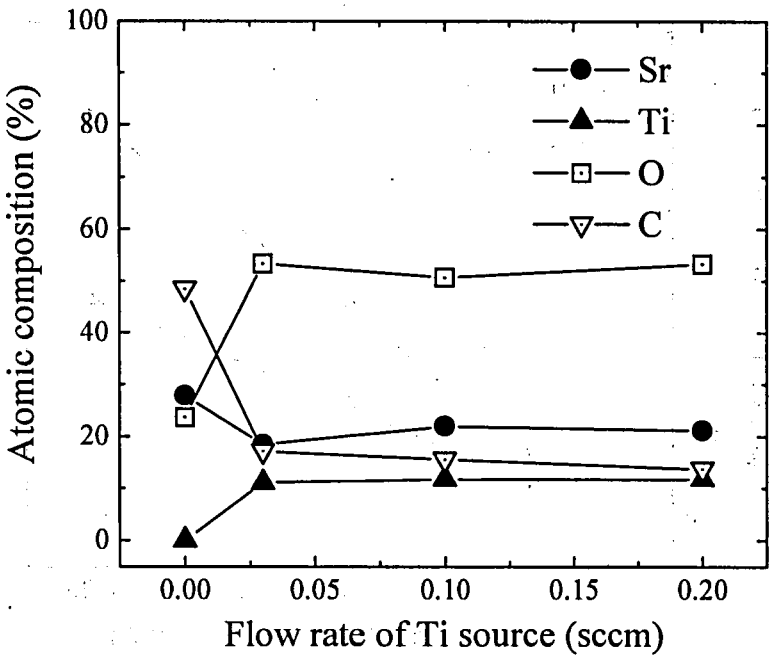

Figure 5.3: Change in the atomic composition in the $SrTiO_3$ films deposited without O_2, upon the addition of the Ti source.

5.3.2 Difference in the mechanism of film deposition between $Ti(t\text{-}BuO)_2(DPM)_2$ and $Sr(DPM)_2$

Figure 5.3 shows the change in the atomic composition ratio in the STO films deposited without O_2 gas when the flow rate of the Ti source was varied from 0 to 0.2 sccm. The flow rate of the Sr source was fixed at a constant value of 0.2 sccm. The other deposition condition was the same as in the experiments described in the above subsection. When the Ti source was added, the O atom concentration increased significantly and carbon contamination was suppressed. Although we changed the flow rate of the Ti source from 0.03 to 0.2 sccm, the atomic composition in the deposited films was constant. The addition of the Ti source showed effects similar to those of O_2 gas (see Fig.

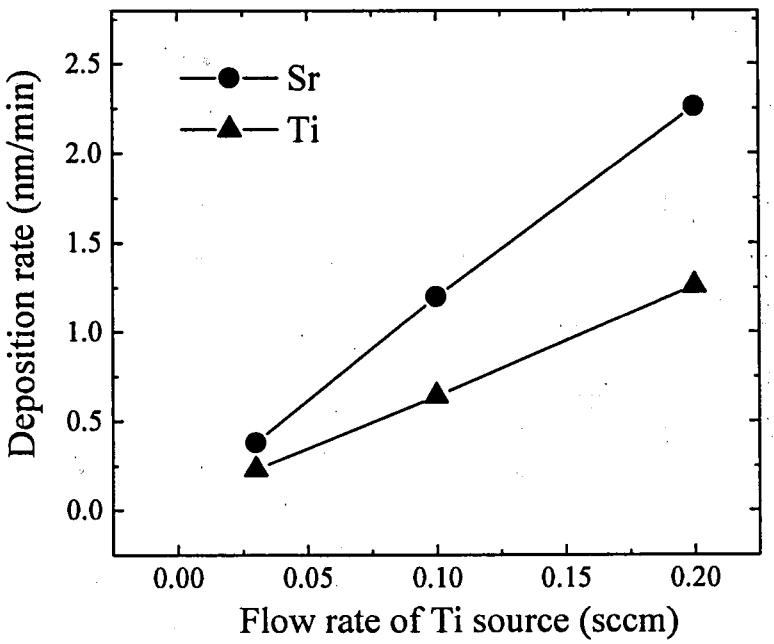

Figure 5.4: Incorporation rates of Sr and Ti atoms into the $SrTiO_3$ films deposited without O_2 addition, as a function of the flow rate of the Ti source.

5.1). This result indicates that the Ti source enhances the incorporation of O atoms and suppresses the contamination of C atoms into the deposited films. Based on the results of our spectroscopic diagnoses, we proposed that the Ti source molecule reaches the substrate surface possessing O atoms of the source molecule and that the Sr source releases O atoms of the source molecule in the gas phase. The O atoms in the Ti source molecules make a large contribution to the incorporation of O atoms in the deposited films.

Figure 5.4 shows the incorporation rates (film thickness × atomic composition) of Sr and Ti atoms in the STO films deposited without O_2 gas as a function of the flow rate of the Ti source. With the increase of the Ti source supply, not only Ti atoms but also Sr atoms were incorporated more actively

Table 5.1: Change in the atomic incorporation rates in the deposition of $SrTiO_3$ films upon the addition of O_2 gas.

	Incorporation rate (sccm)	
Element	Without O_2 addition	With O_2 addition (200 sccm)
Sr	0.38	2.12
Ti	0.23	0.24
O	1.09	2.96
C	0.35	0.34

in the films. Table 5.1 shows the change in the atomic incorporation rates of the deposited STO films when O_2 gas was added. The flow rate of the Ti source was fixed at 0.03 sccm. The other deposition conditions were the same as those in Fig. 5.4. When O_2 gas was added, the deposition rates of Sr and O atoms increased, while those of Ti and C atoms remained unchanged. This result means that the addition of O_2 is indispensable for Sr atoms to be incorporated into the oxide films. The Ti source reaches the substrate possessing O atoms in the molecular structure, while the Sr source releases O atoms in the gas phase. Due to the lack of O atoms, Sr atoms are more difficult to incorporate than Ti atoms when an oxidation gas is not added. When the flow rate of the Ti source was increased from 0.03 to 0.2 sccm, the incorporation rate of Sr atoms increased because of the increase in O atoms of the Ti source molecules. That is, when a Ti source is supplied instead of O_2 gas, reactions between the Sr precursors and the O atoms in the Ti-containing species occur in the gas phase and/or on the film surface. It is considered that the O atoms in the Ti-containing precursors determine the incorporation rate of Sr atoms into the films deposited without O_2 addition. These experimental facts are in good accordance with the precursor formation mechanism suggested from our spectroscopic measurements.

5.3.3 Isotopic labeling study using $^{18}O_2$

Additionally, we carried out isotopic labeling study using $^{18}O_2$ in order to clarify whether the O atoms in the deposited oxide films originate from the source molecules or oxidation gas. Figure 5.5 shows typical positive SIMS depth profiles near the surface of the strontium and titanium oxide films deposited in $^{18}O_2$ ambient. The flow rate of the oxidation $^{18}O_2$ gas was 10 sccm. Since the secondary ion counts after sputter removal of an approximately 1.5-nm-thick surface layer become almost constant in the deposited oxide films, these values are used in the following discussion. Figure 5.6 indicates positive SIMS spectra of the strontium and titanium oxide films, where many high-mass molecular ions are observed. Each spectral signal of the same molecular composition splits into several peaks in accordance with the isotopic ratio of oxygen, strontium and titanium atoms. On the basis of the natural abundance of strontium and titanium isotopes, we correct the isotope interference between the same mass species, e.g., $^{48}Ti^{16}O^+$ and $^{46}Ti^{18}O^+$, for Sr- and Ti-containing oxides. Contributions of ^{17}O can be neglected since the amount lies below the detection limit.

In Fig. 5.7, the positive SIMS signals are shown focusing on MO^+ (M=Sr, Ti) ions containing ^{18}O and ^{16}O. The $Ti^{18}O^+/Ti^{16}O^+$ ratio is about 0.22, which indicates that the β-diketonate and alkoxide ligands of Ti(*t*-BuO)$_2$(DPM)$_2$ are only partially substituted by $^{18}O_2$ (i.e., oxidation of the source molecules). The spectroscopic measurements in this study show that the Ti-O bond of Ti(*t*-BuO)$_2$(DPM)$_2$ is most stable against thermal decomposition. The retention of ^{16}O in the deposited titanium oxide film means that the O atoms in the titanium oxide film originate mainly from the Ti source molecules. In Fig. 5.7(a), the SIMS signals at 103.90, 104.91, 105.90 and 106.91 amu are assigned to $^{88}Sr^{16}O^+$, $^{88}Sr^{16}O^1H^+$, $^{88}Sr^{18}O^+$ and $^{88}Sr^{18}O^1H^+$, respectively. The $Sr^{18}O^+/Sr^{16}O^+$ ratio obtained from the signal intensity of $^{88}Sr^{16}O^+$ and $^{88}Sr^{18}O^+$ is about 1.8. This result indicates that the majority of the O atom in the strontium oxide film originates from the oxidation gas, which is in accordance with our suggestion about the formation mechanism of Sr precursors.

Figure 5.8 shows negative SIMS spectra of the strontium and titanium

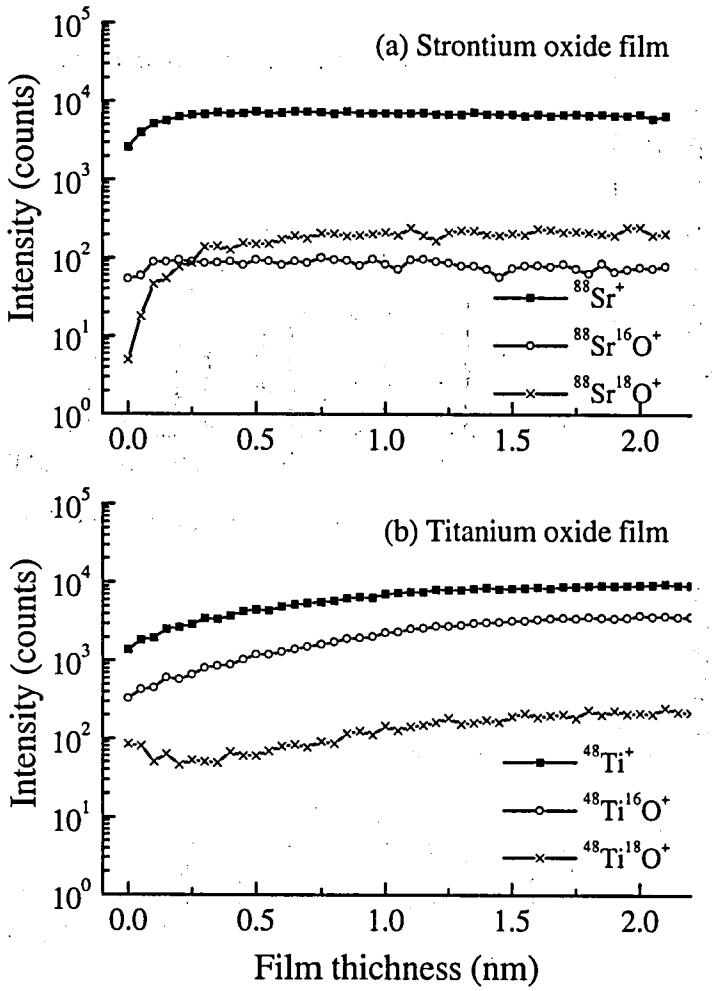

Figure 5.5: Typical positive SIMS depth profiles of (a) strontium oxide and (b) titanium oxide films deposited at the substrate temperature of 600°C in $^{18}O_2$ ambient.

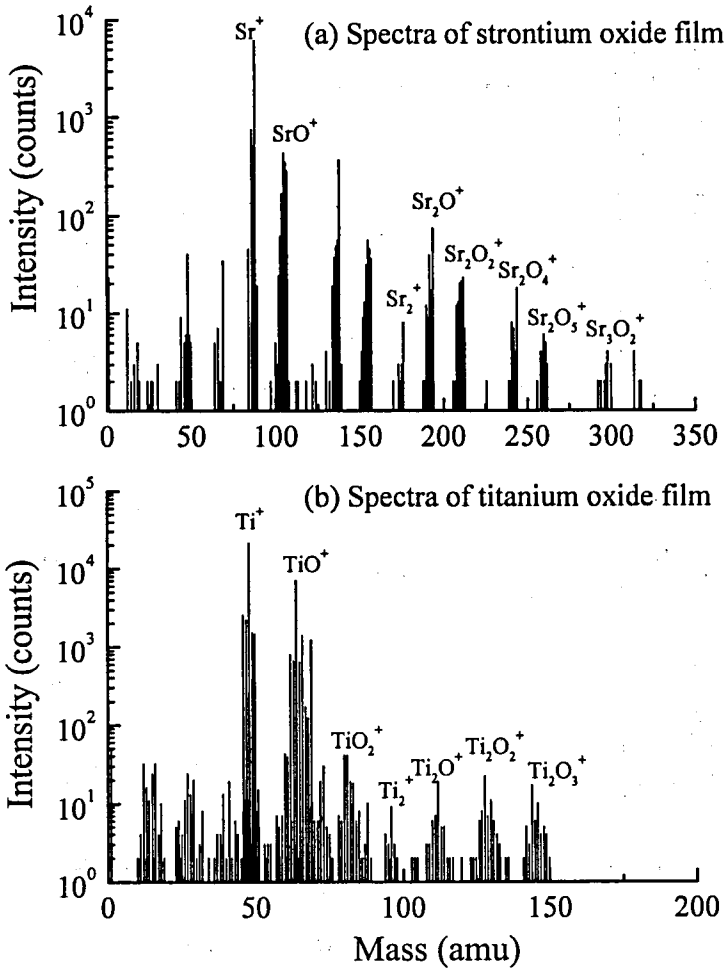

Figure 5.6: Positive SIMS spectra of (a) strontium oxide and (b) titanium oxide films deposited at the substrate temperature of 600°C in $^{18}O_2$ ambient.

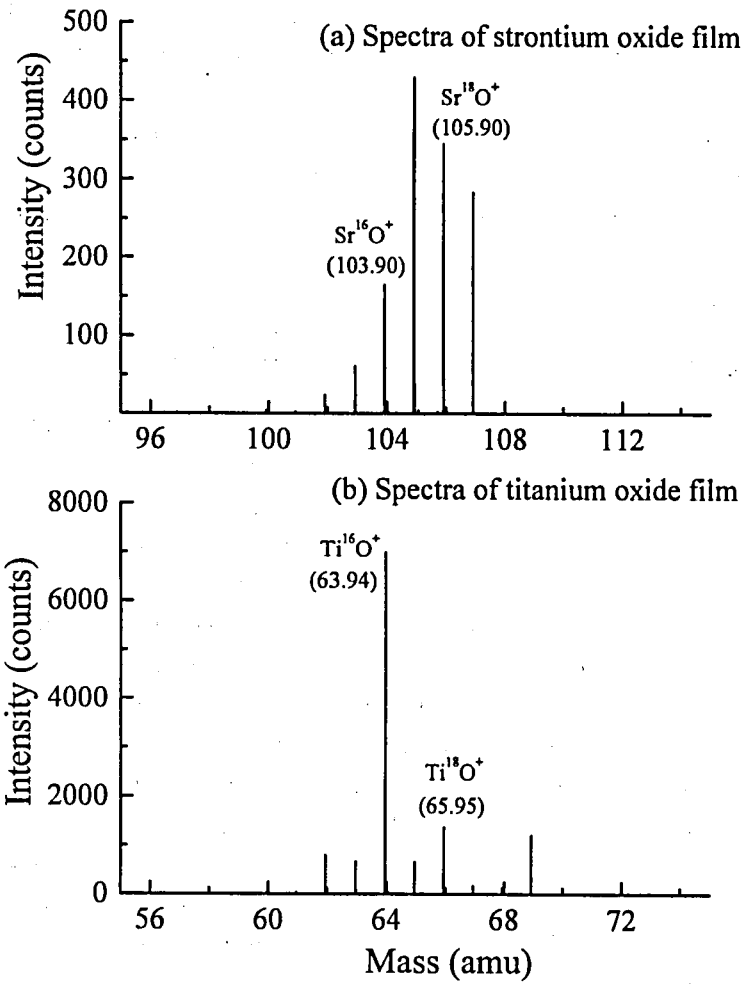

Figure 5.7: Positive SIMS signals of metal monoxide ions of (a) strontium oxide and (b) titanium oxide films deposited at the substrate temperature of 600°C in $^{18}O_2$ ambient.

oxide films. In both films, many high-mass molecular ions were detected by negative SIMS as well as positive SIMS (see Fig. 5.6). As compared with the corresponding positive SIMS spectra, however, the electronegative species such as O^- and O_2^- can be sensitively observed only by negative SIMS. In Fig. 5.9, the negative SIMS signals are shown focusing on $^{18}O^-$ and $^{16}O^-$ ions. The $^{18}O^-/^{16}O^-$ ratio is about 0.20 in the titanium oxide film, while this ratio is about 1.8 in the strontium oxide film. The obtained $^{18}O^-/^{16}O^-$ ratios showed good agreement with the corresponding $M^{18}O^+/M^{16}O^+$ (M=Sr, Ti) ratios. Therefore, $M^{18}O^+/M^{16}O^+$ ratios are indicative of ^{18}O incorporated in deposited films.

5.3.4 Temperature dependence of SIMS signals

Figure 5.10 shows temperature dependence of $M^{18}O^+/M^{16}O^+$ (M=Sr, Ti) and $^{18}O^-/^{16}O^-$ ratios. The $Ti^{18}O^+/Ti^{16}O^+$ and $^{18}O^-/^{16}O^-$ ratios of the titanium oxide films maintain small values with little change, which indicates that the thermal dissociation of the Ti-O bonds of $Ti(t\text{-}BuO)_2(DPM)_2$ is not active at the typical deposition temperature range not only in the gas phase but also on the film surface. In fact, our spectroscopic studies on gas phase reactions in MOCVD of BST films also show that the Ti-O bond is most stable against thermal decomposition [2]. The Ti-O bonds of $Ti(t\text{-}BuO)_2(DPM)_2$ are preserved in the MOCVD process, suggesting that extended chain formation occurs by diffusion and reaction of surface adsorbed species followed by cross-linking to form the final titanate network. On the contrary, the $Sr^{18}O^+/Sr^{16}O^+$ and $^{18}O^-/^{16}O^-$ ratios of the strontium oxide films are markedly reduced as the substrate temperature decreases. This suggests that at lower temperatures the thermal decomposition in the gas phase and/or on the film surface is suppressed, resulting in less incorporation of ^{18}O in the film. The ligand substitution by O_2 plays an important role in the film formations at higher temperatures.

We investigated the thermal dissociation of the metal-oxygen bond of the source molecules by μD-OES. In the substrate temperature range where this isotopic study was conducted, from 520°C to 600°C, the emission intensity of SrII changed significantly in contrast to that of TiII (see Fig. 3.7. The

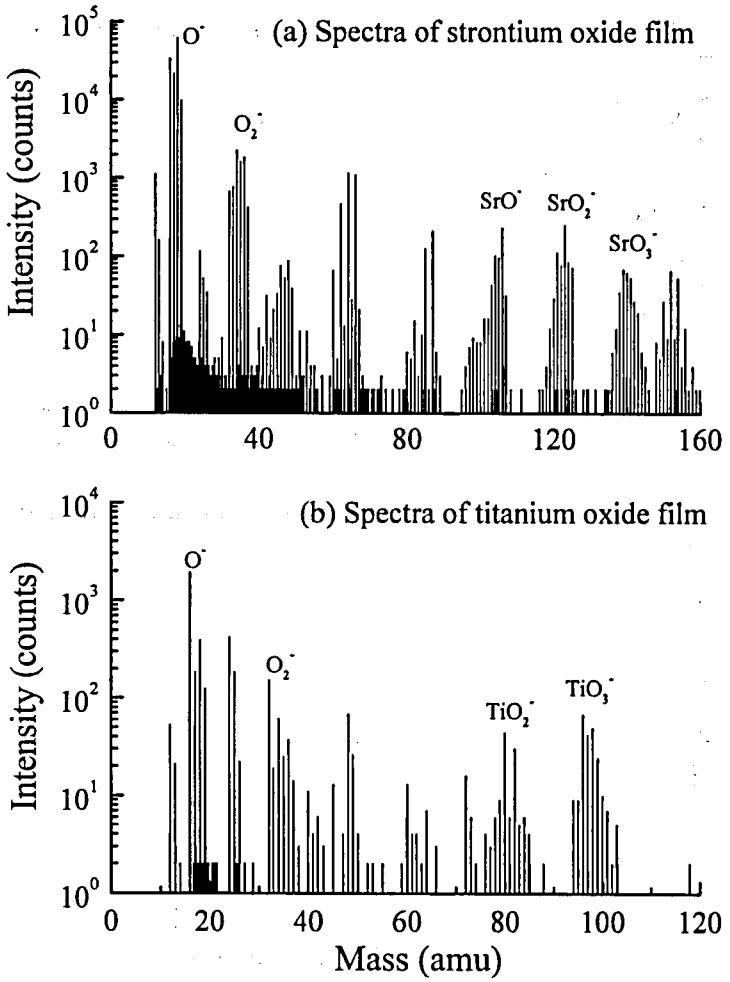

Figure 5.8: Negative SIMS spectra of (a) strontium oxide and (b) titanium oxide films deposited at the substrate temperature of 600°C in $^{18}O_2$ ambient.

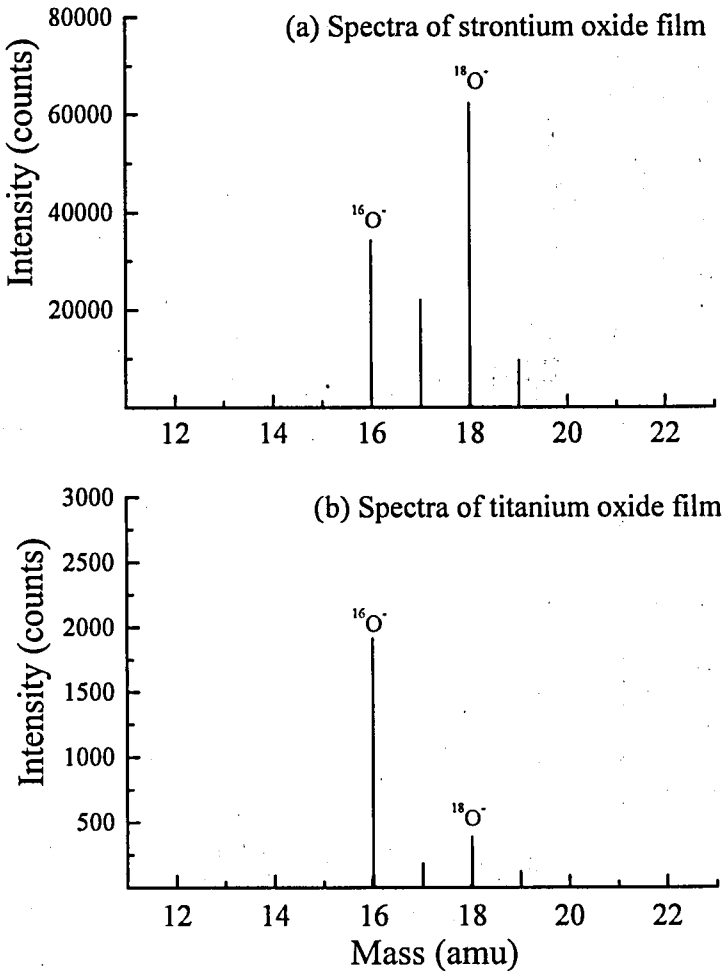

Figure 5.9: Negative SIMS signals of $^{18}O^-$ and $^{16}O^-$ of (a) strontium oxide and (b) titanium oxide films deposited at 600°C in $^{18}O_2$ ambient.

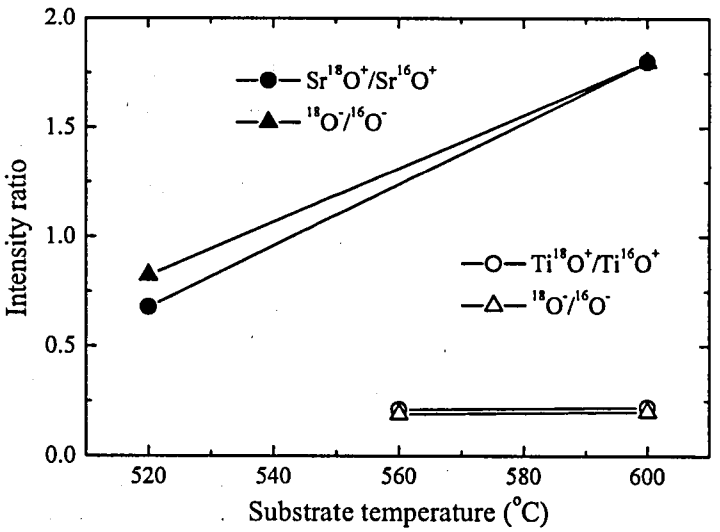

Figure 5.10: Temperature dependence of $M^{18}O^+/M^{16}O^+$ (M=Sr, Ti) and $^{18}O^-/^{16}O^-$ ratios of strontium and titanium oxide films deposited in $^{18}O_2$ ambient.

substrate temperature of 520°C and 600°C correspond to the gas temperature was of 318°C and 355°C, respectively.). The temperature dependence of the emission intensity showed a corresponding behavior to that of the SIMS signal intensity.

5.4 Conclusion

Based on the results of the spectroscopic diagnoses, a precursor formation mechanism was suggested. The film precursors for Sr atoms are formed from the thermal decomposition of the parent source molecules followed by oxidation reactions, and an oxidation gas is necessary for the formation of Sr precursors. On the other hand, the Ti-O bond in the Ti source molecule is not easily cleaved through gas-phase reactions, and the Ti precursor continues to possess the O atoms of the Ti source molecule itself. The above suggestion was verified through a series of deposition experiments of strontium oxide, titanium oxide and strontium titanate films under various deposition conditions.

Additionally, isotopic ^{18}O-labeled experiments for strontium and titanium oxide film deposition were performed to understand the oxidation reactions and verify our suggestion about a precursor formation mechanism. The surface was analyzed by TOF-SIMS to determine the extent of ^{18}O incorporation in the resulting films. In addition to the conventional positive ion detection of both $M^{18}O^+$ and $M^{16}O^+$ (M=Sr, Ti), $^{18}O^-$ and $^{16}O^-$ were sensitively monitored in the negative ion detection mode. The obtained SIMS signal counts of $^{18}O^-$ containing secondary ions in the titanium oxide films were less than those in the strontium oxide films. The majority of the oxygen in the titanium oxide films was found to originate from the source molecules, while the majority of the oxygen in the strontium oxide films was found to originate from the oxidation gas. These results were in good accordance with our precursor formation mechanism suggested on the basis of spectroscopic measurements.

References

[1] S. Momose, T. Nakamura and K. Tachibana: Jpn. J. Appl. Phys. **39** (2000) 555.

[2] S. Momose, T. Nakamura and K. Tachibana: Jpn. J. Appl. Phys. **39** (2000) 5384.

[3] S. Momose, T. Nakamura and K. Tachibana: *CVD XV*, eds. M. D. Allendorf and M. L. Hitchman (The Electrochemical Society, Inc., New Jersey, 2000) p. 740.

[4] S. Momose, R. Sahara, T. Nakamura and K. Tachibana: Jpn. J. Appl. Phys. **40** (2001) 5501.

[5] N. Selamoglu, J. A. Mucha, D. E. Ibbotson and D. L. Flamm: J. Vac. Sci. & Technol. B **7** (1989) 1345.

[6] H. C. Lu, T. Gustafsson, E. P. Gusev and E. Garfunkel: Appl. Phys. Lett. **67** (1995) 1742.

[7] Y. Gao, T. Tran and P. Alluri: Appl. Phys. Lett. **75** (1999) 415.

[8] Y. Gao, C. L. Perlins, S. He, P. Alluri, T. Tran, S. Thevuthasan and M. A. Henderson: J. Appl. Phys. **87** (2000) 7430.

Chapter 6

Conclusions

6.1 Concluding remarks

In this study, the chemical reactions in metalorganic chemical vapor deposition (MOCVD) of barium strontium titanate (Ba,Sr)TiO_3 [BST] films were investigated using spectroscopic techniques such as *in situ* infrared absorption spectroscopy and microdischarge optical emission spectroscopy (μD-OES). The results of these spectroscopic diagnoses were discussed with referring to film deposition experiments including isotopic labeling study using $^{18}O_2$. We clarified the thermal decomposition schemes, oxidation reactions with O_2 and N_2O gases, and precursor formation mechanisms for each metal element.

In Chap. 2, *in situ* Fourier transform infrared (FT-IR) spectroscopy were applied to the diagnosis in MOCVD of BST films under actual deposition conditions. We observed the temperature dependence of the IR absorbance, and investigated the thermal decomposition schemes of the source molecules. We found that $Sr(DPM)_2$ and $Ba(DPM)_2$ are much easier to decompose thermally than $Ti(t\text{-}BuO)_2(DPM)_2$, and that this difference in the thermal decomposition is caused by the difference of the strength of metal-oxygen bonds. It was found that the Sr-O and Ba-O bonds are easy to cleave, while

the Ti-O bond is difficult to cleave. We also investigated the correlation between the observed IR absorption spectra and the characteristics of the deposited BST films. It was found that the thermal decomposition in the gas phase has significant contributions to the deposition of Sr and Ba atoms than to that of Ti atoms and that the surface reactions of $Ti(t\text{-}BuO)_2(DPM)_2$ molecules are more important for the deposition of Ti atoms.

In Chap. 3, μD-OES sensor system was developed as a novel diagnostic tool for the MOCVD of BST films. In addition to FT-IR measurements, we investigated the chemistries of CVD source molecules using this μD-OES technique and obtained information about the metal-oxygen bonds in the source molecules which other spectroscopic methods are difficult to provide. It was found that at the typical deposition temperature, an oxidation gas such as O_2 has a great effect on the Sr precursor, while it does not have much effect on the Ti precursor. We also studied the interaction between $Sr(DPM)_2$ and $Ti(t\text{-}BuO)_2(DPM)_2$ in the gas phase. We demonstrated that by using μD-OES and FT-IR spectroscopy complementarily, it is possible to elucidate the gas-phase reactions in the MOCVD of BST films.

In Chap. 4, an FT-IR absorption measurement was conducted to investigate the oxidation reactions of $Ti(t\text{-}BuO)_2(DPM)_2$ and $Sr(DPM)_2$ molecules in the presence of O_2 and N_2O gases. From the change of the intensities of the IR absorption peaks of $Ti(t\text{-}BuO)_2(DPM)_2$ with the addition of O_2 and N_2O, it was found that O_2 oxidizes the source molecules more strongly than N_2O in the gas phase. We also found that oxidation gases do not act evenly on all the bonds of the source molecule but act on particular bonds such as Ti-O and C-$C(CH_3)_3$. We correlated the results of *in situ* FT-IR measurements with the characteristics of the oxide films deposited in O_2 and N_2O ambients. On the basis of the experimental findings on the increase in the Ti/(Ba+Sr) atomic ratio and the suppression of carbon contamination, it is concluded that O_2 is much more suitable for the fabrication of BST capacitors than N_2O.

In Chap. 5, based on the results of the spectroscopic diagnoses such as μD-OES and *in situ* FT-IR spectroscopy, we proposed a precursor formation mechanism as follows. The film precursors for Sr atoms are formed from the thermal decomposition of the parent source molecules followed by oxidation

reactions, and an oxidation gas is necessary for the formation of Sr precursors. On the other hand, the Ti-O bond in the Ti source molecule is not easily cleaved in the gas phase, and the Ti precursor continues to possess the O atoms of the Ti source molecule itself. This proposed precursor formation mechanism was verified through a series of deposition experiments of strontium oxide, titanium oxide and strontium titanate films under various deposition conditions. In addition to these deposition experiments, isotopic ^{18}O-labeled experiments for strontium and titanium oxide film deposition were performed in order to ascertain the precursor formation mechanism. The results of this isotopic study were in good accordance with our precursor formation mechanism proposed on the basis of spectroscopic measurements.

6.2 Future prospects

In this work, we elucidated the chemical reactions in the gas phase during the MOCVD of BST films by using *in situ* spectroscopic techniques such as μD-OES and FT-IR spectroscopy. BST films are deposited through chemical reactions not only in the gas phase but also on the substrate. The author think *in situ* diagnosis of chemical reactions on the substrate surface is necessary for deeper understanding of the deposition mechanisms of BST films, which is a subject for the future study.

We developed the μD-OES technique by employing microplasma as a probe for the diagnosis in the semiconductor manufacturing process. These days, microplasma has been investigated to realize an on-chip chemical analysis device as part of a miniaturized total analytical system (μ-TAS), which is forecasted to be applicable to a variety of fields such as chemical analysis, clinical analysis, DNA sequencing, drug screening, and health care application [1, 2]. In this system, microplasma is expected to have a function as a biochemical sensor. In this study, we showed the potentiality that microplasma is available for the elucidation of chemical reactions. The author hope that this study of μD-OES helps to develop a μ-TAS.

MOCVD technique is widely used for the manufacturing of various electronic devices. For example, ferroelectric films such as lead zirconate titanate $Pb(Zr,Ti)O_3$ [PZT], strontium bismuth tantalate $SrBi_2Ta_2O_9$ [SBT],

and bismuth titanate $Bi_4Ti_3O_{12}$ [BIT] are prepared by MOCVD technique for a non-volatile Ferroelectric Random Access Memory (FeRAM). FeRAM is a new electronic device which has been attracted a great deal of attention because of its promising applications such as portable personal computers, personal digital assistants (PDAs), cellular phones, and especially electronic money cards [3]. Moreover, it is reported that the adaptive-learning function was observed in a neuron circuit using a SBT film [4]. In order to develop these electronic devices in the future, it is inevitably necessary to understand the deposition mechanism of these films. In addition to the MOCVD of BST films, the *in situ* spectroscopic techniques developed in this study are applicable to the diagnosis in these MOCVD processes.

References

[1] T. Ujiie, T. Kikuchi, T. Ichiki and Y. Horiike: Jpn. J. Appl. Phys. **39** (2000) 3677.

[2] H. Yoshiki and Y. Horiike: Jpn. J. Appl. Phys. **40** (2001) L360.

[3] Y Uemoto: OYO BUTURI **67** (1998) 1256.

[4] S.-M. Yoon, E. Tokumitsu and H. Ishiwara: Jpn. J. Appl. Phys. **38** (1999) 2289.

List of publication

Papers

1. *Microdischarge Optical Emission Spectroscopy as a Novel Diagnostic Tool for Metalorganic Chemical Vapor Deposition of (Ba,Sr)TiO_3 Films*

   Shun Momose, Toshihiro Nakamura and Kunihide Tachibana: Jpn. J. Appl. Phys. **39** (2000) pp.555-559.

2. *Effects of Gas-Phase Thermal Decompositions of Chemical Vapor Deposition Source Molecules on the Deposition of (Ba,Sr)TiO_3 Films: A Study by In Situ Fourier Transform Infrared Spectroscopy*

   Shun Momose, Toshihiro Nakamura and Kunihide Tachibana: Jpn. J. Appl. Phys. **39** (2000) pp.5384-5388.

3. *Diagnostics of Metalorganic Chemical Vapor Deposition of (Ba,Sr)TiO_3 Films by Microdischarge Optical Emission Spectroscopy*

   Shun Momose, Toshihiro Nakamura and Kunihide Tachibana: *CVD XV*, eds. M. D. Allendorf and M. L. Hitchman (The Electrochemical Society, Inc., New Jersey, 2000) pp.740-747.

4. *Diagnosis of Oxidation Reactions in Metalorganic Chemical Vapor Deposition of (Ba,Sr)TiO_3 Films by In Situ Fourier Transform Infrared Spectroscopy*

   Shun Momose, Ryusuke Sahara, Toshihiro Nakamura and Kunihide Tachibana: Jpn. J. Appl. Phys. **40** (2001) pp.5501-5506.

5. *Formation Mechanism of Strontium and Titanium Oxide Films by Metalorganic Chemical Vapor Deposition: An Isotopic Labeling Study Using $^{18}O_2$*

   Toshihiro Nakamura, Shun Momose and Kunihide Tachibana: Jpn. J. Appl. Phys. 40 (2001) pp.6619-6622.

6. *Film Precursor Formation in Metalorganic Chemical Vapor Deposition of Barium Strontium Titanate Films: A Study by Microdischarge Optical Emission Spectroscopy*

   Shun Momose, Toshihiro Nakamura and Kunihide Tachibana: Jpn. J. Appl. Phys., in press.

7. *Effects of O_2 Gas on Reaction Mechanisms in the Chemical Vapor Deposition of (Ba,Sr)TiO_3 Thin Film*

   Mikio Yamamuka, Shun Momose, Toshihiro Nakamura, Kunihide Tachibana and Hiroshi Takada: Jpn. J. Appl. Phys., in press.

Proceedings papers

1. *In Situ Diagnostics of Metal-Organic Chemical Vapor Deposition by Micro-Discharge Optical Emission Spectroscopy*

   Shun Momose, Toshihiro Nakamura and Kunihide Tachibana: *Bulletin of The American Physical Society, Program of the 51st Annual Gaseous Electronics Conference and the 4th International Conference on Reactive Plasmas*, Maui, Hawaii, 1998 (American Institute of Physics, New York, 1998), pp.1457.

2. *Diagnostics of Metalorganic Chemical Vapor Deposition of (Ba,Sr)TiO_3 Films by Microdischarge Optical Emission Spectroscopy*

   Shun Momose, Toshihiro Nakamura and Kunihide Tachibana: *Meeting Abstracts of the 197th Meeting of The Electrochemical Society*, Toronto, Canada, 2000 (The Electrochemical Society, Inc., New Jersey, 2000), pp.949.

3. *Effect of Gas Phase Reactions on the Deposition of $(Ba,Sr)TiO_3$ Film*

   Shun Momose, Ryusuke Sahara, Toshihiro Nakamura and Kunihide Tachibana: *Proceedings of the 17th Meeting on Ferroelectric Materials and Their Applications*, Kyoto, Japan, 2000 (Organizing Committee of FMA-17, 2000), pp.83-84.

4. *Gas Phase Reactions in the MOCVD of $(Ba,Sr)TiO_3$ Films: A Study by Microdischarge Optical Emission Spectroscopy*

   Shun Momose, Toshihiro Nakamura and Kunihide Tachibana: *Extended Abstracts of the 2000 International Conference on Solid State Devices and Materials*, Sendai, Japan 2000 (The Japan Society of Applied Physics, Tokyo, 2000), pp.160-161.

5. *Diagnosis of Oxidation Reactions in MOCVD of $(Ba,Sr)TiO_3$ Films by In Situ FT-IR Spectroscopy*

   Shun Momose, Ryusuke Sahara, Toshihiro Nakamura and Kunihide Tachibana: *Proceedings of the 18th Meeting on Ferroelectric Materials and Their Applications*, Kyoto, Japan, 2001 (Organizing Committee of FMA-18, 2001), pp.17-18.

6. *Study of Deposition Mechanisms of Barium Strontium Titanate Films*

   Shun Momose, Toshihiro Nakamura and Kunihide Tachibana: *Abstracts of Annual American Physical Society March Meeting 2002*, Indianapolis, Indiana, 2002 (American Physical Society, Maryland, 2002), in press.